UNIVERSIDADE FEDERAL DO RIO GRANDE DO SUL
INSTITUTO DE FÍSICA

A new proposal for avoiding sintering of nanoparticles in catalysis

Fabio Rasera Figueiredo

M.Sc. dissertation taken under the supervision of Dr. Fabiano Bernardi and Dr. Carolina Brito submitted to the Graduate Program of Instituto de Física - Universidade Federal do Rio Grande do Sul (UFRGS) as part of the fulfillment to obtain the Master's degree in physics.

Porto Alegre, RS, Brazil
2021

⋆ Funded by Conselho Nacional de Desenvolvimento Científico e Tecnológico (CNPq)

UNIVERSIDADE FEDERAL DO RIO GRANDE DO SUL
INSTITUTO DE FÍSICA

Uma nova proposta para evitar *sintering* de nanopartículas em catálise

Fabio Rasera Figueiredo

Porto Alegre, RS, Brasil
2021

⋆ Financiado pelo Conselho Nacional de Desenvolvimento Científico e Tecnológico (CNPq)

"In my head there are several windows, that I do know,
but perhaps it is always the same one,
open variously on the parading universe.
Samuel Beckett
(Molloy, 1951.)

Acknowledgements

Above all, I thank my mother, Ivani Cristina Rasera, without whom I would never have the chance to enter an university. She has taken many more roles than she was supposed to, as the ones of my absent father and many times of a friend, when I was still unable to reach other people. She struggled to maintain the most nurturing environment she could, even when violence and scarcity were threatening our home. I truly admire her strength and never-ending love. I know that, in her eyes, the hard times will be worth it if she can see her sons and daughter succeed. And I surely can not find a bigger motivation to succeed.

I would like to express my deepest gratitude to my advisor, Fabiano Bernardi, and my co-advisor, Carolina Brito. I have been under professor Fabiano's guidance since 2016. His disposition to help, always objectively but never unkindly, made me feel free to knock on his door whenever I had questions. Besides his orientation in research projects, he has been my teacher in more than one class and my advisor in the incredible Open Laboratories Project. In all forms I have learned so much with him. Specially to never settle with OK when there is room for doing better. I have always admired his attention to details and great capacity to synthesize complex arguments without losing scientific rigor. I have the ambition to one day become a teacher and I hope I can be half as capable as he is in teaching. Carolina has been my co-advisor since the beginning of 2019, but she had my admiration long before this. As a fan of the Fronteiras da Ciência podcast, I have heard her conversations on so many distinct topics with that kind of curiosity and sharp questioning that makes her so interesting to talk to and such a good researcher. When I nervously entered her office to present myself for the first time, it did not took me more than a few minutes to feel comfortable and excited to work with her. The enthusiastic interest she showed for the project brought me confidence and strengthen the belief that I was doing something valuable. The academic environment can be harsh for people who are still insecure at the beginning of their careers, specially living in a country where scientists are feeling less and less valued. Carolina always had a kind word after our meetings and each one of these complimentary words had a huge impact on me. I deeply appreciate this. As much as her qualities as a researcher and advisor are unquestionably exceptional, I would like to point out that her ability to communicate with students and other professors in a candid and horizontal way is one of the things that I most admire in her.

I must thank my partner, Marina Dal Ponte, for the immeasurable help she gives me. She is the one who is there for better or worst. I admire so much her intelligence,

organization and responsibility that I find myself sporadically thinking on how would she do things that I have no clue how. Since I met her, my heart has been ticking with this fervorous passion, while my mind is embedded in a warm and complacent comfort. She is alluring in many ways, but her honesty is something unheard-of. There is a huge relief in madly love someone that you trust without effort, and specially in feeling on every look, word and touch that this feeling is a two way street. Marina brought me a fiery desire to keep going, no matter what, so I can be there to see her accomplish her dreams, and I have no doubt that she also wants to see me accomplish mine.

I need to make a honorable mention to my dog, Antonella, because she brought a lightness to these hard times of pandemic and careless government. This little dog has no idea of how good of a companion she is.

Finally, I thank the National Council for Scientific and Technological Development (CNPq) for my scholarship, the National Center for Research in Energy and Materials (CNPEM) for receiving me and the many people who helped me conduct measurements at the departments of Physics and Chemistry at UFRGS. Also, I would like to acknowledge the work done by UFRGS' administration, specially at the Physics post graduation program.

Resumo para Público Leigo

Os catalisadores são substâncias que aumentam a velocidade de reações químicas e por isso são utilizados em mais de 90% de todos os processos químicos da indústria. Sem os catalisadores, seria praticamente inviável suprir a grande demanda de alimentos e fármacos que a sociedade exige. Os catalisadores ainda se destacam no controle de poluentes, como na quebra de moléculas que constituem gases nocivos para o ser humano e contribuem para agravar o aquecimento global.

Com o advento da nanociência, o estudo e desenvolvimento de catalisadores foram revolucionados. A nanociência trabalha com materiais na escala nanométrica, tais como nanopartículas, onde 1 nanômetro corresponde a bilionésima parte do metro. Para compreender melhor o significado de tal quantidade, o tamanho de uma bola de futebol está para o tamanho da Terra assim como 1 nanômetro está para o tamanho de uma bola de futebol. Por conta disso, a maior parte dos átomos das nanopartículas se encontram em sua superfície. Como as reações catalíticas ocorrem na superfície dos catalisadores, o alto percentual de átomos superficiais das nanopartículas as tornam catalisadores muito mais eficientes que materiais comuns. No entanto, reações catalíticas exigem altas temperaturas e isso ocasiona a migração e aglomeração das nanopartículas, que aumentam irreversivelmente de tamanho. Este fenômeno é chamado de *sintering* e devido a ele o percentual de átomos superficias das nanopartículas diminui, causando prejuízos a sua atividade catalítica.

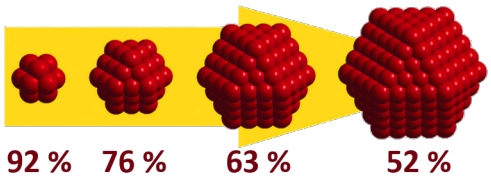

Percentual de átomos na superficie em relação ao número total de átomos de uma nanopartícula conforme seu aumento de tamanho.

Este trabalho busca evitar *sintering* de nanopartículas através de uma estratégia inédita, que se baseia em criar obstáculos para que as nanopartículas tenham menor probabilidade de entrarem em contato e aumentarem de tamanho. Os experimentos demonstram que o método é muito eficiente na prevenção de *sintering* sem causar danos secundários às nanopartículas. Ainda, foi possível descrever com clareza como a inclusão de obstáculos previne *sintering* e quais as condições importantes para que o método seja efetivo.

Sintering é a principal causa de desativação de catalisadores e a facilidade de aplicação do método proposto, em conjunto com a possibilidade de adaptação para diversos tipos de catalisadores, o tornam extremamente promissor.

Abstract

Sintering is a process whereby nanoparticles increase their size and reduce their number under high temperatures. Since catalytic activity depends on the number of active sites, and those lie on the surface of nanoparticles, the most detrimental consequence of sintering for catalysis is the loss of surface area, which reduces the number of active sites. Sintering is the main cause of catalyst deactivation and the current prevention strategies demand specific synthesis methods, modification of the chemical properties of the nanoparticles or nanostructuring of supports. A new proposal for the prevention of sintering of nanoparticles, easily reproducible, is presented and applied to Cu nanoparticles supported on MgO. A combination of XRD, *in situ* EXAFS and TEM shows the prevention of sintering of Cu nanoparticles under H_2 atmosphere at 300 °C. *In situ* time-resolved XANES and XPS techniques were used to investigate the possibility of catalyst poisoning due to the strategy employed. The results show no evidence of poisoned species. Furthermore, by modelling the system with Monte Carlo simulations, it was possible to reproduce sintering prevention and to propose a possible mechanism whereby the method operates, besides getting a better picture of the pertinent parameters value range that allows sintering prevention.

Keywords: Sintering, nanoparticles, heterogeneous catalysis, catalyst deactivation, catalyst poisoning.

Resumo

Sintering é um processo pelo qual nanopartículas aumentam o seu tamanho e reduzem seu número sob altas temperaturas. Como a atividade catalítica depende do número de sítios ativos, e estes se encontram na superfície das nanopartículas, a consequência mais prejudicial do *sintering* para catálise é a perda de área superficial, que reduz o número de sítios ativos. *Sintering* é a principal causa de desativação de catalisadores e as estratégias de prevenção atuais demandam métodos de síntese específicas, modificação das propriedades químicas das nanopartículas ou nanoestruturação dos suportes. Uma nova proposta para a prevenção de *sintering* de nanopartículas, facilmente reproduzível, é apresentada e aplicada a nanopartículas de Cu suportadas em MgO. Uma combinação de medidas de XRD, EXAFS *in situ* e TEM demonstra a prevenção de *sintering* das nanopartículas de Cu sob atmosfera de H_2 à 300 °C. As técnicas de XANES *in situ* resolvido no tempo e XPS foram utilizadas para explorar a possibilidade de envenenamento do catalisador devido à estratégia empregada. Os resultados indicam que não há qualquer composto envenenado. Ademais, modelando o sistema utilizando simulações de Monte Carlo foi possível reproduzir a prevenção de sintering e propôr um mecanismo pelo qual o método opera, além de se obter uma figura mais ampla do intervalo de valores de parâmetros que permitem a prevenção de *sintering*.

Palavras-chaves: Sintering, nanopartículas, catálise heterogênea, desativação de catalisadores, envenenamento de catalisadores.

Contents

List of Figures

List of Tables

Chapter 1

Introduction

In the 20th century physicists dove in the invisible universe of small scale. The consolidation of quantum mechanics allowed the modeling and experimental probing of low dimensional systems, leading to the development of new scientific fields. Nanoscience emerged within this context and gave rise to impacting applications, not only for the scientific community, but for the development of new technologies for the society. Since its arrival, nanoscience has pushed boundaries in physics (Fomin, 2013, Dupas & Lahmani, 2007), chemistry (Park, 2007, Whitesides, 2005), geology (JU et al., 2015, Ju et al., 2016), materials science (Chong, 2004), bioscience (Khawaja, 2011), electronics (Lieber, 2011, Chappert et al., 2010), among other fields.

Nanoscience is the study of phenomena and manipulation of materials at atomic, molecular and macromolecular scale, where system properties differ significantly from those at a larger scale (Pidgeon et al., 2004). The *nano* prefix comes from the greek word "nanos", meaning dwarf, and represents one billionth of an unit. That means nanoscience deals with materials with sizes around 10^{-9} m. For comparison purposes, a strand of human hair has a diameter of approximately 80000 nm, a red blood cell diameter is around 7000 nm and a single water molecule lengths around 0.3 nm. In low dimensional systems quantum mechanics reigns, replete of phenomena which are strange to the macroscopic scale where our intuition is molded. Size-dependent properties have actually been exploited for centuries, although without the knowledge of the underlying physics. For example, gold and silver nanoparticles have been used as coloured pigments in stained glass and ceramics since the 10th century AD (Erhardt, 2003). Depending on their size, gold particles appear red, blue or gold in colour. The challenge was to make all nanoparticles with the same size (and hence the same colour), which is still today a non trivial task. Naturally, nanoscience developed side by side with advances in quantum mechanics and the conception of high precision instruments. In the 1930's the inven-

tions of the Scanning Electron Microscope and the Transmission Electron Microscope brought the possibility of atomic imaging and manipulation (Lindsay, 2010). However it was only later, around the 1980's, that nanoscience gained popularity and started to become established as a new scientific field. A lecture given by the physicist Richard Feynman at the annual American Physical Society meeting at Caltech on December 1959 (Feynman et al., 1960) is frequently reminded as one of the sparks that ignited the advent of nanoscience. In this lecture, entitled "There's Plenty of Room at the Bottom: An Invitation to Enter a New Field of Physics", Feynman speaks with excitement about the promising achievements blooming from the ability to manipulate materials at the nanoscale.

From nanoscience came the branch of nanotechnology, where nanostructures are designed for diverse applications. The aim is to create materials, devices, and systems with fundamentally new properties and functions by engineering their small structure. Key issues are being approached through the use of nanotechnology, such as the early detection, diagnostics, prognostics and selection of therapeutic strategies for cancer (Ferrari, 2005) and the increase in Nitrogen use efficiency by crops, which directly improves world food production and reduces waste generation (DeRosa et al., 2010). The nanotechnology arrival has already been consolidated as the latest big technological revolution (Hochella Jr, 2002, Keiper, 2003, Mirkin, 2005). It was even compared to the industrial revolution that took place at the 18th century due to its huge industrial and social impacts Peterson (2000). Today, it is still a rapidly growing sector. In 2016 the global nanotechnology market was evaluated at US$ 39.2 billion and estimated to reach US$ 90.5 billion by 2021. (McWilliams, 2016).

The study and development of catalysts was highly impacted by nanoscience. The scientific production regarding nanoparticle-based catalysts grew largely and today constitutes a very relevant niche of science (Bell, 2003, Campelo et al., 2009, Astruc et al., 2005). As nanoscience brought great advances to the field of catalysis, it also brought a number of new issues that need to be fixed. The sintering of nanoparticles, which is the irreversible increase in mean nanoparticle size due to high temperatures, is one of the main impairments in nanomaterial-based catalysts.

This work is focused on introducing a pioneering method to prevent sintering. The following chapter is dedicated to defining the research motivations, carrying a detailed review of the bibliography used to study and introduce the problem. Then, the experimental and numerical techniques used for analysis are explained followed by the methodology description and results analysis. Finally, a brief conclusion summarizes the main results and discuss the perspectives.

Chapter 2

Bibliographic Revision

This chapter introduces the main concepts involved in this work, presenting the scientific literature used for research.

2.1 Catalysis and Nanoparticles

Catalysts are used in most of the current technological processes of the society. Today is estimated that over 90% of all industrial chemicals are produced with the aid of catalysts (de Vries & Jackson, 2012). Its use spurred major improvements in key industries such as pharmaceuticals and foods. However, its relevance goes beyond the industrial applications. Catalysts have being studied and applied in the control of pollutants, as for example in the cleaning of toxic gases from exhaustion systems (Whittington et al., 1995), the production of clean fuels as alternative to oil-based ones (Maxwell & Naber, 1992) and more recently in the essential task of reducing greenhouse gas emissions (van der Hoeven et al., 2013, Centi et al., 2003), which are directly related to global warming (Lashof & Ahuja, 1990, Satterthwaite, 2008).

Catalysis was first conceptualized in the 1830s by Berzelius, who collected experimental evidence from many laboratories that identified the phenomenon (Somorjai & McCrea, 2001). A catalyst is defined by The International Union of Pure and Applied Chemistry (IUPAC) as a substance that increases the rate of a reaction without modifying the overall standard Gibbs energy change (ΔG) of the reaction (McNaught et al., 1997) and without consumption of catalyst, i.e., catalysts increase a reaction rate without affecting the equilibrium state of the reaction. Fig. 2.1 shows an illustrative energy diagram of a reaction with and without a catalyst, where X and Y represent the reactants and Z the product. The catalyst increases the reaction rate by lowering the activation energy. Catalysis is classified into homogeneous, where only one phase is involved,

and heterogeneous, where the reaction occurs at or near an interface between phases. Besides artificial catalysts, there are also natural catalysts (biocatalysts) present in the human body like enzimes. One example of a catalytic reaction is the decomposition of hydrogen peroxide to water and oxygen when in contact with human blood. The reaction is catalyzed by an enzyme called *catalase* which is present in blood. One catalase molecule can convert millions of hydrogen peroxide molecules to water and oxygen each second (Kaushal et al., 2018). The main goal in the study of catalysts is to increase their selectivity, which is the capability to steer a reaction to produce a desired product, and activity, which is the ability to increase a given reaction rate.

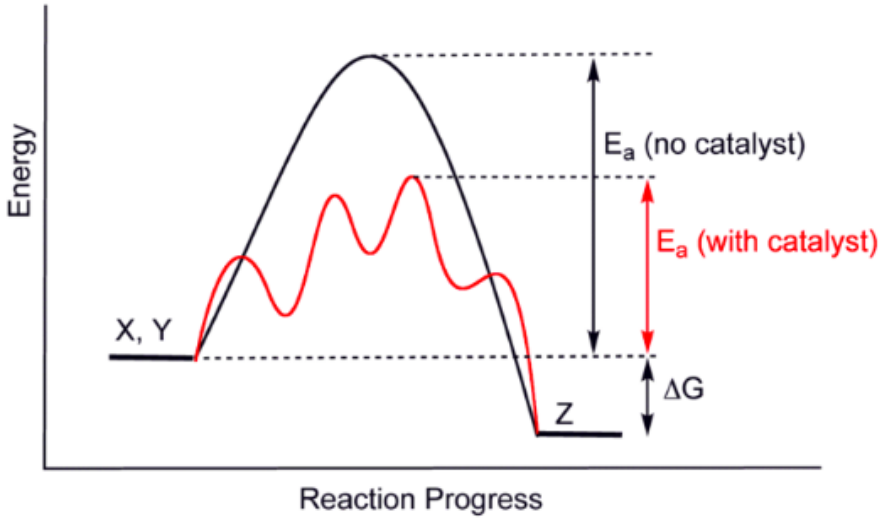

Figure 2.1: A catalyst speeds up a reaction by lowering the activation energy required for the reaction to proceed. Adapted (Learning, 2021).

2.1.1 Cluster Size Effect in Catalysis

In heterogeneous catalysis, the catalytic reaction occurs in the active sites (Taylor, 1925). As exemplified in Fig. 2.2, a catalytic reaction occurs in three main steps: the reactants first adsorb onto active sites, then react to form a product, and finally the product desorbs leaving the active site clear.

The concentration of active sites where catalytic reaction steps occur is much smaller than the total concentration of available surface sites (Somorjai et al., 2002). Since the active sites are composed by surface atoms, and smaller clusters have higher percentage of surface atoms (Fig. 2.3), the use of nanoparticles instead of bulk materials enhances catalytic activity. However, it is important to note that for some reactions the increase in cluster size can improve catalytic activity too (Shtyka et al., 2020), then the nanoparticle

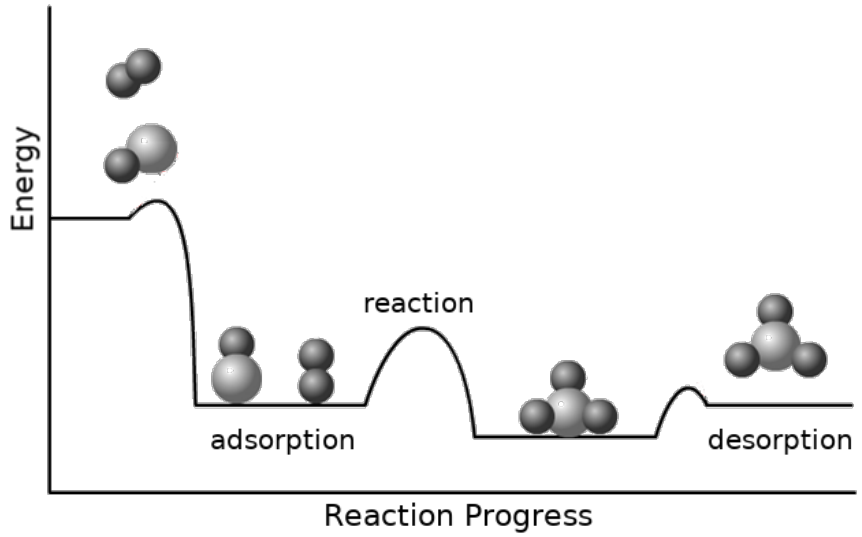

Figure 2.2: Schematic representation of a catalytic process in heterogeneous catalysis. First, the reactants adsorb into the active sites. Then the reaction occurs forming a product. Finally, the product desorbs leaving the active site available. Adapted (ESA, 2018).

size should be optimized for each catalytic reaction and catalyst. Cluster size can also affect catalytic performance because of surface and electronic properties changes with the cluster size.

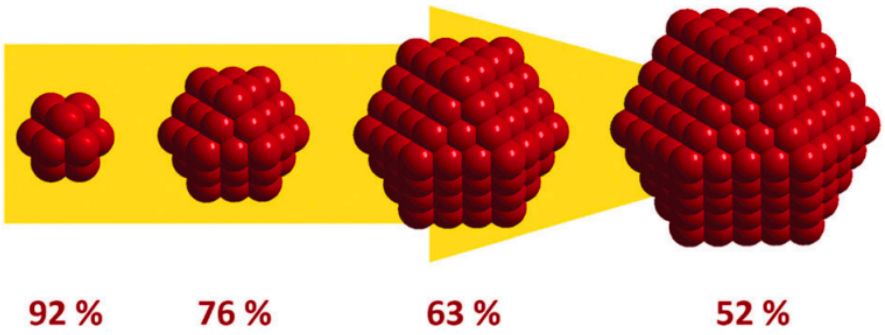

Figure 2.3: Schematic representation of the change on the percentage of surface atoms as a function of the nanoparticle size. Adapted from Sonström & Bäumer (2011).

2.1.2 Supported Nanoparticles

To achieve high dispersion and enhanced thermal stability in catalysts, in heterogeneousthe nanoparticles (which are usually metals) are generally anchored over the surface of a less active materials such as carbon black and metal oxides with high surface area,

for instance mesoporous zeolites (Navalón & García, 2016, Haruta, 1997). The material in which the nanoparticles are anchored is called support and is typically composed of particles in the order of hundreds of nm to few μm. Supported catalysts can be prepared in several ways (Delmon et al., 1997), one of the most common being deposition by impregnation. It can be made via several methods, including impregnation by soaking (Poncelet et al., 1995), dry or pore volume impregnation (Ertl et al., 2008), incipient wetness impregnation (Ertl et al., 2008), co-impregnation (Qiu et al., 2013) and successive impregnation (Del Angel et al., 2003). In this method, the nanoparticles are adsorbed by Van der Waals forces. Fig. 2.4 shows an illustration of how supported nanoparticles compose a real catalyst. Supports are usually inert during the reaction, however certain nanoparticle/support combinations can highly improve or impair the catalytic activity. Mostly, the influence of the support will be on the electronic density of states of the nanoparticles, and in particular its surface (Joyner et al., 1984). The magnitude of this interaction can be very high, e.g. in the strong metal support interaction (SMSI) effect, where the oxide moieties from support can migrate into the surface of the nanoparticles encapsulating them (Figueiredo et al., 2019).

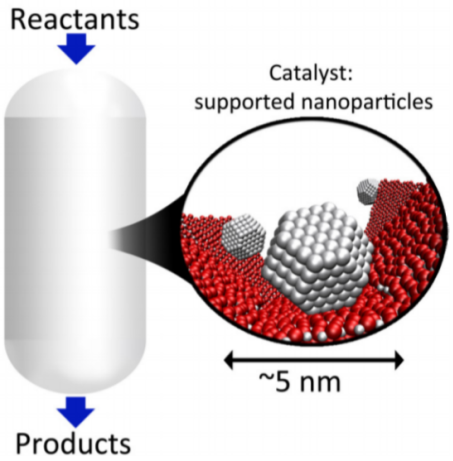

Figure 2.4: Structural representation of an industrial catalyst. The catalytic phase is found inside a reactor into which a flow of reactant gases enter. The products are ejected on the opposite end to which the reactants enter. This reactor can be heated to provide the required energy for the reaction. The nanoparticles are usually synthesized with a mean size of a few nanometers whereas the support is made of bigger particles with a large surface area available for nanoparticle adsorption. Adapted from Mom (2017).

2.1.3 Catalyst Deactivation

Besides optimal selectivity and activity, a long lifespan is highly desirable for catalysts. However, their degradation is unavoidable after many cycles, specially due to the

high temperatures in which most catalytic reactions occur. The time for deactivation can range from seconds to years, depending on the reaction (Moulijn et al., 2001). There are several mechanisms of catalyst deactivation, which can be of chemical, mechanical or thermal nature (Bartholomew, 2001, Forzatti & Lietti, 1999, Argyle & Bartholomew, 2015). Table 2.1 gives a brief description of the main mechanisms. In the simplest models, the catalytic activity is proportional to the number of active sites (Moulijn et al., 2001)

$$k_{obs} = N_T k_{intr} \eta \tag{2.1}$$

where k_{obs} and k_{intr} are the observed and intrinsic rate constants for the reaction (per active site), N_T the total number of active sites, and η the effectiveness factor. Catalyst deactivation can be caused by (i) a decrease of the number of active sites (N_T decreases); (ii) a decrease of the quality of the active sites (k_{intr} decreases); and (iii) a degradation in accessibility to the sites (η decreases). In the present work, sintering and poisoning mechanisms will be discussed in more details.

Table 2.1: Mechanisms of catalyst deactivation (Argyle & Bartholomew, 2015).

Mechanism	Type	Description
Poisoning	Chemical	Strong adsorption of species on active sites which block sites for catalytic reaction, e.g Pt_xPd_{1-x} (x = 1, 0.7, or 0.5) under H_2S sulfidation (Bernardi et al., 2009)
Fouling	Mechanical	Physical deposition of species from fluid phase onto the catalytic surface and in catalyst pores, e.g mechanical deposits of carbon and coke (Lange, 2015)
Thermal degradation and sintering	Thermal Thermal/chemical	Thermally induced loss of catalytic surface area, support area, and active phase-support reactions, e.g growth of Pd nanoparticles above 300 K Tait et al. (2005)
Vapor formation	Chemical	Reaction of gas with catalyst phase to produce volatile compound, e.g $Al_2(SO_4)_3$ formation in CO oxidation by Pt/Al_2O_3 catalyst (Bartholomew & Farrauto, 2011)
Vapor–solid and solid–solid reactions	Chemical	Reaction of vapor, support, or promoter with catalytic phase to produce inactive phase, i.e formation of K_2O film in catalytic combustion by Co/K supported on CeO_2 (Froment & Delmon, 1994)
Attrition/crushing	Mechanical	Loss of catalytic material due to abrasion; loss of internal surface area due to mechanical-induced crushing of the catalyst particle, e.g carbiding of primary Fe_3O_4 particles increases their specific volume and micro-morphology, breaking up these particles (Kalakkad et al., 1995)

2.2 Poisoning

Catalyst poisoning is caused by the strong adsorption of impurities on active sites, making them unavailable for reactions. It is one of the longest known issues in catalysts and, although it has been widely studied, it is still subject of intense research nowadays (Chernyshev et al., 2019). Due to poisoning the number of active sites in Eq. (2.1) decreases as

$$N_T = N_{T_0}(1 - \alpha) \tag{2.2}$$

where N_{T_0} is the initial number of active sites and α is the fraction of the sites poisoned. Furthermore, the poisoner molecules are predominantly present in the outer shell of the cluster. This implies that the accessibility to the sites decreases (η decreases, Eq. (2.1)).

Undesired compounds are very commonly adsorbed into catalyst surfaces. However, if they are easily removable by a thermal treatment, poisoning is reversible and hence less harmful. When the contaminants are strongly adsorbed in such a way that they cannot be easily removed (thermal treatments at low temperatures), the poisoning effect is irreversible and leads to catalyst deactivation (Dunleavy, 2006). Poisoning is not always detrimental, it can be used to enhance selectivity, although usually at the expense of activity (Argyle & Bartholomew, 2015). It is also possible that a strongly adsorbing species leads to an increase in activity, in this case the species is called a promoter instead of a poisoner (Moulijn et al., 2001).

The toxicity of a species will depend on the oxidation state of the catalyst. In general, toxicity increases with increasing atomic or molecular size and electronegativity (Argyle & Bartholomew, 2015). Sulfur species interact with metals via s and p orbitals, and are one of the main poisoning sources for metallic catalysts. It affects many important catalytic processes like hydrogenation, methanation, Fischer–Tropsch synthesis, steam reforming and fuel cell power production. Nevertheless, the rate of sulfur poisoning and hence sulfur resistance varies from catalyst to catalyst and it is a function of catalyst composition (Bartholomew et al., 1982) and reaction conditions (Erekson & Bartholomrw, 1983).

2.2.1 Poisoning Mechanisms

Catalyst poisoning is divided into three categories: selective, anti-selective and nonselective. Selective poisoning involves preferential adsorption of the poisoner at the most active sites at low concentrations. It can be useful when needed to inhibit reactions with

specific functional groups (e.g. selective catalytic reduction of NO_x with NH_3 by Peng et al. (2012)). When sites of low activity are blocked, the poisoning is called anti-selective. If the poisonous species adsorbs to sites without preference, the poisoning is nonselective (Bartholomew, 2001). Fig. 2.5 shows the normalized activity (the reaction rate normalized to initial reaction rate) versus normalized poisoner concentration patterns for each type of poisoning. It is based on the assumption of uniform poisoning of the catalyst surface and surface reaction rate controlling, i.e. negligible degradation of accessibility to the sites. However, for cases where these assumptions do not hold the activity versus poisoner concentration can produce a non-linear curve even for nonselective poisoning (Forzatti & Lietti, 1999).

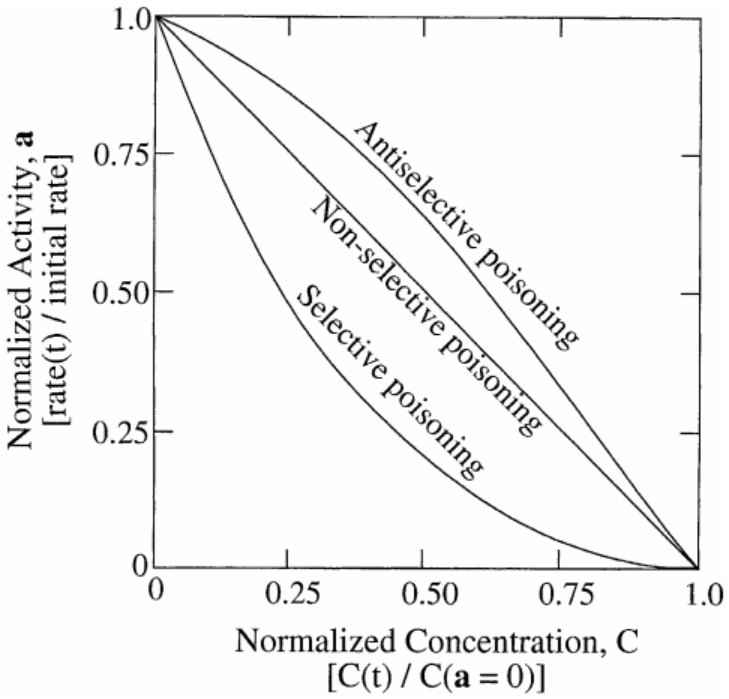

Figure 2.5: Three kinds of poisoning behavior in terms of normalized activity vs. normalized poison concentration (Bartholomew, 2001).

The adsorption of poisonous species affects catalytic activity through competitive adsorption, i.e, the contaminants obstruct adsorption/reaction sites at the metal surface. There are several consequences triggered by the adsorption of poisonous species (Argyle & Bartholomew, 2015, Delmon, 2000). It follows that, by virtue of its strong chemical bond, the poisoner can electronically modify its nearest neighbor metal atoms and possibly its next-nearest neighbor atoms, thereby modifying their abilities to adsorb and/or dissociate reactant molecules. Another effect may be the atomic restructuring at the surface induced by the adsorbed poisoner (Bernardi et al., 2009), possibly causing dramatic

changes in catalytic properties, especially for reactions sensitive to surface structure. In addition, the adsorbed poisoner blocks access of adsorbed reactants to each other and prevents or slows the surface diffusion of adsorbed reactants. In Fig. 2.6, sulfur poisoning of a metal surface on a reaction of ethylene hydrogenation is illustrated. The sulfur atom hinders reactants interaction, while occupying active sites on the metal catalyst.

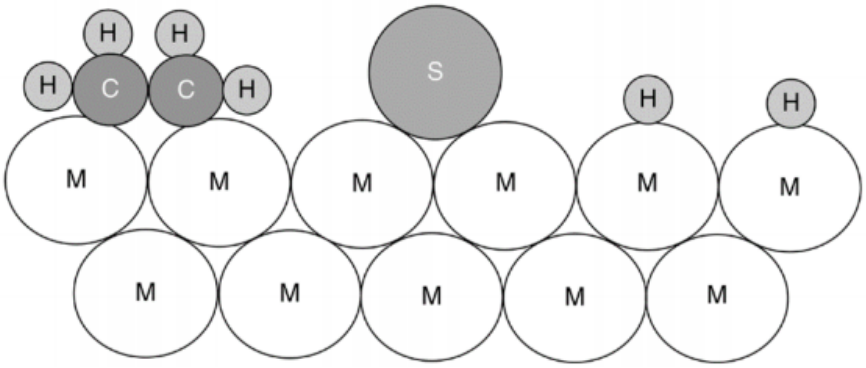

Figure 2.6: Conceptual model of nonselective poisoning by sulfur atoms of a metal surface in ethylene hydrogenation (Bartholomew et al., 1982). In this reaction ethylene (C_2H_4) reacts with H_2 to form ethane (C_2H_6) and is usually catalysed by Ni.

2.2.2 Poisoning Prevention

The main issue originated by poisoning is the loss of active sites, blocked by strongly adsorbed impurities. Hence, it is best prevented by removal of impurities from the feed to levels that enables catalysts operating at its optimal lifetime.

When the environment can not be thoroughly controlled or the presence of possible poisonous species is unavoidable, it may be possible to lower the rate of poisoning through careful choice of reaction conditions that weak the strength of poisoner adsorption, specially with carbon species (Bartholomew, 1982).

Some reactions can present an undesired metal species that produces residuals which lower the catalytic performance. The poisoning of catalysts by metal impurities can be moderated by selective poisoning of the unwanted metal (Parks et al., 1980).

Another strategy that has been employed to reduce the impact of poisoning, particularly for sulfur, is the inclusion of traps (commonly referred to as ”getters” in literature) as part of the catalyst, which act as sacrificial stoichiometric reactants to protect the active metal by preferentially adsorbing the poisoner (Jacobs et al., 2000).

2.3 Sintering

Thermal induced deactivation of catalysts is very difficult to prevent and mostly irreversible. This deactivation process results from: (i) loss of catalytic surface area due to crystallite growth; (ii) loss of support area due to support collapse and of catalytic surface area due to pore collapse on crystallites of the active phase; and/or (iii) chemical transformations of catalytic phases to noncatalytic phases (Argyle & Bartholomew, 2015). While (iii) is a strictly chemical process, which depends on the catalytic and reactive species, (i) and (ii) have a higher range. Processes (i) and (ii) constitute a phenomenon called sintering (also called coarsening, or grain growth in the ceramics literature). In summary, sintering is a process whereby clusters increase their size and reduce their number, and the most detrimental consequence for catalysis is the loss of surface area, which reduces the number of active sites.

Sintering is the predominant mechanism of catalyst deactivation. Its high recurrence is in part because sintering is not limited to specific reactions, although the sintering rates vary according to the reaction (Vogelaar et al., 2010, Teixeira & Giudici, 1999, Sadeqzadeh et al., 2013, Euzen et al., 1999). In addition, catalytic reactions are usually carried out at high temperatures, and sintering rates grow exponentially with temperature. Empirical correlations have been proposed for the catalytic activity as a function of time and temperature,

$$\frac{da}{dt} = -k_d a^m \tag{2.3}$$

$$k_d = k_{d0}\, e^{-E_a/(RT)} \tag{2.4}$$

in which a is the catalytic activity, and k_d the deactivation rate constant (Moulijn et al., 2001). The exponent m often has a value of 2. Besides temperature, which affects sintering rates according to Eq. (2.4), other factors such as atmosphere, metal type, metal dispersion, promoters/impurities and support surface area, texture and porosity also contribute to deactivation. Although many of these parameters can be controlled to some extent, the reaction temperatures are almost impossible to decrease for a given system because it would decrease the catalytic activity as well.

2.3.1 Sintering Mechanisms

For supported nanoparticles, there are two main mechanisms of sintering: crystallite migration and atomic migration (also known as Ostwald ripening). Crystallite migration

involves the diffusion of entire crystallites over the support surface, followed by collision and coalescence (process in which two phase domains come together and form a larger phase domain). Atomic migration involves detachment of metal atoms or molecular metal clusters from crystallites, diffusion of these atoms over the support surface (or through vapor phase), and ultimately, capture by other crystallites (Bartholomew, 2001). The driving force for both mechanisms is the minimization of the total surface energy of the system, and both can act simultaneously. When the cluster adhesion to the support is weak, the coalescence mechanism is favored, whereas the atomic diffusion mechanism is favored for strongly adhered clusters (Jose-Yacaman et al., 2005). Fig. 2.7 illustrate both mechanisms.

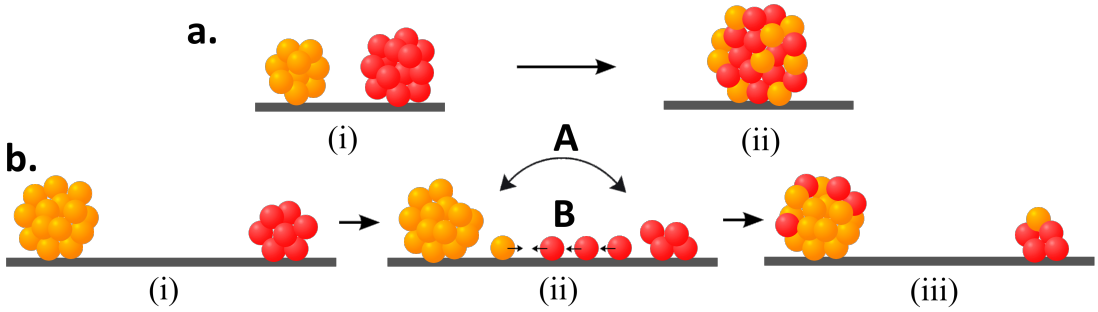

Figure 2.7: Schematic representation of sintering mechanisms. (**a**) Crystallite diffusion: whole clusters migrate along the support surface. When two clusters are close enough (i) a bigger cluster is formed by coalescence (ii). (**b**) Atomic diffusion: Clusters are not required to be in close contact (i). Atoms (or clusters of few atoms) migrate from one cluster to another cluster (ii), in vapor phase (A) or diffusing along the surface (B). The net mass transport is from smaller to larger clusters, because of the lower average coordination of atoms at the surface. Thus big clusters get bigger at the expense of smaller clusters (iii).

Nanoparticles are known to present Brownian motion under high temperatures. Through cluster shape oscillations, provoked by small dislocations of multiple atoms with time, mostly due to thermal energy, small changes in the center of gravity of the nanoparticles occur. Together with the weak adhesion to the substrate, it leads to slight positional shifts of this cluster with each oscillation. Such motions may be described by the classic Frank-Read mechanism (Frank & Read Jr, 1950) for slip. Slip the displacement of one part of a crystal relative to another part along crystallographic planes and directions. The result of the slip is a distortion, viewed as a structural fluctuation, which changes the center of gravity of the nanoparticle on the substrate, thus changing its point of contact. This appears, over time, as small, random displacements across the surface, i.e. Brownian motion, which is microscopically manifested as diffusion. Diffusion coefficients for

supported clusters have been derived based on bubble diffusion theory. Relations between the cluster diffusion coefficient D_p and the surface atomic diffusion coefficient D_s of the type

$$D_p = C\left(\frac{a}{d}\right)^4 D_s \tag{2.5}$$

have been proposed (Gruber, 1967, Harris, 1995), where a is the atomic diameter and d is the cluster diameter, and C is a constant that depends on the cluster shape. Eq. (2.5) indicates that the diffusion of clusters is proportional to the diffusion of its surface atoms and that cluster diffusion grows with decreasing cluster size. The surface atomic diffusion is strongly dependent on temperature and is given by

$$D_s = D_0 e^{-E_a/(RT)} \tag{2.6}$$

where D_0 is a constant, E_a is the activation energy for surface diffusion, R is the gas constant and T is the temperature (Somorjai & Klerer, 1972). Other types of expressions have been proposed in bubble diffusion theory and were later applied to nanocrystal diffusion (Chen & Cost, 1974, Willertz & Shewmon, 1970), where D_p has exponential growth with decreasing d. The variation in migrated distances can be very significant for only few tens of nm difference in cluster size. Considering various models proposed for cluster migration, Harris (1995) suggested that for Pt/Al_2O_3 at 600°C, spherical clusters of $\sim$5 nm in diameter would migrate about 540 nm in 2 h, while large clusters around 24 nm would move at most a distance equal to their diameter.

Coalescence is a process driven by surface energy minimization: the surface area of a coalesced nanoparticle is smaller than that of the sum of the surface areas of the two original nanoparticles. The melting points of nanoparticles are substantially lower than the bulk value, increasing with nanoparticle diameter asymptotically to the bulk value(Buffat & Borel, 1976). The heat created at the coalescing interface melts crystalline material, with heat transferred to the volumes of the coalescing clusters as well as to the surroundings. This facilitates the coalescence mechanism due to the formation of a liquid-like surface layer in the nanoparticles (Sun et al., 2002). In addition to the high percentage of surface atoms, which will conduct the mass transfer through grain boundaries in coalescing clusters, this property makes the coalescence easier for nanoparticles than for macroscopic particles. Fig. 2.8 shows *in situ* sequential TEM images obtained in an 1h window, where the migration and coalescence of Ni nanoparticles supported on $MgAl_2O_4$ under an atmosphere of H_2O:H_2 1:1 at 750 °C can be seen.

Recently, a new mechanism in nanoparticle growth has gained notoriety: the ori-

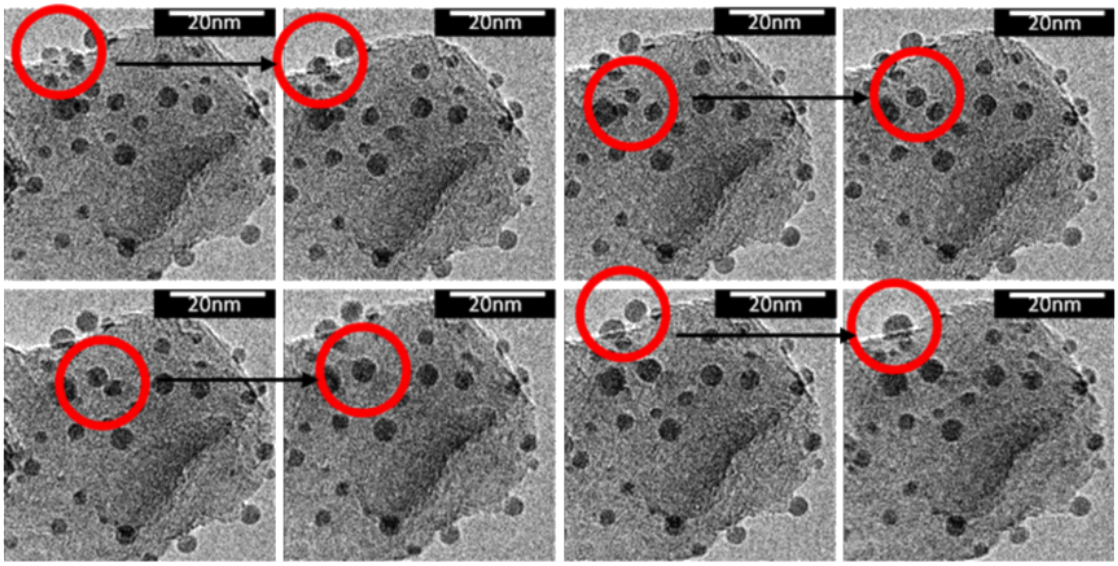

Figure 2.8: *In situ* TEM images of Ni/$MgAl_2O_4$ nanoparticles exposed to H_2O:H2 1:1 atmosphere at 750 °C (Hansen, 2006).

ented attachment mechanism, first proposed by Penn & Banfield (1998). The oriented attachment mechanism propose that, when in contact, nanocrystals rotate to align their crystalline planes while coalescing. For this reason it is also called grain-rotation induced grain coalescence (GRIGC) mechanism. From the thermodynamical point of view, combination in a coherent crystallographic orientation will eliminate the interfaces of nanocrystals, thereby reducing surface energy (Zhuang et al., 2009). When two nanoparticles just attached without self-recrystallization, the curvature radius at the joint is negative. According to the Gibbs–Thompson relation,

$$\mu(R) = \mu_0 + \frac{2\gamma\Omega}{R} \tag{2.7}$$

where $\mu(R)$ is the chemical potential, μ_0 is the chemical potential at a flat interface, γ is the surface free energy, Ω is the volume per atom, and $1/R$ is the curvature radius, the chemical potential at the joint is negative (Zhang et al., 2010). Thus atoms sited on other places are thermodynamically favored to move to the joint. As shown in Fig. 2.9, clusters collide (i), reorient (ii) and coalesce (iii) to a final cluster that ajdusts its morphology to minimize surface energy (iv). Steps (ii) to (iii) are very rapid. But the process from state (iii) to state (iv) might be slow, thus irregular small cluster attachment geometries can be seen when the sizes of the assembling units are small. The orientation of the clusters is not always perfect. Coalescence by oriented attachment can result in nanoparticles with irregular morphologies and typical defects of twins, stacking faults, and misorientations

(Tang et al., 2002, Penn & Banfield, 1998). On the other hand, when the sizes of the assembling units become larger, the possibility of oriented attachment decreases, so there is enough time for nanoparticles to self-organize into round shapes.

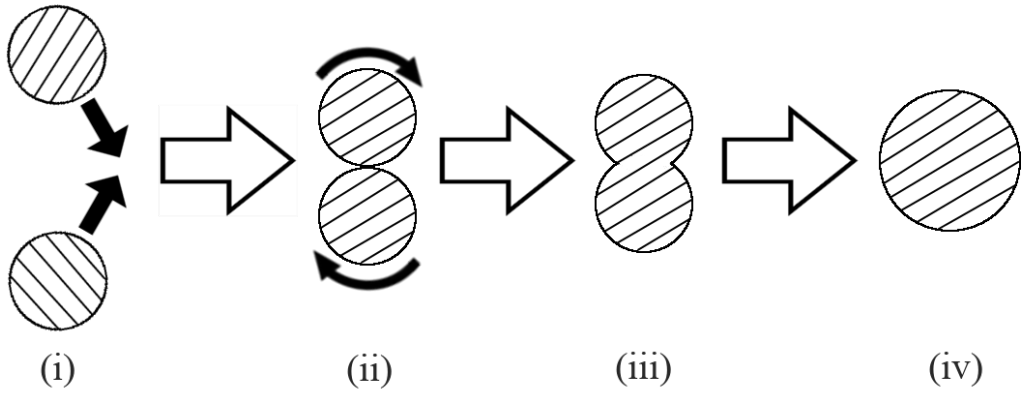

Figure 2.9: Schematics of self-recrystallization following oriented attachment. The diffusing nanoparticles collide (i) and then rotate to have coherent crystallographic orientation (ii). Following reorientation, they coalesce (iii) and adjust morphology (iv) in a process called re-crystallization. Adapted from Zhuang et al. (2009).

Li et al. (2012) used a liquid cell mounted within a high resolution transmission electron microscope (TEM) for the direct *in situ* observation of iron oxide nanoparticle growth by the Oriented Attachment mechanism at room temperature, as seen in Fig. 2.10. The surfaces of adjoining nanoparticles made transient contact at many points and orientations before finally attaching and growing together. Irrespective of how many times nanoparticles made contact, at the time of attachment they either shared the same crystallographic orientation or their orientations were twin-related (a mirrored image of the other particle crystallographic orientation). Molecular dynamics (MD) simulations have been frequently used to study coalescence (Song & Wen, 2010, Zhu, 1996, Ding et al., 2009), and they also show the oriented attachment mechanism. Classical molecular dynamics simulations with a simple two dimensional Lennard-Jones model (Ding et al., 2009) and the Matsui-Akaogi force field (Alimohammadi & Fichthorn, 2009) have demonstrated that the nanoparticles may reorient themselves to match their crystalline orientations at the beginning of the sintering.

In the same way than crystallite migration, the driven force of Ostwald Ripening is the decrease in total surface free energy. The mechanism bears the name of Ostwald, who reported at 1900 the first systematic study of a two phase dispersion coarsening by transfer of matter from small nanoparticles to larger ones (Ratke & Voorhees, 2013).

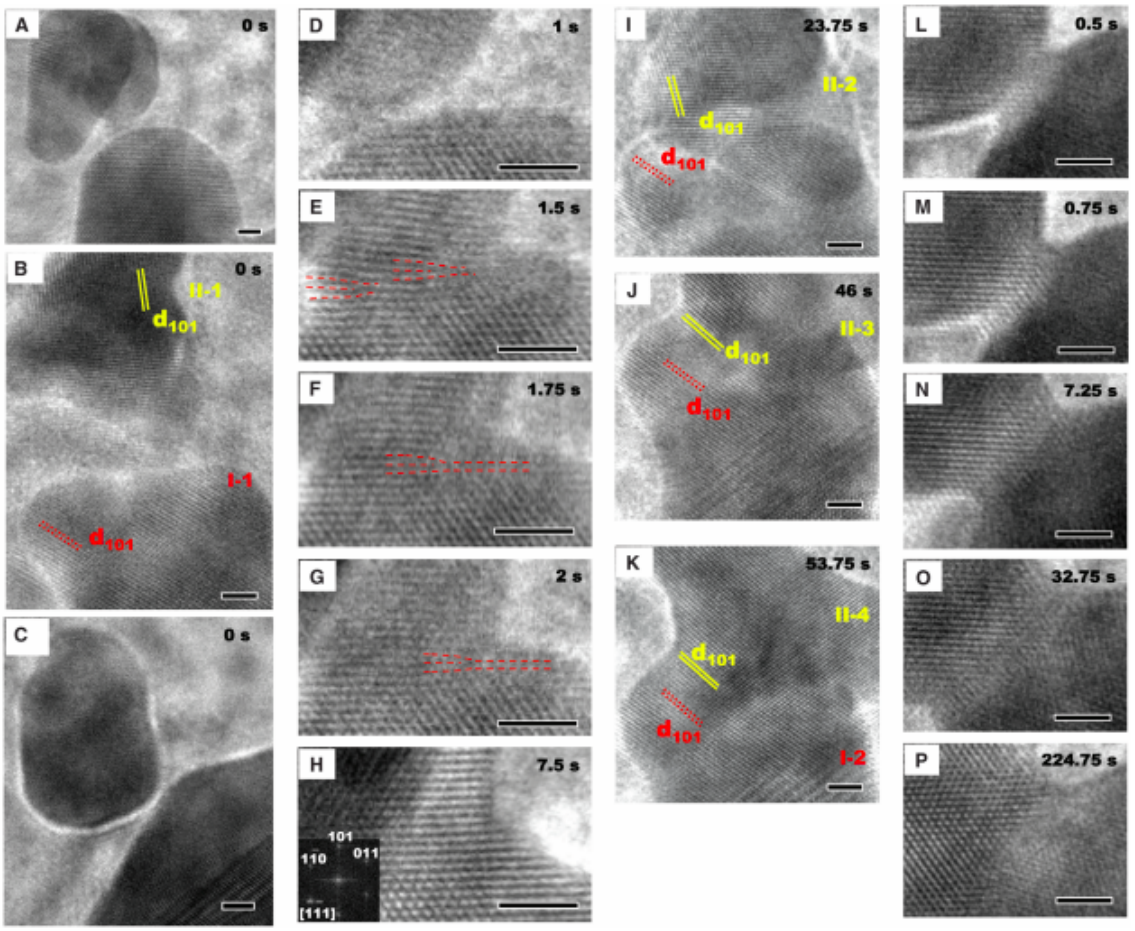

Figure 2.10: Sequences of *in situ* TEM images show the details of the oriented attachment process. (**A**) and (**D** to **H**) Sequence showing attachment at a lattice-matched interface. (A) shows the arrangement of nanoparticles before attachment. The asymmetric nanoparticle in front of the smaller spherical nanoparticle is not involved in the attachment process. (D) to (G) show formation of the interface. Two edge dislocations denoted in (E) to (G) by red dashed lines translate to the right, leaving a defect-free structure in (H). (**B**) and (**I** to **K**) Sequence of images showing relative rotations of nanoparticles during the attachment process, leading to a lattice-matched interface. Nanoparticles I and II have their (–121) plane axes perpendicular to the viewing plane. (**C**) and (**L** to **P**) Sequence showing how the interface expands laterally after attachment. All scale bars are 2 nm. Reproduced from Li et al. (2012).

In the Ostwald model cluster growth occurs as a result of the Gibbs-Thomson equation (Eq. (2.7) which describes the equilibrium concentration at the surface of a cluster. The difference in the chemical potential of the clusters within the distribution will determine the net rate of mass transport. As the chemical potential varies with $1/R$, the net mass transport will be from small to larger clusters. In this way, small nanoparticles tend to vanish and large particles tend to grow (Challa et al., 2011).

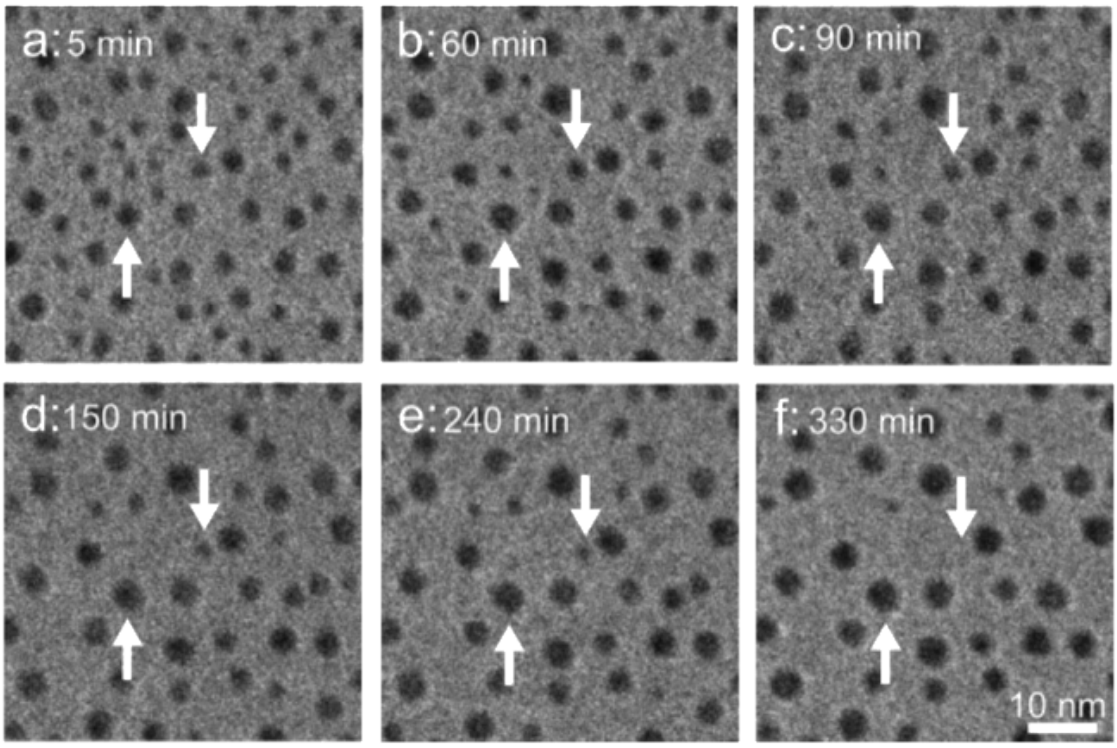

Figure 2.11: (**a**-**f**) *In situ* TEM images of Pt nanoparticles supported on SiO_2 exposed to an O_2 atmosphere under 10 mbar pressure and 650 ° C. The arrows indicate two nanoparticles, one increases in size while the other decreases. The images were taken from Simonsen et al. (2011).

There are two kinds of Ostwald ripening, depending on the mobile species involved: a surface-mediated ripening and a gas-phase-mediated ripening. For the former, atomic species, after being emitted from a nanoparticle, diffuse through the support surface and attach to another nanoparticle. In this case, the interaction between the support and the nanoparticle in comparison to the mobile species has significant effect on sintering (Cargnello et al., 2013). In the gas-phase mediated sintering the volatile species are emitted from nanoparticles and the growth is caused by re-adsorption of those volatile species on large nanoparticles (Plessow & Abild-Pedersen, 2016). Fig. 2.11 shows a time-lapsed TEM image series of Pt nanoparticles, acquired during the exposure to 10 mbar synthetic air at 650 °C, where the Ostwald ripening mechanism is evidenced (Simonsen et al., 2011).

Experimental observations, such as shown in Fig. 2.12, where Ni nanoparticles surface area is measured as a function of time during sintering of Ni/SiO_2 nanoparticles under H_2 atmosphere at 650, 700, and 750°C, demonstrate that sintering is strongly temperature dependent. The absolute melting point temperature T_{mp} has a crucial role in sintering rates since the driving forces for dissociation and diffusion of surface atoms

are both proportional to the fractional approach to T_{mp}. The Hüttig and Tamman temperatures are often used to empirically describe the temperatures at which the two migration mechanisms occur. As temperature increases, the mean lattice vibration of surface atoms increases; when the Hüttig temperature (0.3 T_{mp}) is reached, less strongly bound surface atoms at defect sites (e.g.,edges and corner sites) dissociate and diffuse across the surface, while at the Tamman temperature (0.5 T_{mp}), atoms in the bulk become mobile (Argyle & Bartholomew, 2015).

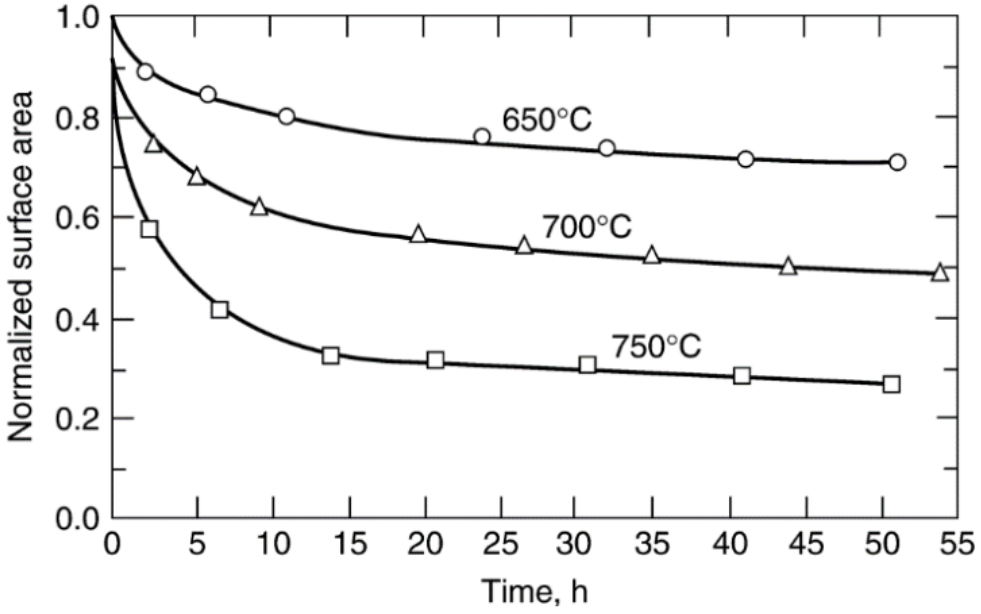

Figure 2.12: Normalized Ni surface area as a function of time during sintering of Ni/SiO_2 in H_2 atmosphere at 650, 700, and 750°C. Reproduced from Bartholomew & Sorensen (1983).

There have been a number of attempts to develop models of sintering. The coalescence models are largely based on the classic work of Smoluchowski (1916), describing the cluster density due to binary encounters of diffusing clusters. Whereas, the Ostwald ripening models go back to the works of Lifshitz & Slyozov (1961) and Wagner (1961) on the condensation of droplets. Theories for the migration and coalescence of supported metal crystallites (Ruckenstein & Pulvermacher, 1973), and the mean growth of clusters by Ostwald ripening (Voorhees, 1985) have been accomplished and both result in a growth law of the type

$$\langle d \rangle^n - \langle d_0 \rangle^n = kt \tag{2.8}$$

where $\langle d \rangle$ is the mean diameter after time t, $\langle d_0 \rangle$ is the initial mean diameter, n an integer,

and k a temperature dependent constant.

Although these models are widely used, studies have shown that they do not accurately predict the sintering behaviour of very small nanoparticles. Campbell et al. (2002) showed that taking into account the very large change of energy per metal atom as a function of size, measured for the first time by single-crystal adsorption microcalorimetry, the sintering behaviour of nanoparticles is better described. The surface energy increases substantially as the radius decreases below $\sim$3 nm, which could be expected because the average coordination number of the surface atoms decreases. This makes Eq. (2.7) overpredict the stability of small clusters. Therefore, for more accurate models, it seems necessary to include a proper treatment of the cluster size effect on $\mu(R)$. Furthermore, stochastic cluster models have been implemented to simulate nanoparticle sintering for both coalescence (Sander et al., 2009, Morgan et al., 2005, Akhtar et al., 1994) and Ostwald ripening (Schwind & Ågren, 2001).

The regime of each mechanism should be determined by their activation energy. However, it is highly difficult to observe the reaction stages in which each sintering mechanism prevails over the other, since *in situ* TEM imaging of sintering processes are limited to small areas and time frames. In addition, there are several factors that unpredictally influence on sintering rates (even the electron beam in TEM measurements may have some influence). Previous literature (Beck & Carr, 1988, Wynblatt & Gjostein, 1975) has suggested that the operative mechanism may change from cluster migration, in the early stages when the nanoparticles are very small, to Ostwald ripening, when the clusters become large and effectively immobile. However, recent evidence of early disappearance of small clusters are being related to Ostwald ripening at initial stages of sintering (Hansen, 2006). Because the sintering dynamics is very dependent of the metal, support, and gas atmosphere, the precise stages of sintering are still undetermined, although the mechanisms are known.

2.3.2 Sintering Prevention

There are three main approaches used for sintering prevention: (a) modification of the interface between clusters and between clusters and the support, (b) modification of the metallic nanoparticle electronic structure by bonding with other metals (*alloying*) and (c) modification of the support by nanostructuring.

(a) Cluster-cluster and Cluster/support Interface Modification

Nanoparticle coating is a method that modifies the interface between clusters and it is the most widely used for sintering prevention. To inhibit sintering, the nanoparticles are usually coated by a porous oxide shell, which acts as shield. This shell can be inert (Joo et al., 2009, Park et al., 2008, Vystavel et al., 2005) or catalytically active (Lee et al., 2016). SiO_2, ZrO_2, Al_2O_3 are among the most used inert oxide shells, while CeO_2 is widely used for active shells. CeO_2 exhibits high surface ion mobility and a great capacity to store and release oxygen atoms (Trovarelli, 1996), where the Ce(III)/Ce(IV) ratio can be modified by tuning the oxygen vacancies amount of CeO_2 (Della Mea et al., 2017). Although the coating method is effective in reducing sintering rates, these coatings inevitably cover a portion of the nanoparticles surface, thus harming reactivity. Furthermore, they are susceptible to decomposition at high temperatures and the inherent interconnectivity between pores often serves as a sintering pathway for metal nanoparticles (Lee et al., 2016). The nanoparticle coating is accomplished in the synthesis and typically produces a core-shell structure with a nanoparticle in the core region and the oxide in the shell region. The oxide shell must be permeable to expose the active sites in the nanoparticles. Fig. 2.13 shows TEM images of Pt nanoparticles encapsulated by SiO_2 after calcination at 350, 550 and 750 °C, where the silica shell was confirmed to present mesopores 2-3 nm size (Joo et al., 2009). Surfactants are also employed in nanoparticle synthesis to produce thermally stable nanoparticles, and many times as a template to produce oxide shells. Surfactant coatings can not hold temperatures much higher than 300 °C (Ding et al., 2004). In applications where the bulk properties are important, coating is a reliable method. However, for catalysis, where the nanoparticles surface area is of extreme importance, surfactants passivate surface active sites of the nanoparticles and are often accompanied by decrease in mass and/or energy transfer, resulting in diminished catalytic activity. Hence, the encapsulation method restricts catalysis by steric effects (Suryanarayanan et al., 2004), with exception of very specific cases in which the shell can be catalytically active. On the other hand, active shells are made of oxides instead of metal surfaces, then changing the reaction pathways of a given catalytic reaction.

(b) Alloying

As previously mentioned, the melting point of the specific metal nanoparticle plays a key role in sintering. Metals with higher melting points tend to show better thermal stability. Hence, strategies to increase the melting point of a nanoparticle can be expected to mitigate sintering (Cao et al., 2010). The main strategy to achieve this is by combining

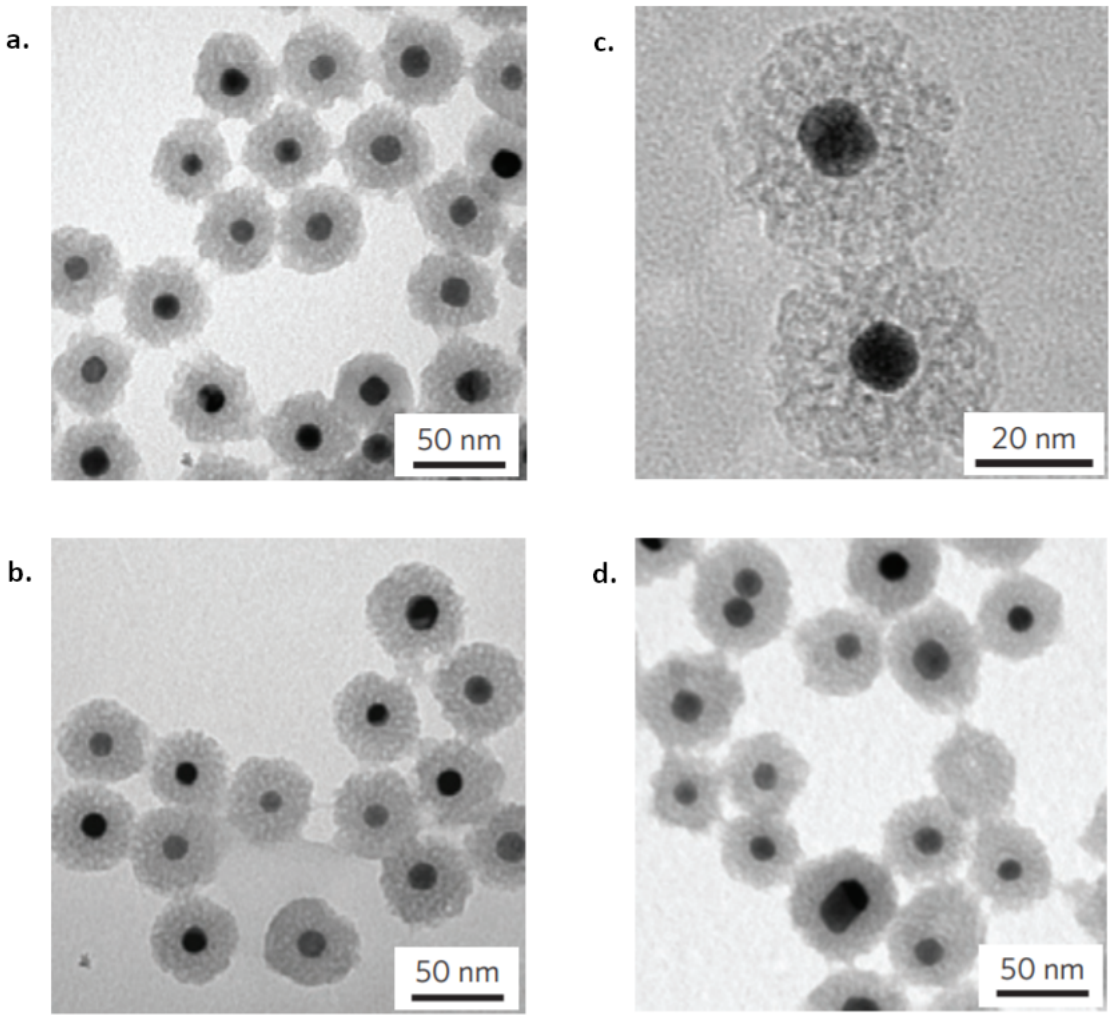

Figure 2.13: TEM images of Pt nanoparticles encapsulated by SiO_2 shells after calcination at (**a**, **b**) 350°C, (**c**) 550 °C and (**d**) 750 °C. Adapted from Joo et al. (2009).

a metal nanoparticle with another metal whose melting point is higher. This process is called alloying. The bimetallic clusters thus formed will have different chemical composition and atomic arrangements in relation to separated nanoparticles. Cao & Veser (2010) have synthesized a thermally stable nanocatalyst with a PtRh alloy. The authors showed that the thermal stability of these nanoparticles depends critically on the Pt/Rh ratio, with higher Rh contents leading to increased thermal stability. However, thermally induced de-alloying phenomena are not rare (Jeon et al., 2010), causing metal clusters to sinter. Moreover, this strategy limits the range of available chemical compositions and therefore their activity and/or selectivity.

(c) Support Nanostructuring

Finally, there is an approach to prevent sintering which is based on designing supports that can restrain nanoparticles diffusion. The easiest and most common approach is to produce a mesoporous support (Gabaldon et al., 2007). The presence of pores in the scale of a few to a few tens of nanometers creates confining spaces for the nanoparticles, supressing their mobility (De Vos et al., 2002). These pores must be stable under high temperature reactions for this procedure be applicable for catalysis. Some issues like pore collapse and the appearance of interconnectivity between pores are prone to happen at high temperatures and enables cluster and atomic migration (Cao et al., 2010). Beyond mesoporous supports, there are several support topologies which can overcome or hinder sintering, although the practical tailoring of these supports are usually challenging. Carbon nanotubes have been used as an alternative to limit nanoparticle collisions (Pan et al., 2007), although it does not prevent sintering from happening, only delays it. Fig. 2.14 shows the advantage of a design with wide-mouthed compartments in preventing sintering by optimizing the distance d between clusters (Liu et al., 2017).

All the alternatives above have limitations in applications for catalysis. Sintering is still an open issue and research aimed to avoiding it with minimal loss of catalytic activity and selectivity, little change in nanoparticles chemical composition and ease of reproduction is of great importance. In this work it is presented a new proposal for preventing sintering without the need of encapsulation, alloying or nanostructuring of supports.

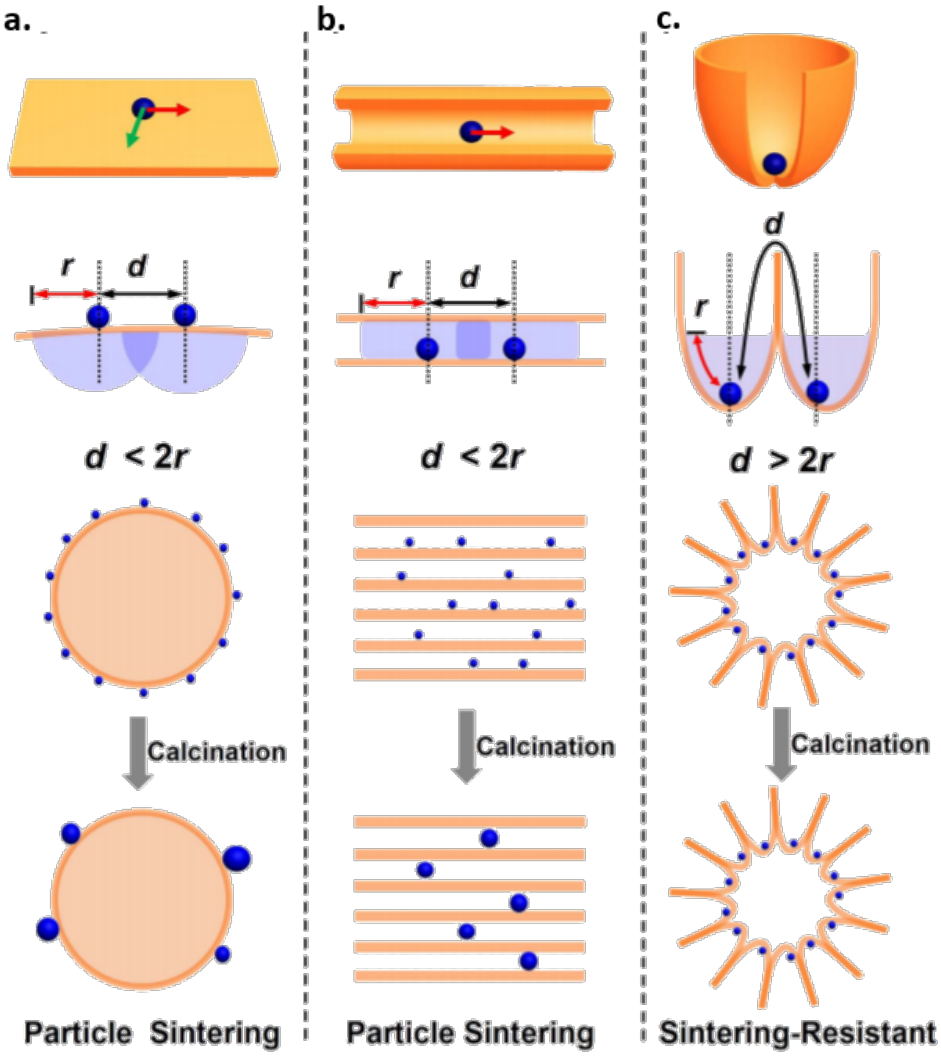

Figure 2.14: Schematic illustration of the relationships between support topology and cluster sintering. Nanoparticles dispersed on (**a**) the solid supports with two-dimensional open surface, (**b**) the porous supports with one-dimensional nanochannels, and (**c**) the supports enriched with wide-mouthed compartments at the surface. d stands for the cluster-to-cluster traveling distance of neighboring two clusters, while r denotes the migration length of individual clusters at a given temperature. Reproduced from Liu et al. (2017).

Chapter 3

Experimental and Numerical Techniques

In this chapter the experimental and numerical techniques used in this work are described. Their theoretical foundations and basic instrumentation are presented as well a brief historical background.

3.1 X-Ray Diffraction

X-Ray diffraction (XRD) by crystals is known since 1912, when it was discovered by Max Laue and earned him a Nobel Prize (Eckert, 2012). XRD is used for non-destructive analysis of materials and it consists on focusing a X-ray beam into a crystalline sample varying the incidence angle or the X-ray wavelength and detecting the intensity of the diffracted X-rays. Since the wavelength range of X-rays can reach the atomic scale, their interaction with a material is sensible to its atomic arrangement. Therefore, the diffraction pattern makes a reliable fingerprint for crystal structures.

The interatomic distance in materials is around a few Å, therefore it is needed incident radiation with wavelength of the same order to produce significant diffraction effects related to the atomic structure. One year after Laue's discovery of X-ray diffraction, W. L. Bragg described X-ray diffraction by representing crystals as a set of parallel atomic planes in which incident radiation is scattered. Bragg et al. (1913) showed that coherent X-rays scattered from these parallel crystal planes interfere each other.

Let d be the distance between two crystal planes and θ the angle between the incident X-ray and the material surface. Fig. 3.1 shows that the scattered X-rays from both planes will have an optical path difference of $2d\sin\theta$. Therefore, the condition for constructive interference is that the optical path difference be equal to an integer multiple of the

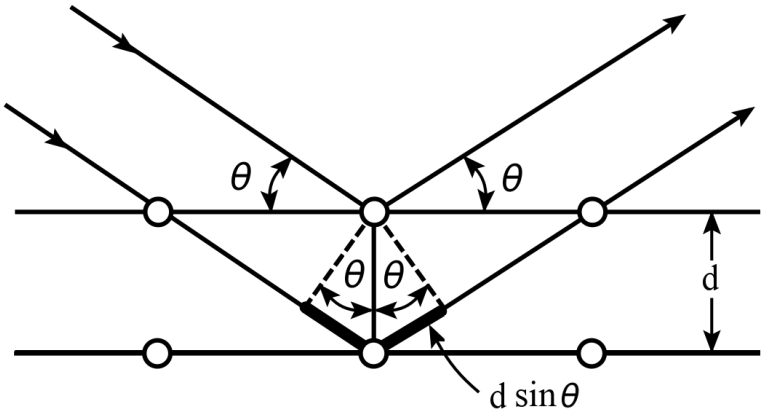

Figure 3.1: Illustration of X-rays scattering by parallel planes.

incident X-ray wavelength. Thus, Bragg's Law is formulated:

$$n\lambda = 2d\sin\theta \qquad\qquad n = 1, 2, 3, ... \tag{3.1}$$

The interplanar distance d is an structural characteristic of the material, while λ and θ can be experimentally controlled. However, a crystal structure contains several crystal planes with different interplanar distances. The characterization of a material using the Bragg's Law can be conducted varying λ or θ. The experimental methods of X-ray diffraction are distinguished by the quantity varied. In the Laue's method, λ varies while θ is fixed. In the rotating crystal method λ is fixed and θ is varied by rotating a single crystal around an axis. In the powder method, λ is fixed and θ is varied. However, the way θ is varied is significantly different from the rotating crystal method. The crystal to be examined is reduced to a very fine powder, so that each particle of the powder is a tiny crystal, or assemblage of smaller crystals, randomly oriented with respect to the incident beam. Then θ is varied by changing the incidence angle of the X-ray beam on the sample. The result is that every set of lattice planes in the material will statistically contribute to the diffraction pattern (Cullity & Stock, 1978). One of the most common geometry configurations for powder measurements, and that is used in this work, is the Bragg-Brentano geometry (Fig. 3.2). In this configuration, the X-rays source and the detector are scanned synchronously such that the X-ray incidence angle and the diffracted angle remain the same throughout the scanning. Therefore, in such a geometry only the crystal planes which are parallel to the sample surface may be probed. The detector will record intensity maxima at the θ angles that fulfill Bragg's Law for each crystal plane in the sample. The diffraction intensity as a function of the scattering angle 2θ consitutes the diffraction pattern, also called diffractogram (Fig. 3.3). The maxima regions are denominated Bragg reflections,

that are located in the Bragg's angles. The diffraction pattern is usually exhibited as a function of 2θ, which is the angle between the incident and diffracted beams.

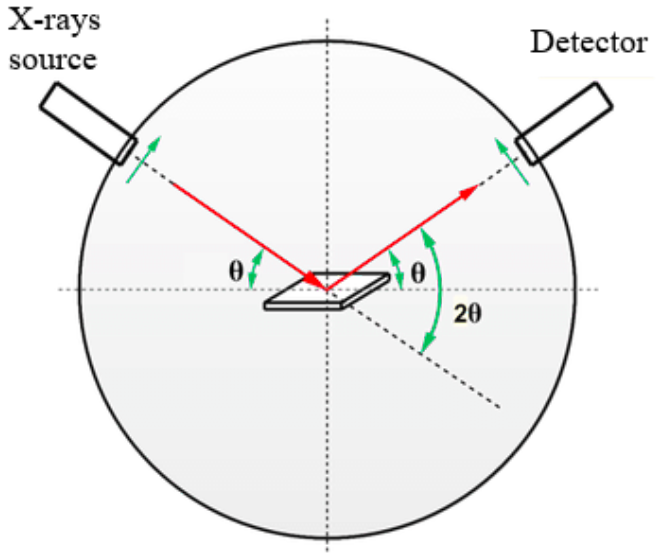

Figure 3.2: Schematic representation of the Bragg-Brentano Geometry used in XRD measurements. Adapted fom Raza (2017).

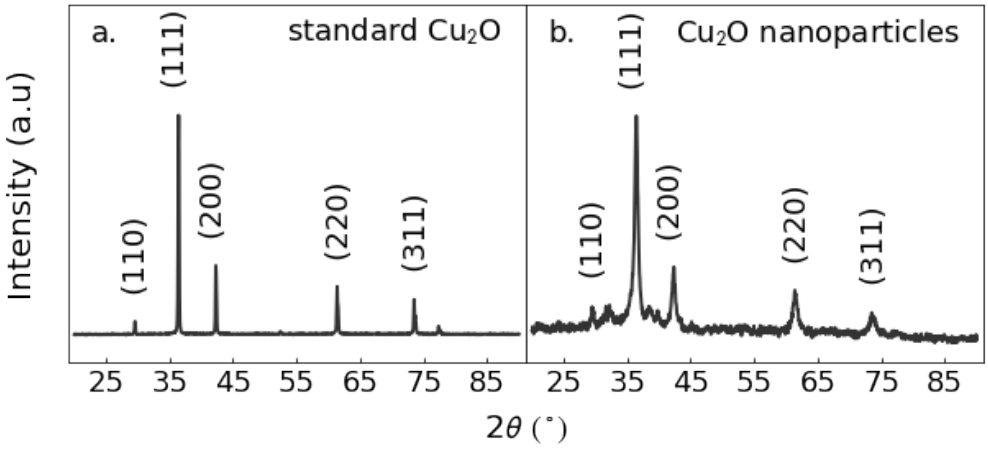

Figure 3.3: Diffraction patterns of (**a**) standard Cu_2O and (**b**) Cu_2O nanoparticles.

Any characteristic that makes a crystal deviate from a perfect lattice will shape the diffraction profile. (Fultz & Howe, 2012). The finite size of a real crystal, for example, turns the diffraction lines into peak-shaped functions. The smaller the size of a crystal the broader the peaks, due to the number of crystal planes involved in diffraction. Cullity & Stock (1978) present the following construction to illustrate this relation: suppose, for example, a crystal with finite width t, measured in the perpendicular direction to $(m + 1)$

atomic planes, as demonstrated in Fig. 3.4. Let θ_B be the angle which exactly satisfies the Bragg's Law, then rays **A, D, ..., M** arrive at planes 0,1,...,m at a θ_B angle, so that the rays **A', D', ..., M'** which are scattered at a $2\theta_B$ angle are completely in phase and produce constructive interference. Now, for rays reaching the planes at angles slightly different than θ_B the optical path difference which gives total destructive interference lies deep in the crystal. If rays **B** and **L** arrive at an angle θ_1, the scattered ray **L'**, from the m^{th} plane, will be $m + 1$ wavelengths out of phase from **B'**. Hence, there must be a crystal plane between the surface and the m^{th} plane for which there is total destructive interference, given that the optical path difference between the incident and scattered rays gradually grows with depth. Therefore, there will be pairs of crystal planes for which the scattered rays at $2\theta_1$ cancel each other, in such a way that rays scattered by the upper half of the crystal cancels those scattered by the lower half. Thus, θ_1 constitutes an angle for which the diffracted ray has null intensity. The same logic applies to $2\theta_2$, being the angle for which a ray **N'**, scattered by the mth atomic plane, is $m - 1$ wavelengths out of phase with ray **C'**, scattered at the surface. These are defined as the limiting angles $2\theta_1$ and $2\theta_2$, where the intensity drops to zero. For angles between them, the intensity is not null but lower than for $2\theta_B$. For an infinite crystal, there will always be pairs of cancelling planes at an infinitesimal distance from θ_B, thus the Bragg reflections are Dirac delta functions (Fig. 3.5.a). For a finite crystal, the smaller the m, the larger the extensions $2\theta_1$ - $2\theta_2$ (Fig. 3.5.b). Since less crystal planes are involved in the diffraction process, only partial destructive interference is produced in angles close to θ_B.

The finite size will then introduce a broadening B in the diffraction lines (Fig. 3.5.b). Hence, writing the Bragg's Law (3.1) for the entire thickness of the crystal gives

$$2t \sin\theta_1 = (m+1)\lambda \tag{3.2}$$

$$2t \sin\theta_2 = (m-1)\lambda \tag{3.3}$$

which are combined to

$$2t \cos\left(\frac{\theta_1+\theta_2}{2}\right) \sin\left(\frac{\theta_1-\theta_2}{2}\right) = \lambda. \tag{3.4}$$

But θ_1 and θ_2 are nearly equal to θ_B, so $\theta_1 + \theta_2 \simeq 2\theta_B$. Therefore with this approximation the length of a crystallite domain becomes

$$t = \frac{K\lambda}{B\cos\theta_B} \tag{3.5}$$

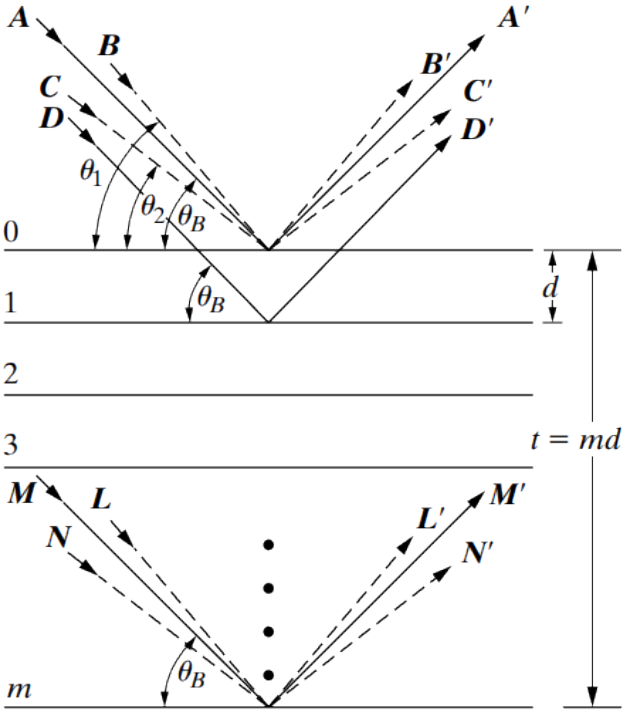

Figure 3.4: Schematic representation of $m+1$ crystal planes in a crystal of size t. Adapted from Cullity & Stock (1978)

which is known as Scherrer's equation. The proportionality constant K is here introduced *a posteriori* to account for different cluster geometries and specific choices of peak width measurements. This equation gives the mean volume-weighted crystallite size, since the diffraction pattern contains contributions from several crystal planes along the depth of a cluster, and clusters with several sizes are measured.

Several other factors influence on the diffraction profile, not only in the Bragg's reflections shape, but also in its position and intensity (Cullity & Stock, 1978, Warren, 1990). The polarization factor describes the effects in the diffraction intensity when the incident X-ray is polarized. When electromagnetic waves are scattered by a crystal plane, the beam component which has its polarization vector parallel to the plane is scattered without losing intensity. The portion which is perpendicular to the plane is attenuated by a factor $\cos^2 2\theta$. The Lorentz factor is a geometrical correction due to X-ray beam divergence and partial monochromatization. The intensity of the scattered beam is proportional to the Lorentz Factor, given by $1/(4\sin^2\theta\cos\theta)$. The multiplicity factor is the number of equivalent crystal planes, i.e, the number of planes with the same interplanar spacing in a family of planes. This factor multiplies the diffraction intensity. The absorption factor describes how a sample absorbs the incident radiation. This induces an exponential

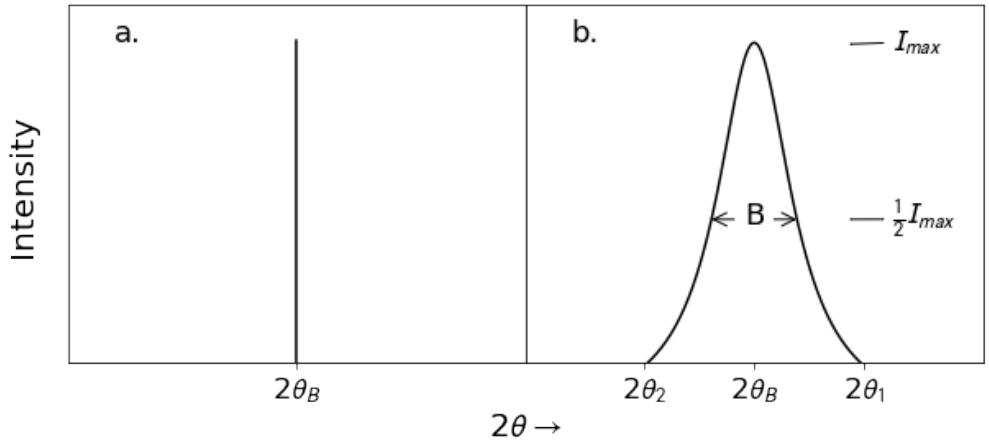

Figure 3.5: Schematic effect of finite cluster size on diffraction curves, where I_{max} is the maximum intensity and B is the full width at half maximum intensity (FWHM). Adapted from Cullity & Stock (1978).

attenuation in intensity as a function of the distance traveled by the X-ray inside the material. The temperature factor describes the effects in the diffraction lines due to the thermal oscillation of the atoms. The main effects of temperature in the XRD patterns are expansion of the unit cell; changing of the Bragg's angles; attenuation of the intensity of the diffracted X-rays, due to the atomic disorder induced by the temperature; increase in the background between consecutive Bragg reflections. The intensity attenuation is not trivial but it can be modeled as exponentially dependent of the mean square atomic displacement.

X-rays are not scattered only by electrons or single atoms, but by a collection of periodically arranged atoms. This introduces a dependence of the scattered intensity with the Miller indices:

$$I(hkl) \propto F^2(hkl)\frac{\sin^2(U_1 h\pi)}{\sin^2(h\pi)}\frac{\sin^2(U_2 k\pi)}{\sin^2(k\pi)}\frac{\sin^2(U_3 l\pi)}{\sin^2(l\pi)} \tag{3.6}$$

where U_1, U_2 and U_3 are the numbers of the unit cells in the corresponding directions and $F(hkl)$ is called the structure factor, which describes the scattering function of one unit cell (Pecharsky & Zavalij, 2008). The structure form is defined as

$$F(hkl) = \sum_j f_j e^{-2\pi i(hx_j + ky_j + lz_j)} \quad ,$$

where $\vec{r_j}$ is the postion of the j^{th} atom in the unit cell, f_j is the form factor of the j^{th} atom and h, k, l are the Miller indices. The form factor is defined as the ratio between the

scattering amplitude by a single electron to the scattering amplitude of the single atom.

The theoretical positions of a Bragg reflection can be calculated from the Miller indices of the respective crystal plane if the unit cell parameters are known. The Bragg's Law can be more conveniently written as

$$2\theta_{hkl} = 2\arcsin\left(\frac{\lambda}{2d_{hkl}}\right) \tag{3.7}$$

For an orthorombic system, for example, we have:

$$d_{hkl} = \left(\frac{h^2}{a^2} + \frac{k^2}{b^2} + \frac{l^2}{c^2}\right)^{-1/2} \tag{3.8}$$

There are two crystallographic parameters which define the basic structure of a diffraction pattern: the unit cell content and the spatial distribution of atoms in the unit cell. Thus a theoretical diffraction line pattern can be simulated using known crystallographic information. If the contributions of the instrumental and specimen conditions are well modeled, the convolution of the individual functions fits the data. However, *ab initio* modeling is difficult and most often a fit is performed using various empirically selected peak shape functions and parameters.

3.1.1 Rietveld Refinement

The Rietveld Refinement is a fitting method that seeks to use the entire diffraction profile, and not just the integrated intensities of the Bragg reflections, to refine the parameters of the structural model (Rietveld, 1969). It requires prior knowledge of the possible crystal structures contributing to the pattern and the instrumental parameters involved in the measurements. Initially the indexing of the XRD pattern is conducted with a database. Then, an initial model is built for each phase. However, instrumental parameters and specimen properties affect the pattern components, producing Bragg reflections with peak like shapes. Proposing a peak function to describe the Bragg reflections, a non-linear least square fitting method can be used to fit the profile. Crystal structure, instrumental, peak function and background function parameters can be involved in the fit. Since the number of parameters can be very high in the full profile fitting, the optimization is done in cycles of few non-fixed parameters until reaching a satisfactory result. This is called a refinement procedure.

After the convergence of the refined parameters, the full diffraction profile is given by the sum of the calculated profiles of each phase. Then the final parameters give valuable information about each component. Fig. 3.6 summarizes the described process

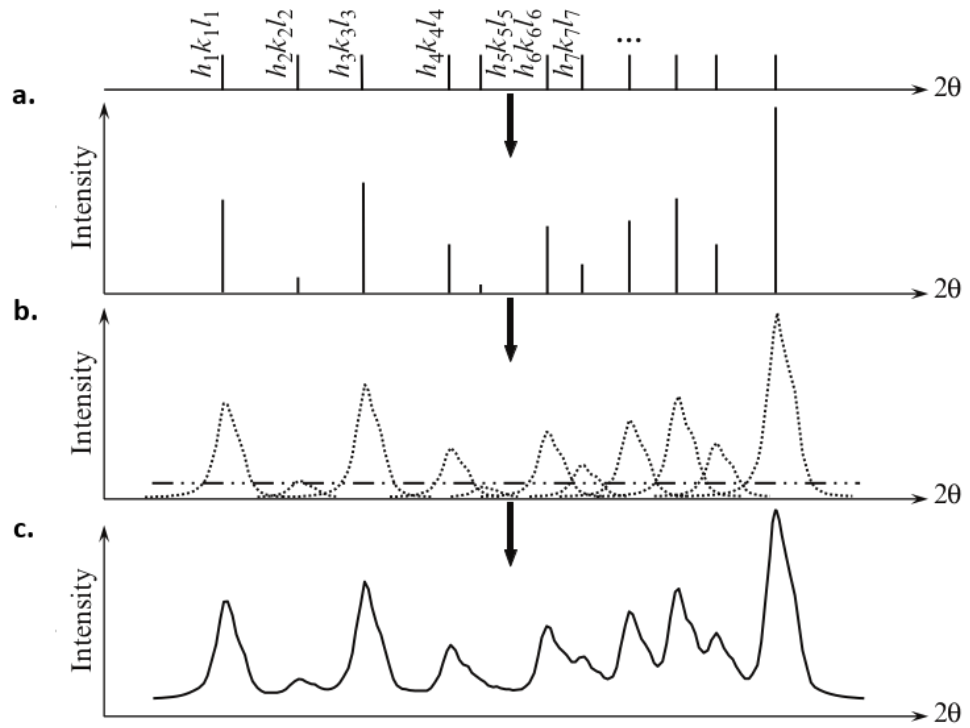

Figure 3.6: (**a**) Only Bragg reflections positions are represented by the vertical bars of equal length. (**b**) The intensity of the Bragg reflections is calculated, indicated by the length of the bars. (**c**) Peak shapes have been introduced, which are the convolution of instrumental and specimen contributions with appropriate peak-shape functions. A constant background is indicated by the dash-double dotted line. (**d**) The resultant powder diffraction pattern is the sum of all components shown separately in c. Adapted from (Pecharsky & Zavalij, 2008).

of simulating a diffraction profile to adjust the data. It is important, however, to remember that the Rietveld method requires a model of a crystal structure and by itself offers no hints on how to create such a model from first principles. Thus, the Rietveld technique is nothing else than a powerful refinement and optimization tool, and requires knowledge of the possible structures in a sample and the limiting values of the refined parameters.

3.2 X-Ray Photoelectron Spectroscopy

X-ray Photoelectron Spectroscopy (XPS) is one of the most used techniques for defining the elemental composition of a solid surface. It probes a depth around 5 nm from the surface of any solid (van der Klink & Brom, 2000). XPS analysis also reveals the chemical environment where the respective element is present, elucidating its oxidation state and existent bonds. It origins from the photoelectric effect, which was explained

by Einstein (1905), that arises from the energy transfer from photons to bound electrons if this energy is greater or equal to the electronic binding energy to the respective atom summed to the material's work function, which represents the minimum energy necessary to remove an electron from it, i.e., the difference between the Fermi energy E_f and the vacuum energy E_{vac}. In this case, the electron is ejected from the atom and this electron is called photoelectron. The kinetic energy (K.E.) of this photoelectron is given by

$$K.E. = h\nu - \phi - B.E. \tag{3.9}$$

were $h\nu$ is the X-ray photon energy, $B.E.$ is the electronic binding energy and ϕ is the material's work function.

XPS is a very straightforward technique. It consists of focusing a X-ray beam into a sample and measuring the kinetic energy of the photoelectrons emitted. Monochromatization is not mandatory, as long as the X-ray spectrum has narrow lines. The kinetic energy is directly related to the binding energy by Eq. 3.9, which allows identify the elemental composition and chemical components present in the sample's surface. However, not only photoelectrons can be emitted from a sample irradiated by X-rays. When a core electron is removed, leaving a vacancy, an electron from a higher energy level may occupy this vacancy releasing energy. Although most often this energy is released in the form of a photon (fluorescence), the energy can also be transferred to another electron, which is ejected from the atom. This second ejected electron is called Auger electron. The photoelectron peaks are labeled according to the electronic level, as seen in Fig. 3.7.a. The Auger peaks are labeled with the electronic levels of the core hole, the bound electron that occupies the core hole and the Auger electron. For example, in Fig. 3.7.a the core hole resides in the O $1s$ level (K notation), while the electron that occupies the core hole and the Auger electron come from the O $2p_{1/2}$ and $2p_{3/2}$ levels (L_2 and L_3 notation, respectively). Fig. 3.7.b. shows this Auger emission identified as O KL_2L_3.

The depth scale of XPS measurements is controlled by the electronic inelastic mean free path, which is dependent on the kinetic energy of the photoelectron emitted. The electronic inelastic mean free path is defined as the mean distance traveled by an electron before suffering an inelastic collision. As Fig. 3.8.a shows, when a photoelectron is emitted from a depth Z within the material, if its inelastic mean free path is big it will have a higher probability of leaving the material without losing energy, whereas for a small inelastic mean free path it will have a higher chance of leaving the material with energy loss or not leaving at all. In Fig. 3.8.b is shown the universal inelastic mean free path curve, where it can be seen that for photoelectrons traveling in most materials the inelastic mean free path is around 10 Å for the typical kinetic energies of photoelectrons

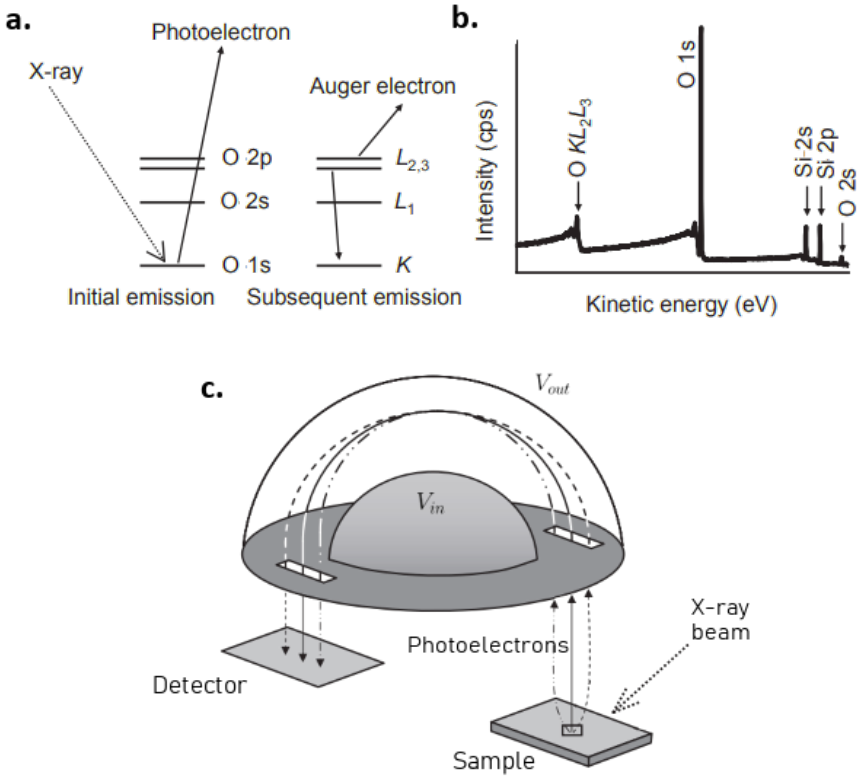

Figure 3.7: (**a**) Schematic example of a photoelectron and subsequent Auger electron emission. (**b**) Spectrum collected from a silicon wafer bearing a surface oxide as analyzed under Mg Kα irradiation. (**c**) Scheme of a concentric hemispherical analyzer. Adapted from van der Klink & Brom (2000).

in the XPS technique. At a distance of around three times the inelastic mean free path, 95% of all photoelectrons are scattered before reaching the surface. Due to this small value, XPS probes mostly the surface of materials.

As depicted in Fig. 3.7.c, the XPS instrument consists mainly in an X-ray source, an electron analyzer and a detection system. The electron analyzer consists typically on two concentric hemispheres, one inside the other, of radius R_{in} and R_{out}. Applying specific potentials V_{in} and V_{out} to these hemispheres results in the deflection of photoelectrons of specific kinetic energy arriving in the multichannel detector, which is coupled to a photomultiplier. The photoelectrons are accelerated or retarded to reach this user-defined kinetic energy which is the energy that the photoelectrons must have when passing through the electron analyser in order to reach the multi-channel detector. A schematic illustration is shown in Fig. 3.7.c. In this way, the number of emitted electrons as a function of the kinetic energy can be counted.

Considering the experimental setup of the XPS measurements, the relation between kinetic energy and binding energy should be modified to

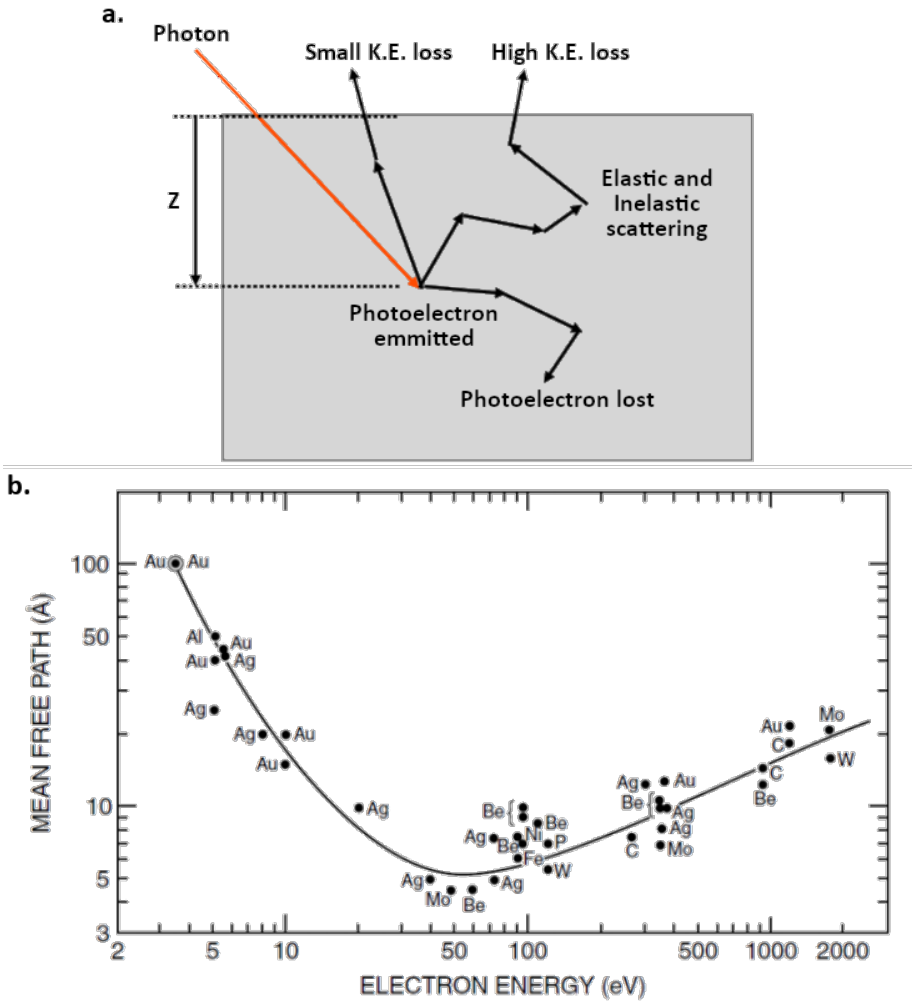

Figure 3.8: (**a**) Schematic representation of the photoelectron scattering after emission, where Z is the material depth. (**b**) Universal curve of electronic inelastic mean free path. Adapted from Somorjai (1990).

$$K.E._{XPS} = h\nu - \phi_{XPS} - B.E._{XPS} \, . \tag{3.10}$$

The change relies on the use of the electron analyzer work function (ϕ_{XPS}) instead of the sample one (ϕ_s). It occurs because if a conductive sample is in physical contact with the instrument, the Fermi level of the instrument and the sample aligns. Then only ϕ_{XPS} needs to be known, as shown in Fig. 3.9.

In XPS analysis, photoemission never comes from an unperturbed free atom, hence the $B.E._{XPS}$ in Eq. (3.10) should not be expected to describe such a scenario. In fact, it is usually studied the variations in binding energies and signal intensities and widths when comparing data. There are several factors affecting the measured electronic binding

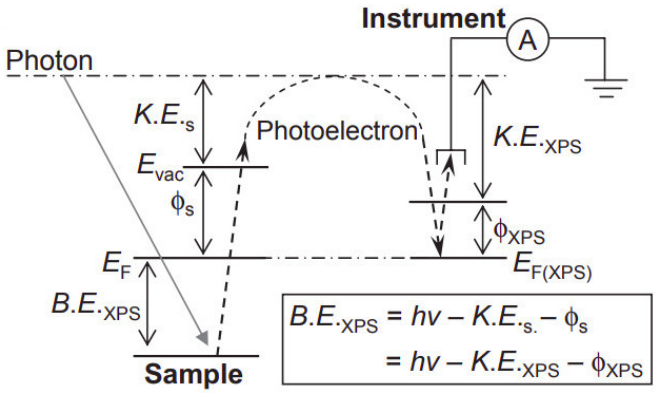

Figure 3.9: Relation between ϕ, E_f and $K.E$ from the sample (subscript s) and instrument. Adapted from van der Klink & Brom (2000).

energy that create distinct features in a typical XPS spectrum, which can be aggregated in two categories: initial state effects and final state effects (schematized in Fig. 3.10). Initial state effects describe the effects induced by the bonding that occurs with other atoms/ions prior to the photoelectron emission process, whereas final state effects are related to the perturbation of the electronic structure resulting from photoelectron emission.

Regarding the initial state effects, the Coloumbic interactions describe the charge density influence on the B.E. values. Prior photoemission, the electronic interactions from the atoms with the chemical environment (interatomic), and within the atoms/ions (intra-atomic) influence on the binding energy, which enables probing of the chemical components and oxidation states (Bagus et al., 2013). The spin orbit splitting, which comes from the interaction of the spin magnetic moment with the orbital magnetic moment of the electrons, gives different binding energies for electrons at the same electronic level, depending on the spin and angular momentum orientations.

The core hole formation from photoionization instantly creates a charge polarization which affects the kinetic energy of the emitted photoelectron. It is supposed to have a kinetic energy that includes all relaxation effects of the ionized atom (except Fluorescence and Auger effects). This is the so called adiabatic approximation but it is not always true. In the opposite regime, the emitted photoelectron respects the sudden approximation, where it leaves the atom before relaxation and its kinetic energy decreases due to a transfer to the ionized atom or material, then increasing the measured binding energy. Note that the real binding energy is the same. The energy transfer from the emitted photoelectron to the ionized atom or material may occur by shake-up, shake-off, plasmon losses and multiplet splitting effects. The plasmon losses comes due to an energy transfer from the emitted photoelectron to the collective excitations (plasmons) existing in the material.

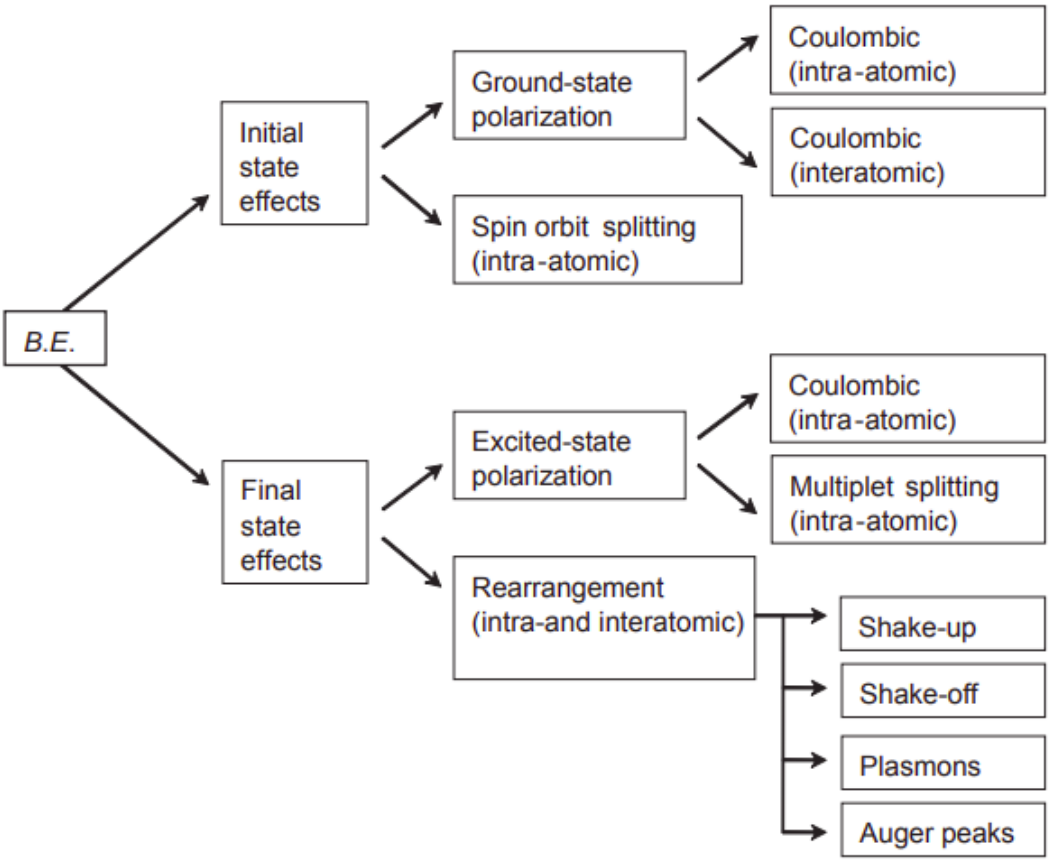

Figure 3.10: Diagramatic view of all the effects that can be experienced by photoelectron emissions from a bound atom/ion with respect to the B.E. value of an unperturbed free atom.

The shake-up and shake-off effects occur due to the energy transfer from the emitted photoelectron to a valence band electron of the ionized atom. If the energy transfer is enough to unbound the valence electron, the effect is called shake-off while the energy transfer without ionizing the atom is called shake-up. Shake-up features can be useful in providing information on the chemical components existing, especially for metal oxides, since they are directly affected by the valence band structure. Fig. 3.11 shows how the shake-up features (identified as satellites) of Cu and its oxides are easily distinguishable. Multiplet splitting effects may occurs whether the atom presents unpaired electrons. After photoemission, the unpaired electron may interact with the unpaired electron at the core level in a similar way than the spin orbit splitting effect. However, the main difference is that the spin orbit splitting effect is an initial state effect and the multiplet splitting is a final state one.

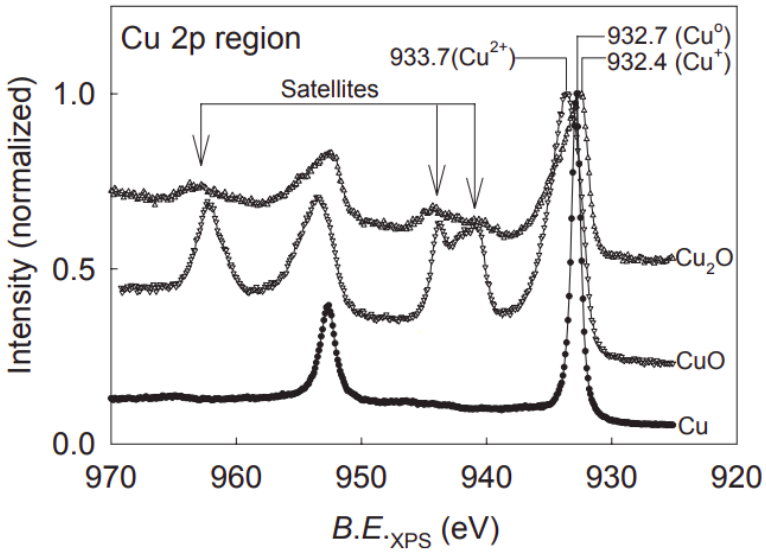

Figure 3.11: XPS spectrum of the Cu $2p$ region for Cu, Cu_2O and CuO. Adapted from van der Klink & Brom (2000).

3.3 X-Ray Absorption Spectroscopy

X-ray Absorption Spectroscopy (XAS) is a technique for studying, at the atomic and molecular scale, the local structure around selected elements. It is a very versatile tool because it does not require long range translational order (Bunker, 2010). XAS technique is also used *in situ*, which makes it a very useful technique for the study of reactive systems under high temperature and pressure of gas, such as catalysts (Fernández-García, 2002).

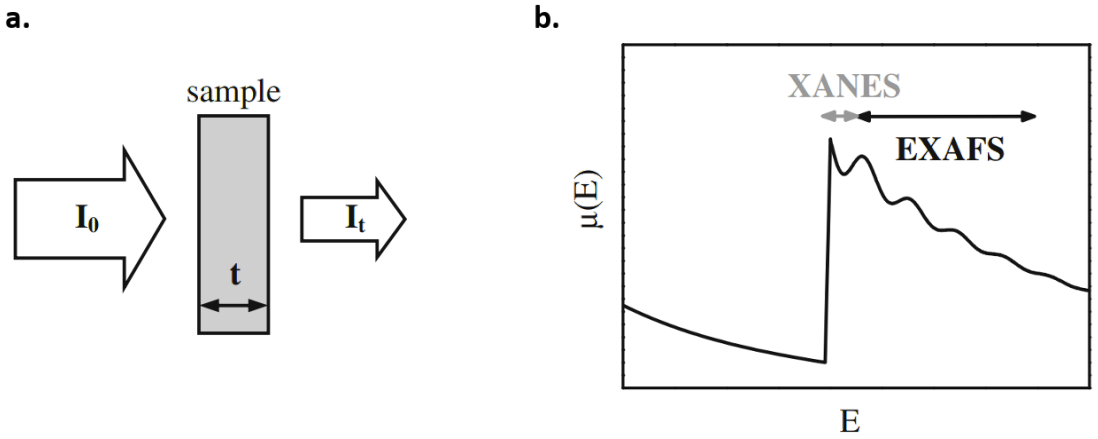

Figure 3.12: (**a**) Schematic representation of incident and transmitted X-ray beam. (**b**) Absorption coefficient $\mu(E)$ versus photon energy around an absorption edge. The XANES and EXAFS regions are demarcated. Adapted from (Schnohr & Ridgway, 2015).

The XAS technique is based on measuring the absorption coefficient of X-rays by the sample as a function of the X-ray energy. Then the measurement consists on the incidence of a monochromatic X-ray beam in the sample with the detection of the transmitted intensity. The intensity I attenuation for a sample of thickness t is described by the Beer-Lambert's law:

$$I = I_0 e^{-\mu(E)t} \tag{3.11}$$

where I_0 is the intensity of the incident X-ray and $\mu(E)$ is the absorption coefficient. Fig. 3.12.a shows a schematic representation of the XAS measurement setup in transmission mode. Generally, $\mu(E)$ decreases smoothly with energy. However, there are sharp rises in $\mu(E)$ for well defined energies related to specific atoms in the material. These are called absorption edges and they arise when the X-ray energy is sufficient to emit photoelectrons from bound states in the atoms. For energies just above the absorption edge, $\mu(E)$ presents an oscillatory pattern, which is called X-ray Absorption Fine Structure (XAFS), and it is categorically divided into the X-ray Absorption Near Edge Structure (XANES) and the Extended X-Ray Absorption Fine Structure (EXAFS) (Fig. 3.12.b). Although absorption edges were first measured in 1913 by Maurice De Broglie, it was much later that Stern et al. (1974, 1975), Sayers et al. (1971), and Lytle et al. (1975) synthesized the essential aspects of a viable theory of XAFS, making it a practical tool.

XAS is described by quantum mechanics since it arises from the absorption of photons, which gives an electronic transition between quantum states. The absorption coefficient $\mu(E)$ has to be proportional to the probability of an electronic transition induced by an electromagnetic wave with energy E. In the atomic context, electromagnetic waves can be treated as a weak time-dependent perturbation. Time-dependent perturbation theory describes that the transition rate, to first order in the perturbation, is proportional to the squared modulus of the transition amplitude (matrix element). This is known as the Fermi's Golden Rule. Hence, using the interaction Hamiltonian between an electromagnetic field with the electrons in the dipole approximation:

$$\mu(E) \propto \sum_f |\langle f|\hat{\epsilon}\cdot\vec{r}|i\rangle|^2 \delta(E_i - E_f - E) \tag{3.12}$$

where $|i\rangle$ and $|f\rangle$ are, respectively, the initial and final electronic states. The quantities $\hat{r}$, $\hat{\epsilon}$ and E are the electron position and the X-ray's electric polarization vector and energy. Eq. (3.12) describes the probability of transition from the electronic state $|i\rangle$ to any of the vacant electronic state $|f\rangle$ for a single electron in an isolated atom.

The EXAFS oscillations arise from the interference between the waves associated to the photoelectron emitted and photoelectron backscattered by the neighboring atoms. Depending on the existence of constructive or destructive interference the absorption coefficient increases or decreases, respectively, then explaining the oscillatory behaviour after absorption edge. It is schematically shown in Fig. 3.13. The mathematical description can be done by a high order multiple scattering formalism (Lee & Pendry, 1975), and results in the factoring of $\mu(E)$ in terms of the absorption by an isolated atom $\mu_0(E)$ modulated by an oscillatory function $\chi(E)$:

$$\mu(E) = \mu_0(E)\,(1 + \chi(E)) \tag{3.13}$$

The $\chi(E)$ function is the EXAFS oscillations, which is analyzed to obtain structural information. In order to separate the structural information from the energy dependence of the absorption coefficient, Eq. (3.13) is rewritten as:

$$\chi(E) = \frac{\mu(E) - \mu_0(E)}{\mu_0(E)} \approx \frac{\mu(E) - \mu_0(E)}{\Delta\mu_0} \tag{3.14}$$

where the energy-dependent denominator is approximated by a constant typically chosen as the height of the absorption edge. Instead of using $\chi(E)$, the EXAFS oscillations are usually written as a function of the photoelectron wave number $k = \sqrt{2m_e(E - E_0)/\hbar^2}$, where m_e stands for the electron mass. The position representation of the states in Eq. 3.12 can be expressed in terms of an outgoing wave emitted at the absorbing atom plus incoming waves that are scattered back by neighboring atoms and used to calculate the dipole transition matrix element from which $\chi(k)$ is calculated (Sayers et al., 1971). Then the EXAFS oscillations can be expressed as

$$\chi(k) = \sum_j S_0^2 N_j \frac{F_j(k) e^{-2R_j/\lambda(k)}}{kR_j^2} e^{i2kR_j + i\delta_j(k)} e^{-2\sigma_j^2 k^2} \tag{3.15}$$

where the j index represents the atomic shell at a given distance from the central atom. Here the structural parameters are the interatomic distance R_j (half the total length of the scattering path), the coordination number N_j (number of equivalent single scattering paths) and the Debye-Waller factor σ_j^2 (temperature dependent fluctuation in bond length, which includes also the effects due to structural disorder). In addition, $F_j(k)$ represents the effective scattering amplitude, $\delta_j(k)$ is the effective total phase shift (including contributions from the central atom and all scattering atoms), $\lambda^{-1}(k)$ is the sum of the inverses of the inelastic mean free path and the length associated to the finite lifetime of the hole created at the core level, and S_0^2 is the amplitude reduction factor.

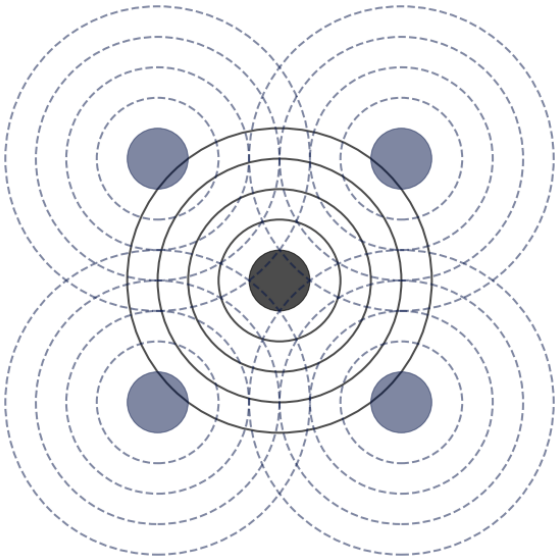

Figure 3.13: Pictorial view of the interference between the waves associated to the emitted photoelectron (black solid circles) and backscattered by the neighboring atoms (gray dashed circles).

For data analysis, firstly the EXAFS oscillations should be extracted from the XAS spectrum. After this, the EXAFS oscillations are Fourier transformed in order to facilitate the interpretation of the results. The next step is the fitting of the EXAFS oscillations and Fourier Transform. For this purpose, *ab initio* calculations of the scattering phase shifts and amplitudes have become the standard procedure. The FEFF program (Zabinsky et al., 1995) is commonly used to implement this calculation. It starts with a model structure that specifies the absorbing atom and the positions and types of the surrounding atoms to be considered. Then, it determines the scattering paths from the geometrical distribution of the atoms, creates spherically symmetric muffin-tin potentials, overlaps the atomic wavefunctions, and calculates the effective scattering phase shifts based on the potentials. FEFF implements a path filter that efficiently (and approximately) estimates the importance of each scattering path. Once the paths are enumerated, the effective scattering amplitudes for each path are calculated using the algorithm of Rehr & Albers (1990), and the EXAFS oscillations are generated by summing the paths. With the effective scattering amplitude and phase shift of one or more paths, a least-squares minimization method is used to fit Eq. 3.15 (and its Fourier Transform) to the EXAFS oscillations, where the path parameters R_i, N_j, S_0^2, σ_j^2 (and also an adjustment in energy E_0) are used as variables. EXAFS is complementary to XRD, since the latter establishes all periodic structural features of solids with long range order, while EXAFS can elucidate local atomic order structure even for very low concentrations (Grünert & Klementiev, 2020).

The XANES region is often comprised of intense absorption peaks that come due to the photoelectron scattering in the near vicinity of the absorbing atom (Bunker, 2010). They are sensitive to chemical bonding and the oxidation state of the absorbing atom. XANES region analysis is usually carried out by linear combination of standards which are suspected to be in the sample. Linear Combination Fitting (LCF) is severely limited if a large number of possible standards has to be considered and if the spectra of different standards are very similar to each other. Characteristic features such as the intensity after the absorption edge can be quantified by peak fitting procedures. To that end, the absorption edge itself is typically approximated by an arctangent function while the peaks are modeled by a pseud-Voigt function to account for experimental broadening (Bunker, 2010).

3.4 Transmission Electron Microscopy

Transmission Electron Microscopy (TEM) is the most used technique to acquire images of objects with submicrometer dimensions. The electron microscope arose due to the limited resolution in optical microscopes, which is imposed by the wavelenght of visbile light (380-700 nm). Soon after Louis de Broglie theorized the wave-like characteristics of electron (De Broglie, 1925), Knoll and Ruska developed the idea of an electron microscope, which awarded Ruska with the (”somewhat late” as himself said) 1986 Nobel prize (Ruska, 1987). Relativistic electrons have an approximate de Broglie wavelength given by

$$\lambda_e \approx \frac{h}{\sqrt{2m_0E\left(1+\frac{E}{2m_oc^2}\right)}} \tag{3.16}$$

where E is the electron energy and m_0 its rest mass, while h and c are the Planck and speed of light constants. In a typical electron microscope electrons have energy in the range 100-300 keV. From Eq. (3.16), these energies result in wavelenghts smaller than the typical interatomic distance in crystals, which is on the order of a few Å. Therefore these electrons are able of probing materials with atomic resolution. The instrumental limitations of a TEM equipment operating in typical settings decrements this resolution, making it closer to the order of the nanometers. However, there are high resolution techniques that are able to resolve individual atoms and show discernible crystalline planes.

The TEM technique consists on focusing an electron beam into a sample and detecting

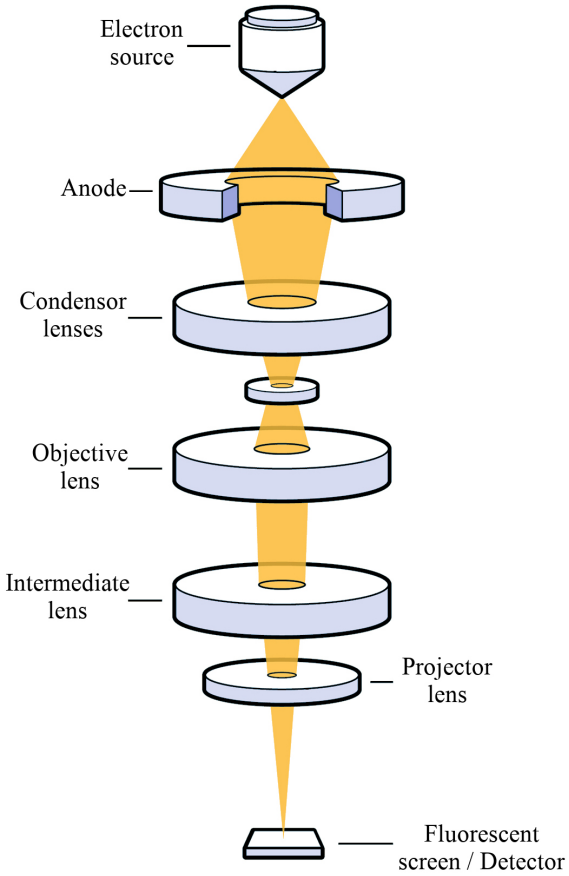

Figure 3.14: Schematic representation of a TEM instrument. The sample is positioned between the condensor and objective lenses.

the transmitted electrons. The microscope is made by an electron gun, a set of lenses and a detection system, as schematized in Fig. 3.14. The electron gun is made of an electron source and an anode to accelerate the electrons. The electron beam that leaves the electron gun enters in a system of condenser lenses where it is collimated to a coherent beam and directed to the sample. Then, the transmitted electrons enter the imaging set of lenses, which consist of an objective, an intermediate and a projector lens, and finally reach a fluorescent screen or detection system.

TEM images are a bidimensional projection of the region in the sample on which the electron beam is focused. The incoming electrons undergo scattering, and thus the electron wave can change both its amplitude and phase as it traverses the specimen. By positioning an objective aperture at a specific location in the back focal plane, an image is made with only those electrons that have been transmitted in a specific angle in relation to the direction beam. This defines two imaging modes, as shown in Fig. 3.16. When the aperture is positioned to pass only the transmitted electrons in a small angle in

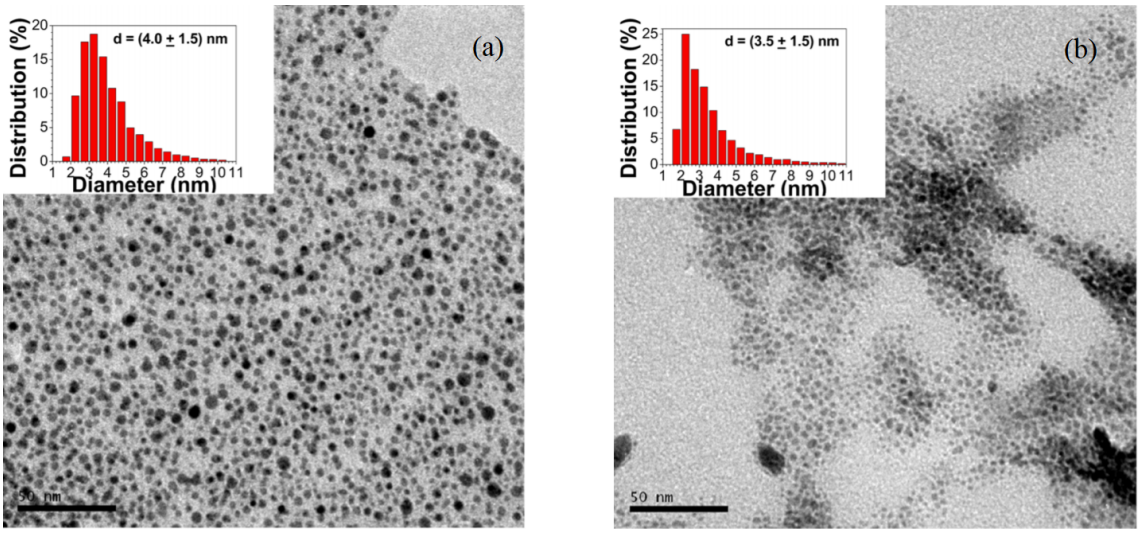

Figure 3.15: Transmission electron microscopy images of (**a**) Cu and (**b**) Ni nanoparticles. The inset represents the size distribution of the nanoparticles. Adapted from Matte et al. (2015).

relation to the direction beam, a bright-field image is formed, whereas when the aperture is positioned in high angles, a dark-field image is formed (Fultz & Howe, 2012). Fig. 3.15 shows bright field TEM images of Cu and Ni nanoparticles (Matte et al., 2015).

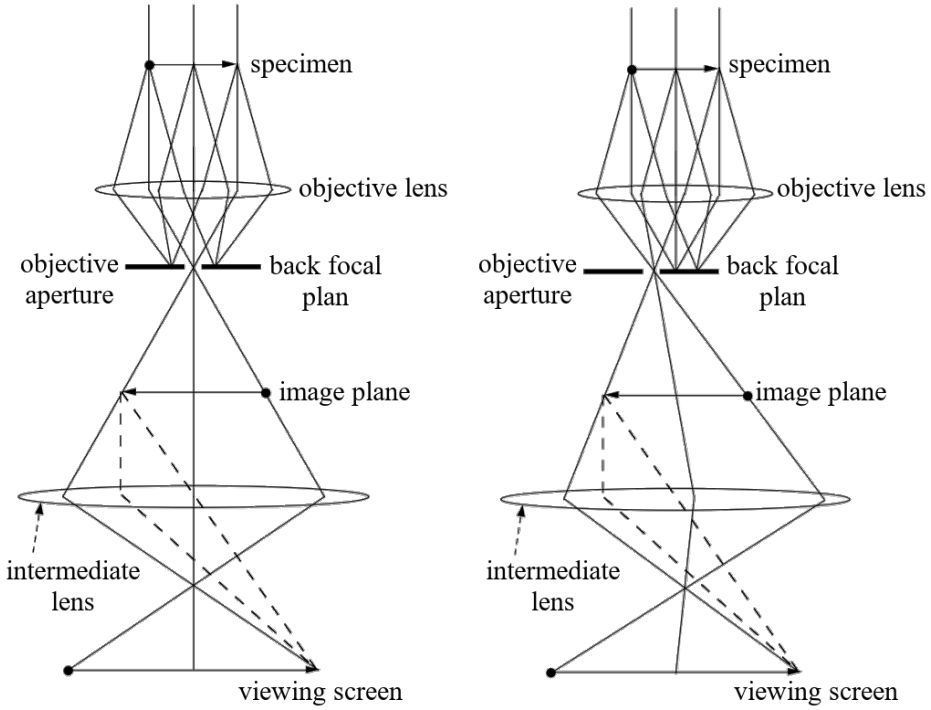

Figure 3.16: On the left, the schematics for a bright field mode. On the right, a dark field mode. Image from Fultz & Howe (2012).

3.5 Monte Carlo Simulations of Cluster Diffusion

The Monte Carlo methods are a broad class of computational algorithms which rely on random sampling to obtain statistical results. Monte Carlo simulations sample from a probability distribution for each variable to produce possible outcomes. It can be used to study thermodynamic quantities or statistical properties of a large variety of systems. Some examples range from the computation of the specific heat of materials to spatial correlations in a system (Newman & Barkema, 1999). Supported small clusters, such as nanoparticles, present thermally activated Brownian motion due to weak nanoparticle interfacial adhesion (Jose-Yacaman et al., 2005). A simple way to study Brownian Motion of clusters is by a Monte Carlo simulation which use random numbers to perform random walks.

3.5.1 Random Walks

A random walk is a path that consists of a succession of random steps. Lets consider a random walker, who initially starts at the origin in d dimensions. At each step, the walker has equal probability $1/(2d)$ to move in any direction within any of the d axis with a step size Δ. Let $\vec{R}_N$ be the position of the walker after N independent steps and τ the time interval between the steps. Then time is defined as $t = N\tau$. It can be shown that in the limit where $\Delta \to 0$, $\tau \to 0$ and $N \to \infty$ the probability density to find the walker in a position interval ($\vec{r}$, $\vec{r} + d\vec{r}$) at time t is:

$$\rho(\vec{r}, t) = \frac{1}{(4\pi D t)^{d/2}} \exp\left[-\frac{r^2}{4Dt}\right] \tag{3.17}$$

where

$$D = \frac{\Delta^2}{2d\tau} \tag{3.18}$$

D the diffusion coefficient (Reichl, 1999). Eq. 3.18 is also known as the Einstein-Smoluchowski relation. The diffusion coefficient is a measurable quantity that gives information on the average behaviour of clusters.

When modeling a dynamic physical problem, random walks with variable jump length can be more adequate. A numerical implementation of random walks with variable jump length requires a sampling method for non-uniform distributions. The inverse transform method (Devroye, 2006) generates sample numbers at random from a probability distribution given its cumulative distribution function. Let X be a random variable whose

distribution f_X can be described by the cumulative distribution function F_X. By generating a random number u from the standard uniform distribution in the interval [0,1], X can be computed by taking $F_X^{-1}(u)$. The only requirement is that the cumulative distribution F_X be invertible. Furthermore, if the distribution has finite first and seconds moments, the central limit theorem states that the probability distribution of a large number of measurements of X is a Gaussian centered at the mean, regardless of the form of f_X (Reichl, 1999).

3.5.2 Anomalous Diffusion

Eq. 3.17 is a Gaussian function centered at $\langle r \rangle$ (zero in this case) with standard deviation $\sigma = \sqrt{\Delta^2 N} = \sqrt{2Dt}$. Hence, in free diffusion the mean-square displacement of the diffusing cluster grows linearly with t,

$$\langle r^2 \rangle = 2d\ Dt \tag{3.19}$$

However, for diffusion in inhomogeneous medium, such as clusters within crowded systems, diffusion is described by a power law (Havlin & Ben-Avraham, 1987)

$$\langle r^2 \rangle \propto t^{\alpha} \tag{3.20}$$

and a normalised, time dependent diffusion coefficient can be defined (Saxton, 2001)

$$D(t) = \Gamma\ t^{\alpha - 1} \tag{3.21}$$

where Γ is a constant. When $\alpha > 1$, super-diffusion is described, while $\alpha < 1$ describes sub-diffusion. For $\alpha = 1$, $\langle r \rangle \propto t$, D is constant and diffusion is normal.

Chapter 4

Methodology and Analysis

This chapter presents the experimental and numerical procedures and a detailed analysis of the results obtained.

4.1 Proposed Method for Sintering Prevention

In this work, a new strategy to avoid sintering of nanoparticles in catalysis is proposed and applied to Cu nanoparticles supported on MgO. Due to the massive usage of catalysts in chemical processes, it is always desirable to have a balance between cost and efficiency in catalyst design. Cu nanoparticles are widely used because of copper's high natural abundance, low cost and the practical and straightforward multiple ways of preparing Cu-based nanomaterials (Gawande et al., 2016). The choice of support largely depends on its compatibility with different reagents, and, most importantly, the properties it confers on the resulting supported nanomaterials. The basicity of MgO is counted as a benefit when compared with neutral or acidic supports (Julkapli & Bagheri, 2016), besides the low cost. Cu/MgO nanoparticles have been observed to benefit various reactions, such as the synthesis of methanol (Yang et al., 2005), the alcohol dehydrogenation (Marella et al., 2012, Nagaraja et al., 2007), or the water gas shift (WGS) reaction (Rodriguez et al., 2009) which is one of the main processes for hydrogen production on an industrial scale. Therefore, Cu/MgO represents a very interesting catalytic system to be studied.

The proposed strategy to avoid sintering consists on impregnating the surface of the MgO support with dithiol molecules, which are expected to constrain the Cu nanoparticles diffusion on the support surface, subsequently reducing the coalescence rate (Fig. 4.1). Thiol complexes are known to interact with metals, poisoning the catalyst and resulting in harmful effects on the catalytic activity. However, thiol adsorption to several metal oxides have also been observed (Soares et al., 2011, Volmer et al., 1990, Wallace, 1966),

although there is a lack of recent studies for adsorption of thiol complexes specifically on MgO. Whether the dithiol molecules are adsorbed on the support, they can affect the nanoparticles diffusion by acting as obstacles to their otherwise free path. The specific nature of the interaction that makes a dithiol molecule obstructing the migration path of a nanoparticle is based on changing the local chemical environment of the support surface, which decreases nanoparticle diffusion by raising the activation energy for migration. It is similar to what was observed by Yang & Sacher (2001), where Ar^+ sputtering of both HOPG (Highly Ordered Pyrolytic Graphite) and Cyclotene supports has been shown to reduce the coalescence of Cu clusters. Here, the only hypothesis is that, when a nanoparticle reaches the vicinity of a dithiol molecule adsorbed at the surface, it will not be able to migrate across this region, or at least its crossing will be strongly impaired. The efficiency of this mechanism to decrease coalescence is tested by a numerical simulation of random walkers in a surface with obstacles and the results are shown at the end of this chapter.

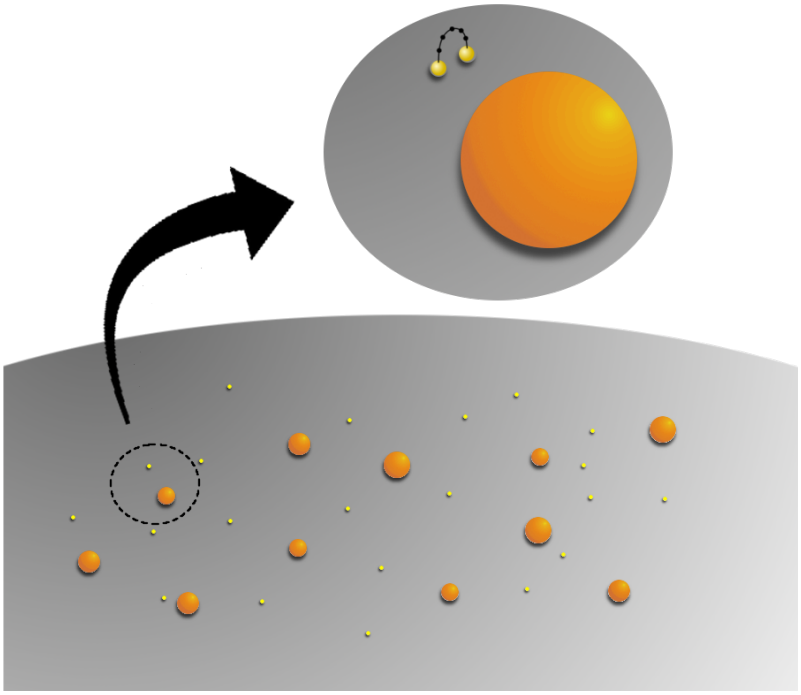

Figure 4.1: Cu nanoparticles, represented by the orange spheres, supported on MgO, represented by the gray surface. The support is impregnated with dithiol molecules, represented by the yellow spheres. The zoom region shows a Cu nanoparticle and a dithiol molecule.

4.2 Experimental and Numerical Procedures

4.2.1 Sample Preparation

The Cu nanoparticles were synthesized in a previous work of the group (Matte et al., 2015). A standard commercial MgO powder and three types of dithiol molecules (1,3-propanedithiol, 1,4-butanedithiol, 1,5-propanedithiol) were used. The proposal method is based on an easy sample preparation. Firstly, the dithiol is impregnated by dripping it on MgO (without Cu) at room temperature with 9 mol % . After, the Cu nanoparticles were supported by manual mixing with 12 wt %. in relation to the MgO support, impregnated with dithiol or not. Fig. 4.1 shows the dithiol molecules structural representation. Four samples were prepared to be analysed: a control sample of Cu nanoparticles supported on MgO (CT) and three samples of Cu nanoparticles supported on MgO impregnated with dithiol (DT_n, with $n = 3, 4, 5$, depending on the number of carbons in the dithiol molecule).

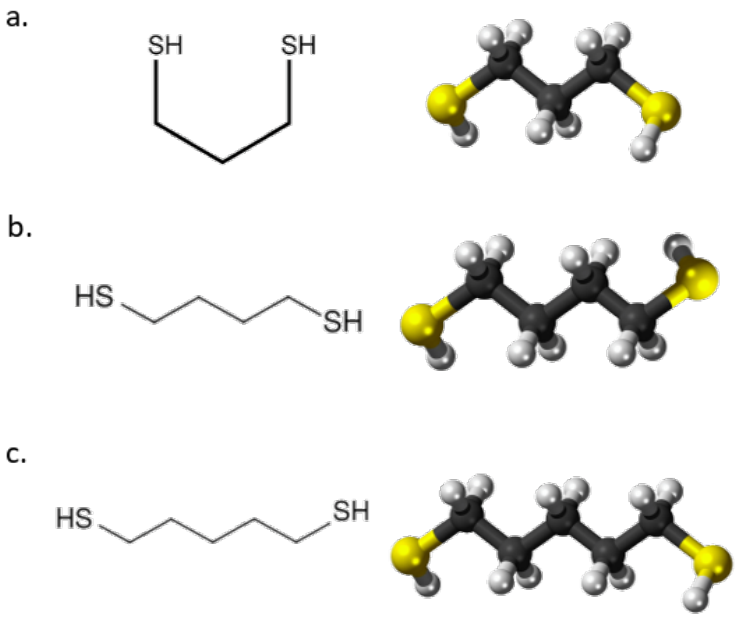

Figure 4.2: Structural representation of (**a**) 1,3-propaneditiol, (**b**) 1,4-butaneditiol e (**c**) 1,5-pentaneditiol molecules.

4.2.2 XRD

The XRD data were acquired in a Siemens 500D conventional diffractometer operating at 40 kV and 17 mA with $Cu\ K_\alpha$ characteristic radiation ($\lambda = 1.5405$ Å). The

measurements were carried out in a Bragg-Brentano geometry, with range of 20-90 °C, $0.05°$ step size and 0.4 s by point. The powder was sieved to a 48 μm grain size before the measurements. The XRD patterns were indexed using the *Crystallographica Search-Match* software and the International Centre for Diffraction Data (ICDD) database. The *FullProf* software was used to conduct the Rietveld Refinement (Rodriguez-Carvajal, 1990).

The background was modeled using a linear interpolation with adjustable parameters. As a peak profile, the Thompson-Cox-Hastings pseudo-Voigt convoluted with an axial divergence asymmetry function was used. Some parameters were fixed in the refinement: the atomic positions in the primitive cell, occupation number and the angle between the primitive vectors for each phase. Material anisotropy and preferential orientation were not included. As criteria for the fit quality, the goodness parameter χ^2 was adopted. It is defined as $\chi^2 = (R_{wp}/R_{exp})^2$, where R_{wp} is the weighted profile R factor and R_{exp} is the expected R factor, which represents the best possible R_{wp}. The R factor is the residue factor, which constitutes a measurement of agreement between the calculated and measured quantities. Therefore, it is a strict condition that $\chi^2 \geq 1$, and the closer to 1, the better the fit quality. However, the χ^2 factor alone can not assure that the initial crystalline model is correct and that the refined parameters are physically reasonable, so the refined parameters are always constrained to a range.

4.2.3 TEM

The TEM images were acquired at the Centro de Microscopia e Microanálise (CMM - UFRGS), using a JEOL JEM 1200Exll microscope with 80 kV operation voltage. The nanoparticles powder was diluted in ethanol and dispersed in ultrasound during 30 minutes. A drop of this solution was placed over a grid coated by a thin carbon film. Several bright field images were obtained and later analysed using Image J software (Abràmoff et al., 2004). For each discernible cluster in an image, the mean Feret diameter was measured. The Feret diameter is the distance between the two parallel planes restricting the object perpendicular to that direction, and the mean Feret diameter is the average between the maximum and minimum Feret diameters. To generate size distributions, around 2000 mean Feret diameters were used.

4.2.4 *In situ* XAS

In situ XAS measurements were performed at the Brazilian Synchrotron Light Laboratory (LNLS) aiming the investigation of the local atomic order around Cu atoms and

the time evolution of the oxidation state of Cu atoms of the Cu/MgO nanoparticles during an activation treatment. 55 mg of the nanoparticles powder was compacted to make a homogeneous 5 mm diameter pellet before introduction into the tubular furnace existing at the beamline. The gaseous atmosphere is introduced into the tubular furnace and goes through the pellet, exiting at the opposite side to the exhaust system. The pellets are heated by a resistive heating system. The temperature at the sample holder is measured by a Chromel-Alumel thermocouple positioned at around 2 mm from the sample position. A power supply controls the sample temperature during the experiments with an accuracy of ± 1 °C. The furnace has two external Kapton foil windows allowing the in situ XAS measurements. This is valid for both *in situ* time-resolved XANES and *in situ* EXAFS measurements, which have some specificities described in the next sections.

(a) *In situ* time-resolved XANES

In situ time-resolved XANES measurements were carried out at the DXAS beamline (Cezar et al., 2010) at LNLS. The measurements were performed at the Cu K edge (8979 eV) in transmission mode. At the beginning, the Cu/MgO nanoparticles were exposed to 100 mL/min 5% H_2 + 95% He atmosphere. Then the samples were heated subsequently to selected temperatures of 100 °C, 200 °C, 300 °C, 400 °C, and 500 °C with 10 °C/min heating rate. For each temperature, the sample was kept under H_2 atmosphere during 60 minutes. At the end, the H_2 atmosphere was removed, the sample was exposed to 200 mL/min N_2 atmosphere and cooled to room temperature. The measurements made use of a curved Si(111) crystal (dispersive polychromator), which focuses the beam in the horizontal plane down to about 200 μm, a mirror that focuses it on the vertical plane to about 500 μm, and a position-sensitive CCD detector. The tubular furnace was placed in the beamline, taking care to place the pellet at the X-ray focal point. The time resolution of the measurements was around 100 ms.

The raw data were analyzed in accordance to the standard procedure of data reduction (Koningsberger & Prins, 1988) with the *Demeter* software (Ravel & Newville, 2005). To normalize the data, the pre-edge and post-edge regions are regressed by a linear and a cubic polynomial, respectively. Then, a normalization constant is evaluated by extrapolating the pre-edge and post-edge regressed curves to the edge energy point and subtracting the pre-edge line from the post-edge line at that point. Finally, the pre-edge line is extrapolated to the full measurement and subtracted from $\mu(E)$, which is then divided by the normalization constant. XANES analysis was done by LCF of the spectra, which is implemented in Athena interface of Demeter. In the LCF method, the normalized XANES spectra are modeled by summing weighted known standard spectra $\mu_i(E)$:

$$\mu_{calc}(E) = \sum_i w_i \mu_i(E) \ , \tag{4.1}$$

where the weights w_i are constrained to $\sum_i w_i = 1$. The best weight is found using the least square fitting of $\mu_{calc}(E)$ to the experimental $\mu(E)$. The LCF has been carried out in the normalized $\mu(E)$ spectra, from -20 eV to 30 eV in relation to the edge energy. The relative weights by the LCF allowed to obtain the chemical compounds present in the Cu nanoparticles during the reaction.

(b) *In situ* EXAFS

In situ EXAFS measurements were carried out at the XAFS2 beamline (Figueroa et al., 2016) at LNLS. The measurements were conducted at Cu K edge (8979 eV) in transmission mode. The Cu/MgO nanoparticles were exposed to 100 mL/min 5% H_2 + 95% He atmosphere and heated to 300 °C with 10 °C/min heating rate. The nanoparticles remained at 300 °C with the H_2 atmosphere during 50 min. At the end, the H_2 atmosphere was removed, the sample was exposed to 200 mL/min N_2 atmosphere and cooled to room temperature. The spectra were collected before and during reduction treatment at 300 °C using a Si(111) crystal and three ionization chambers. The samples were measured at room temperature and also at 300 °C with the sample exposed to the reduction atmosphere. In this last case, measurement at 300 °C, the spectra were acquired after 50 min of sample exposure to the H_2 atmosphere at 300 °C in order to ensure the achievement of a steady state of the sample. Standard Cu foil was used to calibrate the Si(111) monochromator. Two to four scans were collected in order to improve the signal-to-noise ratio.

The *in situ* EXAFS spectra were initially calibrated. The edge energy was calibrated by finding the zero crossing of the second derivative around the edge of the standard Cu foil, which was present in front of the third ionization chamber in each measurement. It was selected as the edge energy, and the corresponding energy shift to the Cu K-edge (8979 eV) position was subtracted from the experimental data. In addition, glitches were manually identified and simply removed without any attempt to interpolate data between them. After this, the data were analyzed in accordance to the procedure described for the analysis of the *in situ* time-resolved XANES spectra using Demeter software, and the following procedures were conducted in the Demeter package Artemis (Ravel & Newville, 2005). The single atom contribution was subtracted from the $\mu(E)$ in order to get the EXAFS oscillations $\chi(k)$. A Fourier Transform of $\chi(k)$ was carried out to extract the radial distribution function $\chi(R)$ around the absorbing element. However, since the

EXAFS amplitude is damped with an increase in k value, the data are generally multiplied by a power of k before taking the Fourier Transform. Here, a k^2 weight was chosen. A Kaiser-Bessel window of 9 Å range was used. FEFF6 code was used to obtain the phase shift and amplitudes (Zabinsky et al., 1995) with Cu an CuS crystal structures. The only parameter fixed in the fits was the amplitude reduction factor S_0^2, which was previously obtained from the Cu standard fit. The R-factor obtained from the analysis was always lower than 0.03, demonstrating the good agreement between the proposed model and the experimental data.

4.2.5 XPS

The XPS measurements were performed at the LNNano-CNPEM using a *Thermo Scientific K-Alpha* X-ray photoelectron spectrometer with operating voltage of 12 kV and an Al-Kα radiation source (1486.68 eV). The samples were measured before and after the reduction treatment at 300 °C performed during the *in situ* EXAFS measurements previously described. For the XPS measurements, a thin layer of powder was dispersed on a carbon tape. The base pressure used during the measurements was around 1×10^{-9} mbar. The photoelectrons were collected in the exit angle of 45 ° by a double focusing hemispherical analyzer operating in the CAE mode. To perform low and high resolution measurements, the pass energies used were 200 eV and 50 eV, while the energy steps were 1 eV and 0.1 eV, respectively, with dwell time of 0.5 s. The measurments were conducted in the long scan Cu 2p, S 2p, Mg $1s$, O $1s$ and C $1s$ electronic regions.

The analyzer's energy calibration was performed using a standard Au foil (Au $4f_7/2$ peak at 84.0 eV). Charging effects in the samples were corrected using the C $1s$ position of adventitious carbon at 285 eV. The XPS spectra were analyzed using XPS Peak software (Kwok, 2000). Initially, it is necessary to subtract the background caused by inelastically scattered photoelectrons. The background was modeled as a Shirley-type function (Shirley, 1972), which assumes a constant (energy-independent) probability for energy loss. The Au $4f$ region of an Au standard was analysed in order to determine the pseudo-Voigt profile used to fit the XPS spectra. A pseudo-Voigt profile linearly combines a Lorentzian function, which describes the intrinsic life time broadening of the core level state and the X-ray line shape from the X-ray source, with a Gaussian function, which depicts the response function of the analyzer. From this analysis, it was determined the pseudo-Voigt function as composed of 55% Lorentzian and 45% Gaussian. The FWHM of a given chemical component and the relative binding energy of different components are constrained to be the same in all samples. Furthermore, the doublets, originated from spin orbit coupling, have their distances and area ratios fixed.

4.2.6 Numerical Simulation

A well known property of supported nanoparticles is their thermally activated Brownian Motion. The thermally induced diffusion of nanoparticles across the support followed by coalescence is a well known mechanism of sintering, which leads to catalyst deactivation. This work seeks to hinder the diffusion of nanoparticles over the support by creating obstacles at the support's surface. To investigate the effectiveness of this approach in reducing coalescence, a Monte Carlo simulation is carried out. The nanoparticles are modeled as spherical random walkers moving across a square surface of side L with periodic boundary conditions. The 3D character of the particles is taken in account only for mass calculation. For spatial movement and coalescence, only the circular projection of the particles in the surface is considered. The dithiol molecules are treated as solid spheres, acting as fixed obstacles.

The movement is simulated by randomly choosing a particle and attempting to move it from $\vec{r}$ to $\vec{r} + \vec{s}$, where $\vec{r} = (x, y)$ is the particle previous position and $\vec{s} = (s_x, s_y)$ is the jump length vector. As Eq. 2.5 shows, the diffusion coefficient of particles diminishes with increase in size. In random walk models for the diffusion of atoms adsorbed on solid surfaces, an exponentially decaying function of distance has previously been used as the jump length distribution (Tsong, 1988, Lakatos-Lindenberg & Shuler, 1971). Here the jump length exponential distribution is extended to particle diffusion. Hence, the values of s_x and s_y are independently sampled from

$$\rho_i(s) = \frac{1}{\lambda_i} e^{-s/\lambda_i} \tag{4.2}$$

where λ is a parameter that will relate to the particle size and the system temperature. The sign of $\vec{s}$ is randomly selected. The first and second moments of the jump size distribution are

$$\langle s \rangle = \int_0^\infty ds\ s\rho_i(s) = \lambda_i\ ;\ s \geq 0 \tag{4.3}$$

$$\langle s^2 \rangle = \int_0^\infty ds\ s^2\rho_i(s) = 2\lambda_i^2 \tag{4.4}$$

hence the ensemble average jump size for the i^{th} particle is λ_i. The following relation between the parameter λ_i and the radius is proposed to model nanoparticle diffusivity:

$$\lambda_i = \frac{K}{R_i}\ , \tag{4.5}$$

where K is a constant with appropriate units, and R_i is the radius of the i^{th} particle. With this relation, varying the radius changes the particle jump size probability. This work is focused only on investigating a possible mechanism in which obstacles can prevent nanoparticles coalescence, with no ambition of describing a detailed model of nanoparticles diffusion and coalescence. Therefore, the influence of other factors such as temperature, inhomogeneity of the surface and drag are disregarded. The influence of the number of particles to obstacles ratio and particles occupation fraction in particle growth are the main interest and are thoroughly explored.

With a selected particle and jump vector $\vec{s}$ generated, a merging zone is defined, which is the area on the surface that would be occupied by a particle while moving from $\vec{r}$ to $\vec{r}+\vec{s}$ (see Fig. 4.3). Then it is checked if any other particle/obstacle projected area overlaps with the merging zone. In the case of another particle in the merging zone, both particles merge into a new one conserving mass. The new particle is positioned at the center of mass of the two and a new λ_i parameter is calculated with Eq. 4.5. The radius of the combined particles is given by

$$R_i = \left(\sum_j {R_j}^3 \right)^{1/3} . \tag{4.6}$$

where the new particle assumes the lower index of the merging particles. The merging is always carried out with only two particles at a time. If a particle happens to overlap with two or more other particles simultaneously, then it merges with the closest one from its departure position first, then with the second closest and so on. The combined particle position is given by

$$\vec{r_i} = \frac{\sum_j m_j \vec{r_j}}{\sum_j m_j} . \tag{4.7}$$

Obstacles do not coalesce with other obstacles nor particles. Therefore, if an obstacle is on the merging zone, the jump is simply cancelled, simulating a blockage.

Each Monte Carlo (MC) step consists of N attempts to move a random particle, where N is the number of particles. In the first 10^3 MC steps coalescence is turned off so that the particles and obstacles are randomly distributed on the surface. Then the spatial configuration at the end of this steps is set as the initial positions.

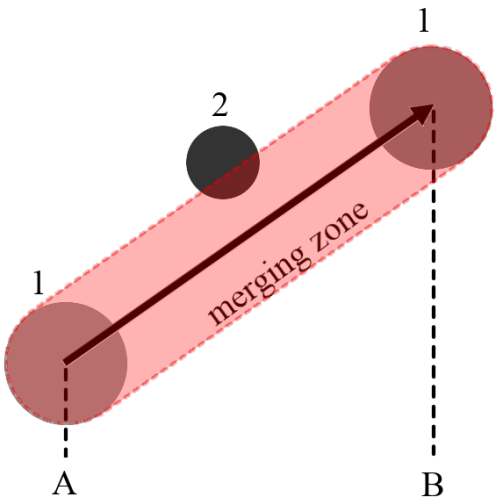

Figure 4.3: If particle 1 moves from A to B, then all area occupied by its trajectory is defined as a merging zone (represented by the red area with dashed boundaries). If any other particle's area overlaps with the merging zone, as particle 2 in the figure, then the two particles merge into a new one, conserving mass. If more than one particle are in the merging zone, the one closest from position A is chosen.

4.3 Crystal Structure Solving

Fig. 4.4 shows the diffractograms of the unsupported Cu nanoparticles and the MgO support, both before the reducing treatment. Only copper (II) oxide (CuO) and copper(I) oxide (Cu_2O) crystal structures were identified in the Cu nanoparticles, showing no significant quantity of Cu^0 before the reducing treatment. It is expected for Cu nanoparticles due to the long exposure to ambient atmosphere (Matte et al., 2015). In the support diffractogram, magnesium oxide (MgO), magnesium hydroxide ($Mg(OH)_2$) and hydromagnesite ($Mg_5(CO_3)_4(OH)_2(H_2O)_4$) crystal structures are identified, the two latter probably due to aging.

In Fig. 4.5 the diffractograms of the DT_3, DT_4, DT_5 and CT samples before and after reducing treatment at 300°C are shown. Before the reducing treatment all samples present the same crystal structures identified in the non-supported Cu nanoparticles and support samples. After the reducing treatment, CuO and Cu_2O phases are still identified, in addition to new ones of MgO and Cu(0). Meanwhile, $Mg(OH)_2$ and hydromagnesite phases are no longer detected. It shows the reduction treatment was effective for activating the catalyst and the CuO and Cu_2O components come from air exposition again. The Cu presence is evidenced by an intense Bragg reflection of the (111) crystal plane, around 44 °. CuO, Cu_2O and MgO phases have very similar Bragg reflection angles, thus it can not be assured whether all contribute simultaneously to the diffraction patterns after the

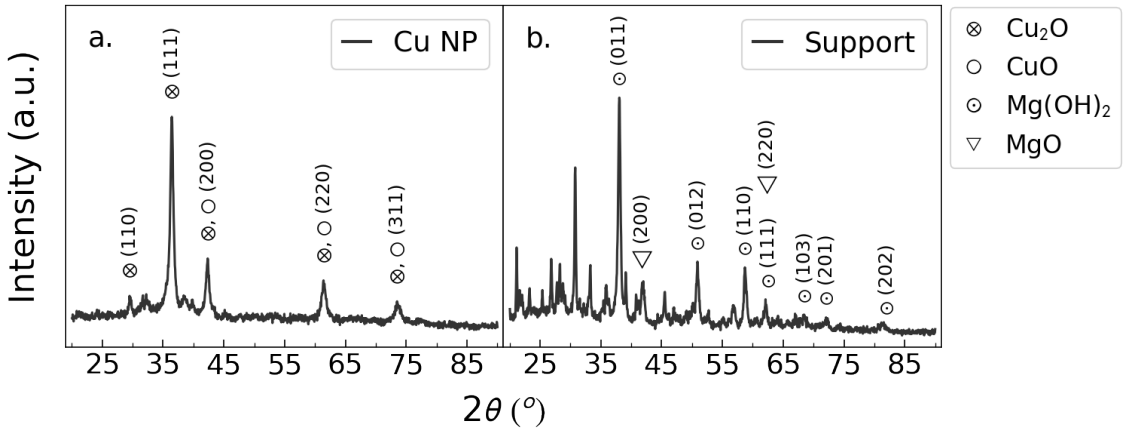

Figure 4.4: Diffractograms of (**a**) Non-supported Cu nanoparticles and (**b**) MgO support, both before the reducing treatment. All unidentified Bragg reflections present in b come from hydromagensite crystal structure.

reducing treatment only by qualitative analysis.

4.4 Nanoparticles Size Comparison

The Rietveld refinement method was used to fit XRD patterns of the as prepared Cu nanoparticles, and the DT_3, DT_4, DT_5 and CT samples after reducing treatment. The XRD patterns of the DT samples before the reducing treatment were not refined due to the high complexity of their diffraction profiles, which comes from the phases existing in the support. However, since the morphological properties of the Cu nanoparticles should not change by supporting them, it is reasonable considering that the size distribution of non-supported Cu nanoparticles is the same than that of the supported Cu nanoparticles before reduction treatment. Fig. 4.6 shows the Rietveld refinement of the XRD patterns for the non-supported Cu and Cu/MgO nanoparticles after reduction treatment at 300°C. In all samples, CuO and Cu_2O crystal structures were initially proposed, whereas Cu and MgO crystal structures were only proposed in Cu/MgO nanoparticles, since there were no characteristic Bragg reflections of these components sufficiently intense in the as prepared Cu nanoparticles sample profile. Nonetheless, table 4.1 shows that some crystal structures do not contribute to the XRD pattern. The only component identified in all the samples was Cu_2O, therefore the mean particle size of the Cu_2O phase was used for comparison purposes. Table 4.2 shows the Cu_2O mean diameter for the CT, DT_3, DT_4 and DT_5 samples after the reduction treatment at 300°C compared to the mean diameter of the as prepared Cu nanoparticles. After the thermal treatment, the control sample CT has a drastic increase in the nanoparticles mean diameter, strongly indicating

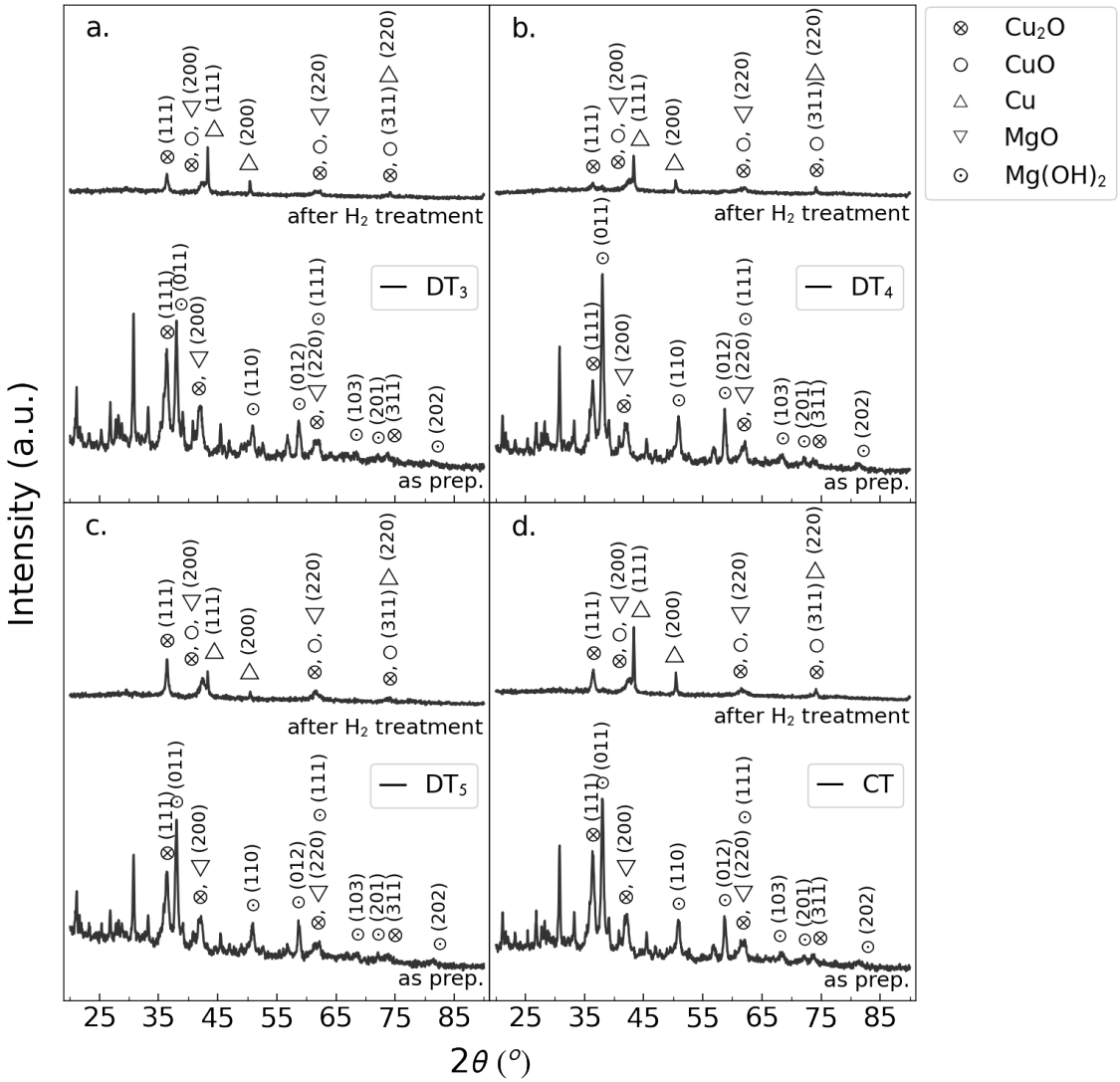

Figure 4.5: Diffractograms of (**a**) DT_3 , (**b**) DT_4, (**c**) DT_5 and(**d**) CT nanoparticles before and after the reduction treatment. All unidentified Bragg reflections before treatment are identified as coming from hydromagensite crystal structure ($Mg_5(CO_3)_4(OH)_2(H_2O)_4$).

sintering. The DT_3, DT_4 and DT_5 samples keep a mean size similar to the non supported Cu nanoparticles before reduction treatment, then indicating sintering was successfully prevented in those samples. The uncertainties were estimated by varying the IG parameter (used for size calculation) until the χ^2 value increased in 10% with respect to the best fit.

It is important to note that methods based on peak width analysis, like the Scherrer's equation, yield a volume weighted mean size value (Kril & Birringer, 1998, Borchert et al., 2005), thus the mean sizes calculated by Rietveld refinement do not represent an arithmetic mean, like those obtained by TEM measurements. Also, neglecting of strain and polydispersion effects yields values that are considerably smaller and larger than the

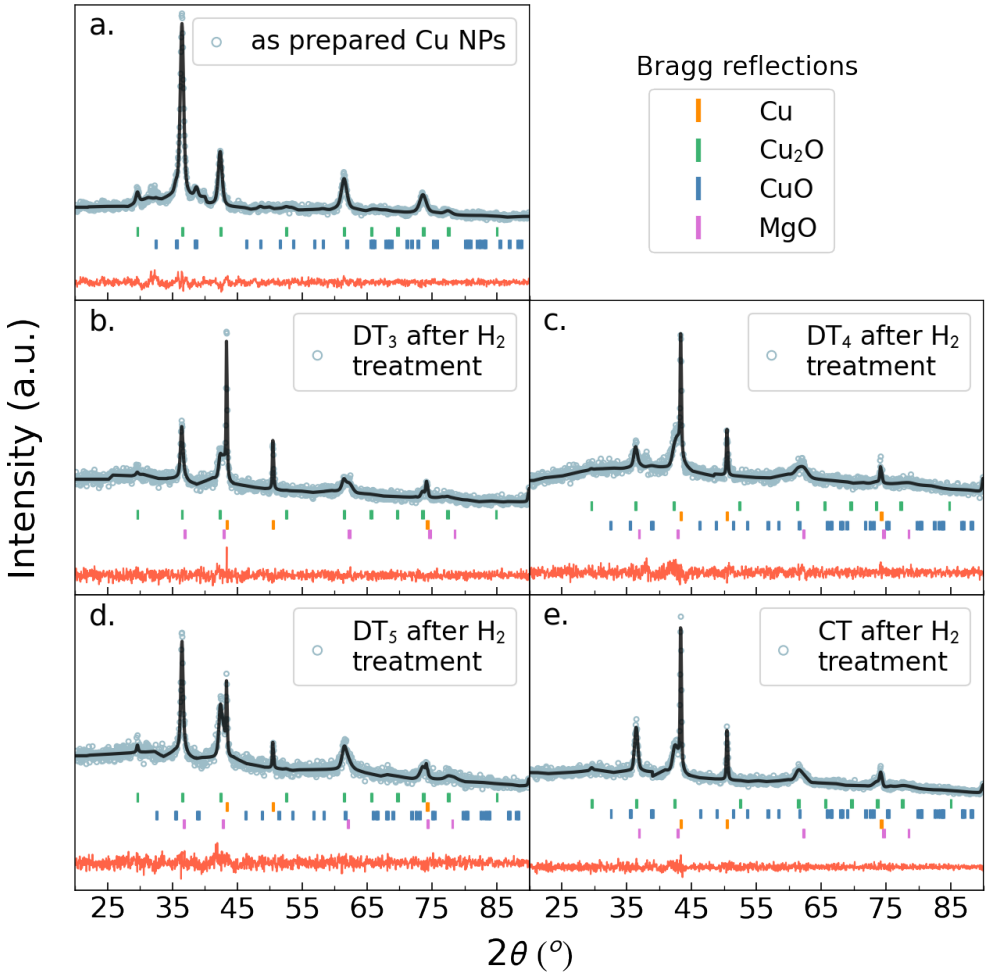

Figure 4.6: Rietveld refinement for (**a**) as prepared Cu nanoparticles and for (**b**) DT_3, (**c**) DT_4, (**d**) DT_5 and **(e)** CT samples after reducing treatment at 300°C. The grey circular points represent the measured data, the solid black line represents the fit and the solid red line represents the subtraction of the calculated and measured profiles. The vertical lines represent the angular position for the Bragg reflections of each crystal structure.

real mean size, respectively (Calvin et al., 2003). The focus of this analysis is on the relative comparison of measured sizes obtained by the same technique before and after the thermal treatment instead of the precise determination of these values.

TEM images were also used to directly compare nanoparticles sizes before and after reducing treatment at 300 °C. Fig. 4.7 shows a typical image of each sample, with the corresponding size distribution histogram in the inset. The histogram is not shown for the CT sample due to the great sintering effect in this case, which implies in a very low amount of large size particles in each TEM image. Although the particles count for the CT sample is insufficient to make a size distribution, there is a clear visual evidence of sintering effect in the images. Fig. 4.7.e shows particles with sizes up to the order of

Table 4.1: Fractions of the proposed structures to the diffraction pattern of each sample, according to Rietveld refinement analysis.

	As prepared	**After H_2 treatment**			
	Cu nanoparticles	DT_3	DT_4	DT_5	CT
Cu_2O	0.91	0.20	0.09	0.27	0.17
CuO	0.09	0.00	0.04	0.00	0.00
Cu	0.00	0.22	0.16	0.08	0.25
MgO	0.00	0.58	0.71	0.65	0.58

Table 4.2: In the top row, the Cu_2O phase nanoparticles mean diameter for each sample, obtained by the Rietveld refinement method. In the bottom row, the χ^2 values for each fit.

	As prepared	**After H_2 treatment**			
	Cu nanoparticles	DT_3	DT_4	DT_5	CT
Mean diameter (nm)	25 ± 15	25 ± 14	22 ± 19	26 ± 12	83 ± 26
χ^2	1.36	1.07	1.07	1.08	1.01

μm, typical of sintered nanoparticles (Jia et al., 2020). This behavior is observed in the full TEM grid and only in this specific sample. Fig. 4.7.a shows that the as prepared nanoparticles are spherical and polydispersed. Comparing figures 4.7.a and 4.7.d, it can be seen that, after the reducing treatment, DT_5 sample presents an increase in the nanoparticles density, which is also observed in DT_3 and DT_4 samples. Furthermore, the morphology and mean size of Cu nanoparticles in DT's samples remain similar to those before the treatment, thereby indicating sintering was prevented. In the Fig. 4.7.b the DT_3 sample image shows the existence of small and some few big nanoparticles, which is reflected on the uncertainty value. On the other hand, DT_4 and DT_5 samples do not present any big nanoparticle in the TEM images. It shows the efficiency of the proposed method to avoid sintering of Cu/MgO nanoparticles.

Fig. 4.8 shows (a) the EXAFS oscillations $\chi(k)$ and (b) the corresponding Fourier Transform at the Cu K edge of the Cu/MgO nanoparticles during reduction treatment and the Cu standard. The EXAFS oscillations of the nanoparticles are similar to those of the Cu standard, which shows the presence of metallic Cu nanoparticles during reduction treatment. Furthermore, the EXAFS oscillations are clearly damped in comparison to those of the Cu standard. It occurs due to the higher temperature of the measurements and smaller size of the Cu/MgO nanoparticles in comparison to the Cu standard. As a consequence, the Fourier Transform is composed mainly by a single component at the Cu-Cu scattering distance (not phase corrected) with smaller height than the Fourier

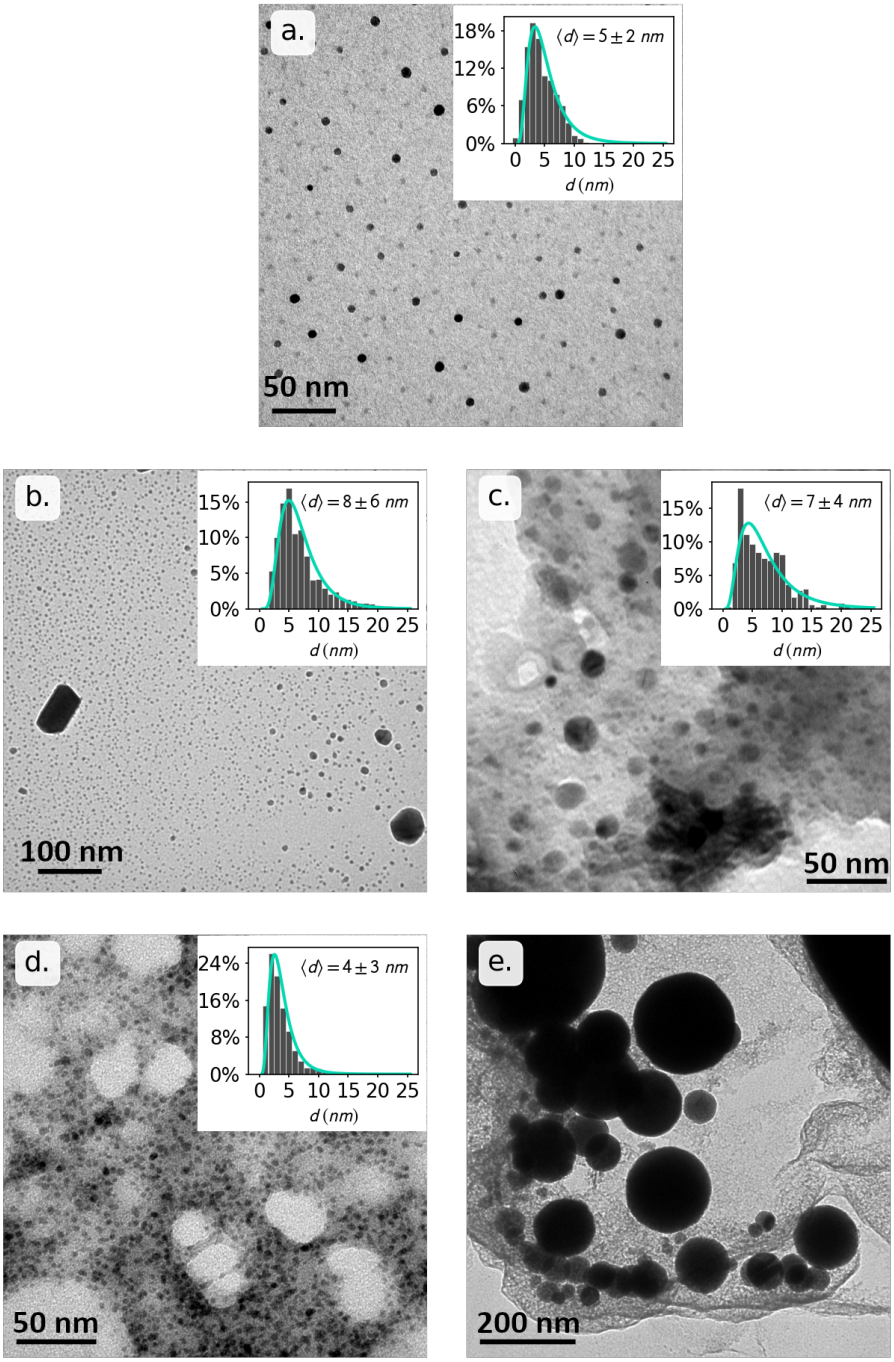

Figure 4.7: Typical TEM images for: (**a**) as prepared DT_5 and (**b**) DT_3, (**c**) DT_4, (**d**) DT_5 and (**e**) CT samples after the H_2 treatment at 300 °C. The inset shows the size distribution fitted by a log normal curve, where the count is given in percentage and D is the particle diameter; $\langle D \rangle$ stands for the arithmetic mean of the diameters.

Transform of Cu standard. It is also interesting to note that the CT sample presents clearly a higher height of the main contribution than the DT samples. Since the measurements are conducted in 300 °C for both CT and DT samples, it comes probably due to a bigger

size of the Cu nanoparticles in the CT sample.

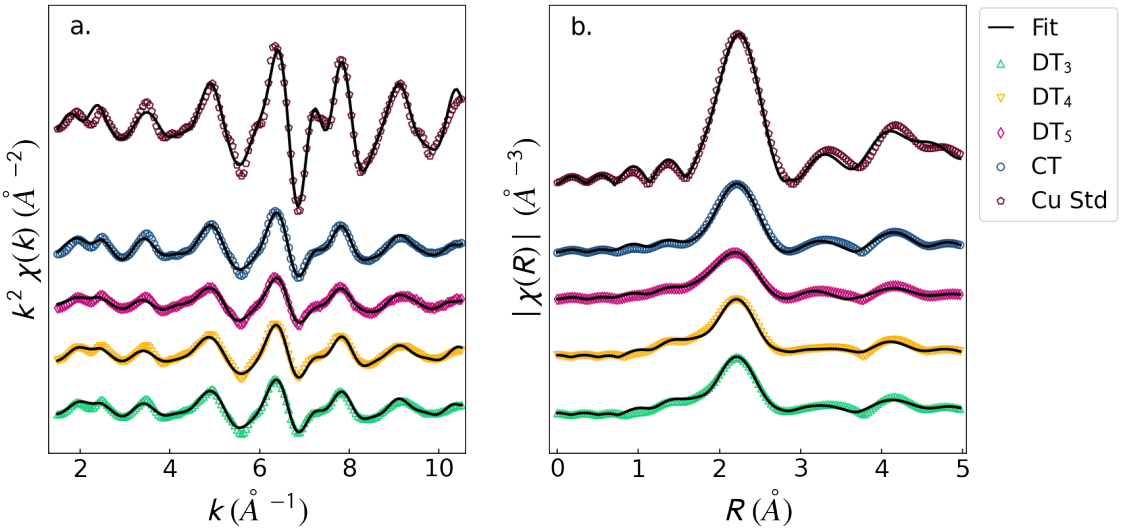

Figure 4.8: (**a**) k^2-weighted EXAFS oscillations and (**b**) the corresponding Fourier Transform. The solid black lines represent the best fit result. The legend is valid for both a and b.

In order to obtain quantitative information, the data were fitted and the fitting results are presented in table 4.3 for the coordination shell. It is possible to observe the Debye-Waller factor in all Cu/MgO nanoparticles is bigger than that from Cu standard and almost the same between the Cu/MgO nanoparticles during reduction treatment at 300 °C. It is expected due to the higher temperature used in the measurements. The Cu-Cu distance is almost constant between the samples and smaller than that found for Cu standard, which is expected for nanoparticles in comparison to bulk samples (Jentys, 1999). The Cu-Cu coordination number is clearly different between the Cu/MgO nanoparticles with the biggest value for the CT sample. The average coordination number is a parameter that directly reflects the mean nanoparticle size due to the termination effect: in comparison to a bulk material, the average coordination number is reduced due to atoms near the boundary. This effect is greater for scattering atoms at greater distances from the absorbing atom. Calvin et al. (2003) proposed a model to relate the mean coordination number with the diameter d of a homogeneous spherical crystallite. The scattering path length r would have its amplitude reduced, relative to that of a bulk standard, by a factor equal to the fraction of the surface area of the scattering sphere that is contained within the crystallite. After integrating through the crystallite sphere and dividing by its volume, the reduction in average coordination number relative to the bulk becomes:

$$N_{nano} = \left[1 - \frac{3}{4}\frac{2r}{d} + \frac{1}{16}\left(\frac{2r}{d}\right)^3\right] N_{bulk} \tag{4.8}$$

where N_{bulk} is the coordination number of the bulk material.

Table 4.3: Parameters obtained from the coordination shell fit.

		N_1	R(Å)	σ^2(Å^2)
Cu Std	Cu-Cu	12	2.54 ± 0.01	0.0081 ± 0.0002
DT_3	Cu-Cu	6.8 ± 0.6	2.534 ± 0.003	0.013 ± 0.001
	Cu-X	0.24 ± 0.07	2.17 ± 0.02	0.002 ± 0.003
DT_4	Cu-Cu	6.6 ± 0.2	2.534 ± 0.002	0.0126 ± 0.0003
	Cu-X	0.43 ± 0.08	2.71 ± 0.02	0.007 ± 0.003
DT_5	Cu-Cu	5.8 ± 0.5	2.522 ± 0.003	0.013 ± 0.001
	Cu-X	0.6 ± 0.01	2.20 ± 0.02	0.013 ± 0.003
CT	Cu-Cu	8.9 ± 0.7	2.531 ± 0.002	0.0132 ± 0.0009
	Cu-X	0.06 ± 0.01	2.17 ± 0.07	0.002 ± 0.008

Eq. 4.8 was used to determine the diameters d for the average coordination number of the first shell N_1 of each sample. The results in table 4.4 show that Cu nanoparticles of the CT sample have a bigger size than those of DT samples, following the XRD and TEM trend. The Cu nanoparticles size are drastically smaller than those obtained by other techniques. However it is necessary to consider that the termination effect depends on the distance of the scattering shell to the absorbing atom. Since it was considered the 1^{st} shell, for particles greater than 10 nm the termination effect becomes much less pronounced. The uncertainties in table 4.4 are propagated from the fit results and then are underestimated but it is hard to determine the real uncertainty in this case. This method for obtaining particle sizes has several limitations, since it considers only spherical particles with uniform atomic density. Other complex phenomena can introduce uncertainties in the coordination number, like the surface atoms contraction in nanometer-sized nanocrystals, since the contraction is coordination dependent (Huang et al., 2008). Furthermore, multiple-scattering contributions are not properly accounted for in this scheme. However, the result allows the estimation of nanoparticles size during reduction treatment (*in situ* measurements), which was not taken into account in the other analysis. Then the results presented in table 4.3 are important since it complements the XRD and TEM results and shows, again, a clear existence of bigger nanoparticles in the CT sample.

The EXAFS technique is more sensitive to small crystallites, whereas XRD analysis is more sensitive to large crystallites (Calvin et al., 2003). Therefore the diameters obtained

Table 4.4: Mean diameters estimated from *in situ* EXAFS analysis.

	N_1	**Mean diameter (nm)**
DT_3	6.8 ± 0.6	$1.2^{+0.2}_{-0.1}$
DT_4	6.6 ± 0.2	1.2 ± 0.1
DT_5	5.8 ± 0.5	1.0 ± 0.1
CT	8.9 ± 0.7	$2.1^{+0.6}_{-0.4}$

from EXAFS represent an inferior limit in the mean size, while the diameters obtained by XRD point to a superior limit. For the sample's TEM size distribution, most of the counts are indeed inside these boundaries. As shown in table 4.5, for all measurements the CT sample presents the larger mean size after thermal treatment, clearly indicating sintering. Although EXAFS analysis does not give a size before treatment for comparison purposes, due to the initial complex composition of the nanoparticles (mixture of CuO, Cu_2O and Cu as obtained from the XANES analysis - see section 4.5), it shows that all the DT samples have similar sizes, which are about half that of the CT sample.

Table 4.5: Mean diameters obtained for each sample by all experimental techniques.

	Mean diameter (nm)				
	TEM		**XRD**		**EXAFS**
	As prepared	After H_2 treatment	As prepared	After H_2 treatment	*In situ*
Cu nanoparticles	-	-	25 ± 15	-	-
DT_3	-	8 ± 6	-	25 ± 14	$1.2^{+0.2}_{-0.1}$
DT_4	-	7 ± 4	-	21 ± 19	1.2 ± 0.1
DT_5	5 ± 2	4 ± 3	-	26 ± 12	1.0 ± 0.1
CT	-	-	-	83 ± 26	$2.1^{+0.6}_{-0.4}$

Upon considering all the analysis, the impregnation of dithiol molecules clearly avoids sintering of Cu nanoparticles supported on MgO exposed to the activation treatment at 300 °C, which was verified by three independent experimental techniques. The sintering prevention is independent of the dithiol molecule used for impregnation (1,3-propanedithiol, 1,4-butanedithiol or 1,5-pentanedithiol). However, this proposal is useful only if no sulfur poisoning of the nanoparticles is observed, which should be investigated.

4.5 Sulfur Poisoning Investigation

For some reactions, sulfur compounds are known to poison Cu-based catalysts (Yang et al., 2018, Shen et al., 2018, Campbell & Koel, 1987), usually by formation of copper sulfate ($CuSO_4$) or copper sulfide (CuS). In order to investigate this possibility, XPS and *in situ* XAS techniques were used.

The Fourier Transform (Fig. 4.8) of the EXAFS oscillations shows the presence of a shoulder at around 1.5 Å(not phase corrected), different to the Cu standard case. If there are Cu-S bondings in the samples, they are expected to affect the EXAFS oscillations pattern at the Cu K edge. Therefore, a Cu-S scattering path was included in the fit of the Fourier Transform of the EXAFS oscilations since the Cu-Cu scattering path itself is not able to fully adjust the coordination shell region of the Fourier Transform. However, it is important to stress out that EXAFS technique is not element sensitive. It means that there is no way to ascertain the presence of S atoms by analyzing only the Fourier Transform. Then this scattering path will be labeled as Cu-X, where X stands for some light element. The parameters obtained from the fitting of the Fourier Transform for the coordination shell are shown in table 4.3. The results point to a small contribution from the Cu-X scattering path to the fit. However, the small values of the Cu-X coordination number indicate that this contribution does not represent large amounts of light atoms in the Cu nanoparticles surroundings. Besides this, the CT sample, which have no dithiol impregnation, also shows a small Cu-X contribution to its EXAFS oscillations. Thus, X can be any atomic species other than S, like O from the support or even from the copper oxide due to the existence of non fully reduced Cu nanoparticles. The XANES region of the absorption spectra is sensitive to the chemical components present in the sample, then a detailed *in situ* time-resolved XANES analysis was conducted aiming to identify the presence or not of S atoms and, in case of S poisoning, the time and temperature needed to poison the Cu nanoparticles.

The normalized *in situ* time-resolved XANES spectra are shown in Fig. 4.9. In this figure, the temperature ramp is represented as a color scale. For each instant, there is a corresponding temperature and a normalized $\mu(E)$ spectrum. In the beginning of the reaction, the XANES spectra of all samples present a well defined contribution between 8980 and 8985 eV. Since the Cu K edge refers to a $1s \rightarrow 4p$ allowed transition (Vaseem et al., 2008), it means that the higher the intensity at this position, the bigger the number of $4p$ empty electronic states. Moreover, the XANES fingerprints are consistent with the presence of Cu(I) oxidation state. During the reaction, the first contribution becomes smaller, and a maximum arises in the region between 9010 and 9040 eV. These features are commonly observed in metallic Cu (Matte et al., 2015). For a quantitative analysis, it

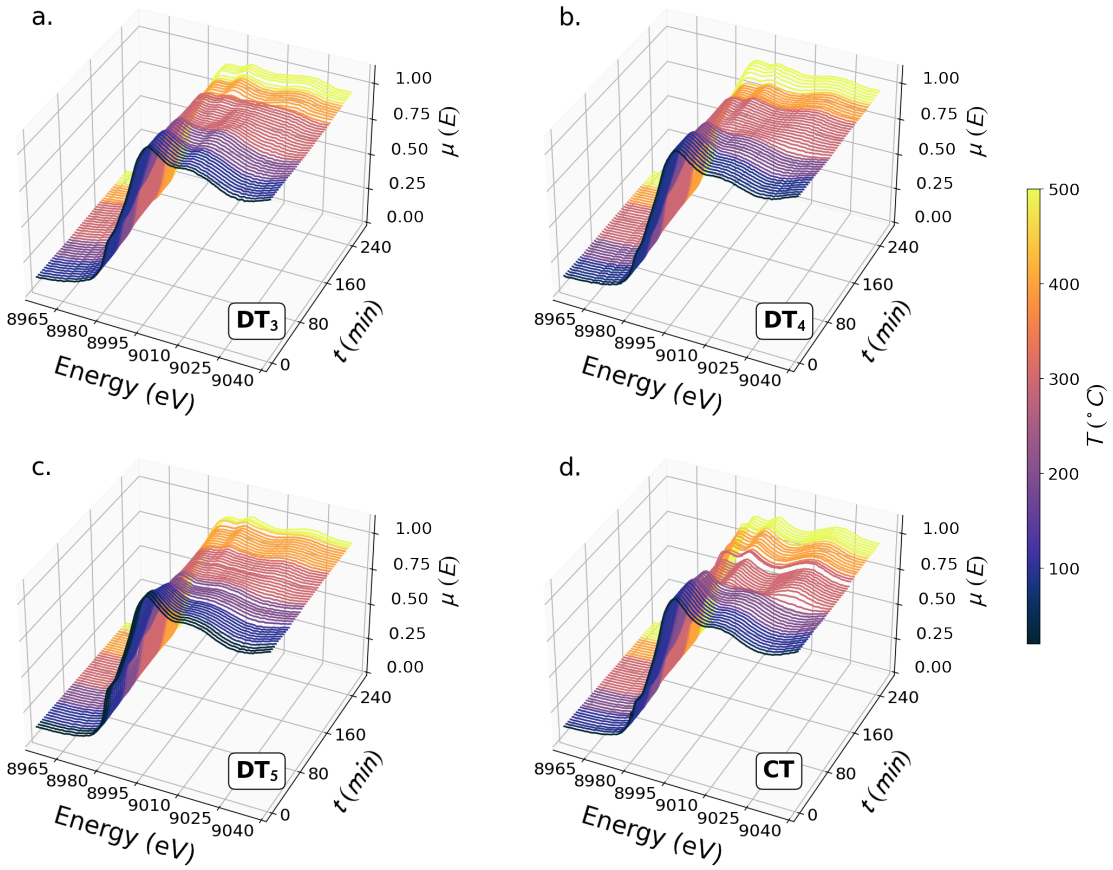

Figure 4.9: *In situ* time-resolved XANES spectra at Cu K edge of (**a**) DT_3, (**b**) DT_4, (**c**) DT_5 and (**d**) CT samples during reduction treatment.

was performed a LCF of the spectra with previously measured standards. The following standard spectra were used in the LCF: Cu, CuO, Cu_2O, $CuSO_4$, copper(II) chloride dihydrate ($CuCl_2 \cdot 2H_2O$) and copper(II) hydroxide ($Cu(OH)_2$). The copper chloride dihydrate was included as a possible residue from the nanoparticles synthesis. Fig. 4.10 shows typical XANES spectra, in addition to their linear combination fit.

Fig. 4.11 shows, for each component that did not give a null contribution, the fraction found at each instant of time t and temperature T by the LCF. Only Cu, CuO and Cu_2O XANES spectra contributed to the fit, for all the samples. Therefore, it shows the absence of Cu-S bonds, implying in the absence of sulfur poisoning in the Cu nanoparticles. The initial chemical state is a mixture of CuO, Cu_2O and Cu for all samples, but the main component is Cu_2O (around 60%) that presents Cu(I) oxidation state. After 50 min of starting the heating treatment, at around 200 °C, CuO starts to reduce to Cu_2O. Then, near 100 min of reaction, when temperature reaches 300 °C, Cu_2O starts reducing to Cu. At the end of the reaction, the samples present around 70% of Cu and 30% of Cu_2O, whereas

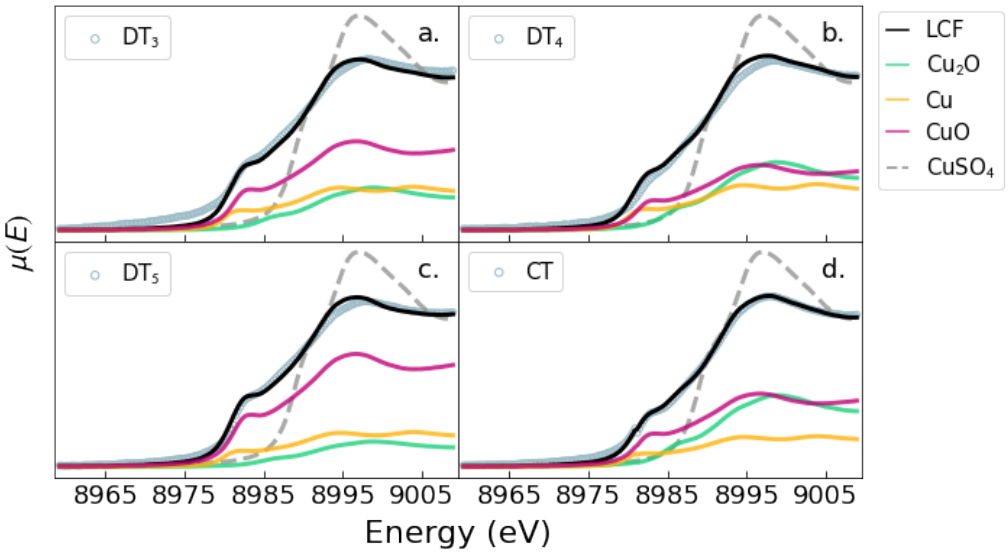

Figure 4.10: Linear combination fit of a typical XANES spectrum during reduction treatment of (**a**) DT_3, (**b**) DT_4, (**c**) DT_5 and (**d**) CT samples. The dashed line show a $CuSO_4$ standard.

CuO is no longer detected. Althoug all samples show the same reducing steps, the CT sample has a deeper change in both stages of reduction. For bulk materials, the reduction of CuO to Cu_2O presents a smaller activation energy than the reduction of Cu_2O to Cu (Kim et al., 2003, Reitz et al., 2001). The CuO species in bulk materials reduce directly to metallic Cu without formation of a stable intermediate or suboxide, except under controlled reaction conditions (limited flow, temperature and reactant supply), and only as a transient species (Rodriguez et al., 2003, Wang et al., 2004). However, nanoparticles have been related to show an intermediate Cu_2O formation in the CuO $\rightarrow$ Cu reduction, besides forming a stable Cu_2O phase (Pike et al., 2006). It is also important to notice that for nanoparticles the reduction rate is size dependent. This effect could be related to the difference between CT and DT samples reducing rates, since the sintering effect was observed in CT samples.

XPS is a highly sensitive technique well suited to examining the composition and chemical components at the materials surface. Fig. 4.12 shows a typical long scan (DT_5 sample after H_2 treatment), with all electronic regions identified. All samples show the same components in the long scan, with exception of the CT sample, which does not present sulfur. The detection of Na and Cl is expected and come as remnant from synthesis. Furthermore, the expected presence of Cu, O, Mg, S and C were confirmed by the long scan spectrum.

Fig. 4.13 shows the Cu $2p_{3/2}$ XPS spectrum of the samples before and after reducing

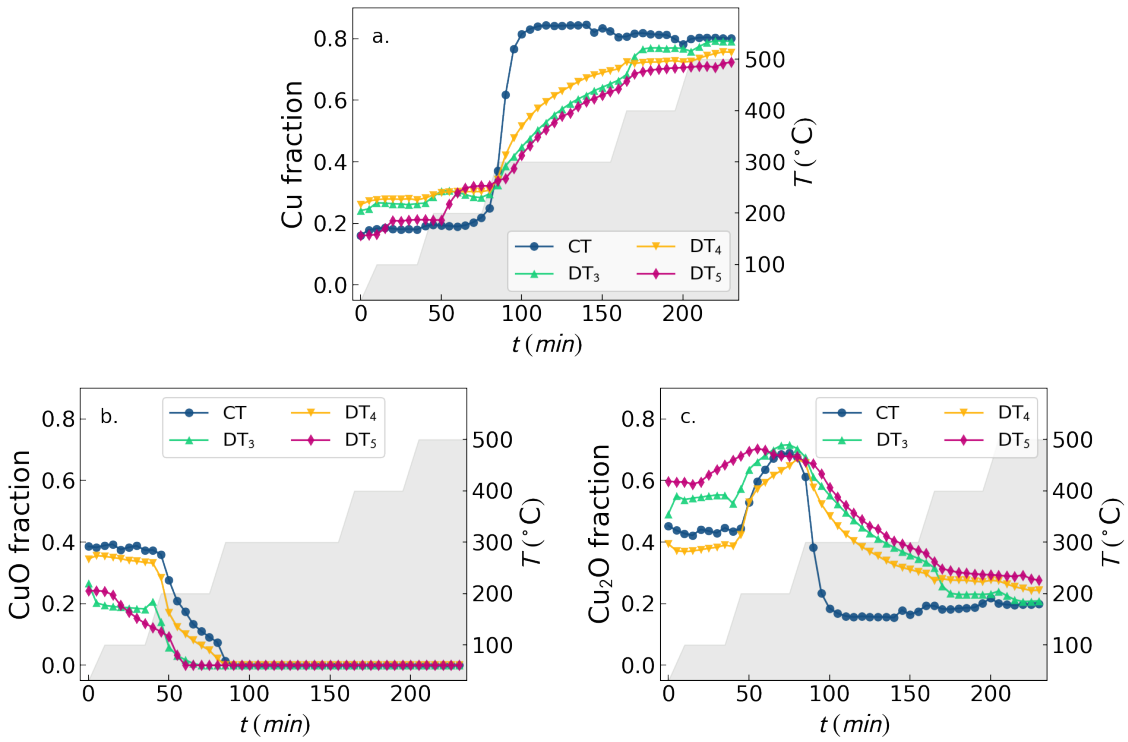

Figure 4.11: Time variation of (**a**) Cu, (**b**) CuO and (**c**) Cu_2O fraction for each sample during reduction treatment obtained from in situ time-resolved XANES measurements. The solid gray step-like region describes the temperature variation, given by the right vertical axis.

treatment. The Cu $2p_{3/2}$ region exhibits two strong signals at 932.8 eV and 934.5 eV. The first binding energy is characteristic of Cu_2O (Vasquez, 1998a), while the latter is typical of CuO (Vasquez, 1998b). Metallic Cu is also associated to a binding energy very close to that of Cu_2O. In fact, the best way to distinguish between Cu and Cu_2O at the surface region is using Auger spectra instead of XPS. However, the main focus here is on the identification of a possible sulfur poisoning and Auger emission measurements were not carried out. The energy position is consistent with the presence of Cu_2O, which makes sense since Cu nanoparticles are highly oxidizable under exposition to the atmosphere. Furthermore, the as prepared samples show mainly Cu_2O in the XANES spectra (Fig. 4.11), then consistent with this identification. A Cu sulfate component is not observed since it is associated to binding energies of ∼936 eV (Hayez et al., 2004, Vasquez, 1998c), which is far away to the CuO component (934.5 eV). Cu sulfides have a Cu $2p_{3/2}$ binding energy very close to ∼ 932.5 eV (Krylova & Andrulevičius, 2009), independent of the value of x, then close to the observed component at 932.8 eV that is associated to Cu_2O. However, if Cu sulfidization where to happen under heating, the Cu_2S component should grow in intensity after the H_2 treatment at 300° (Liu et al., 2020), and this behaviour is

not consistently observed throughout the samples' spectra, since DT_5 even show a slight reduction in this component intensity. To further investigate the possibility of Cu-S bonds, the S $2p$ region was analysed (Fig. 4.14).

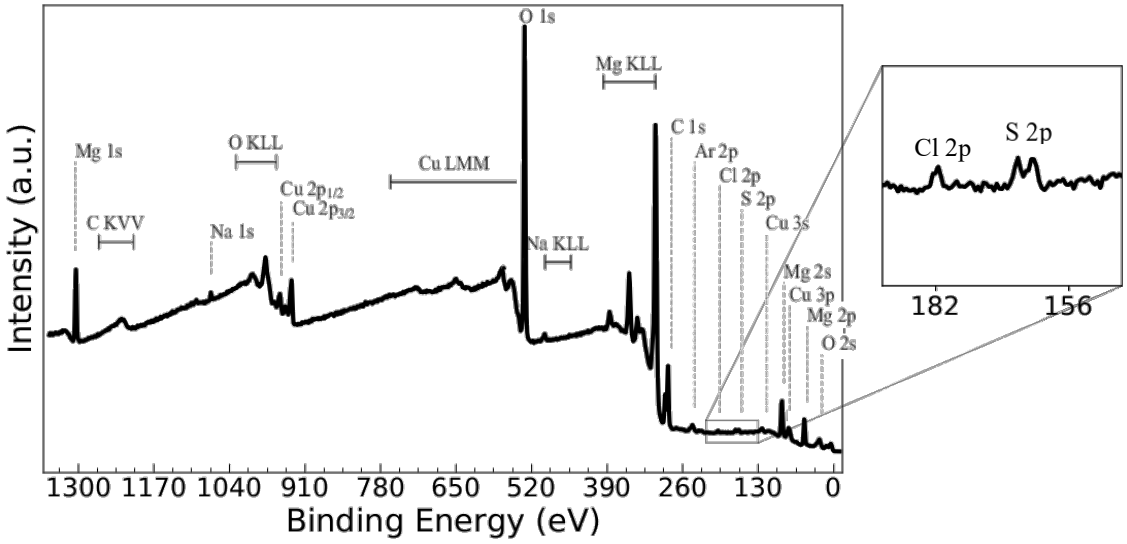

Figure 4.12: Long scan spectrum of DT_5 sample after H_2 treatment at 300 °C.

Coponents from the S $2p$ region present a spin orbit splitting of 1.16 eV, which is too small for the S $2p_{1/2}$ and $2p_{3/2}$ components be individually resolved. This result in the shoulders seen in the adjusted profiles in Fig. 4.14. From Fig. 4.14.a it can be seen that the CT sample presents only background noise, confirming that it is a control sample with no dithiol impregnation. The samples before reducing treatment present two main components at around 162.5 eV and 163.5 eV. The first component can be assigned to either Cu or Mg sulfides (Fantauzzi et al., 2015). The dithiol molecules are expected to interact with metals through the S atom, forming metal-S bonds, hence Cu and Mg sulfides can be interpreted as a dithiol adsorbed to the nanoparticles or the support, respectively. Besides this, it could be related to an Mg-SR^+ complex, where R is an organic group, similar to the Zn-SR^+ complexes that Soares et al. (2011) observed in addition to 1-dodecanethiol adsorption on ZnO. The Mg sulfides MgS_x, with $1 \leq x \leq 2$ have a considerable range of possible binding energies, from ∼163.5 eV for slightly reduced S species (x∼2), to ∼161.5 eV for highly reduced S species (x∼1) (Gao et al., 2015, 2017, 2018). On the other hand, the Cu sulfides Cu_xS, with $1 \leq x \leq 2$, have much smaller variations in binding energies (<0.3 eV) depending on the oxidation state (Kalanur & Seo, 2018, Parreira et al., 2011, Qiu et al., 2016). Considering this, the large shift of ∼0.7 eV to smaller binding energies of this component after reducing treatment suggests that the signal does not come from Cu_xS. Gao et al. (2015) observed that an

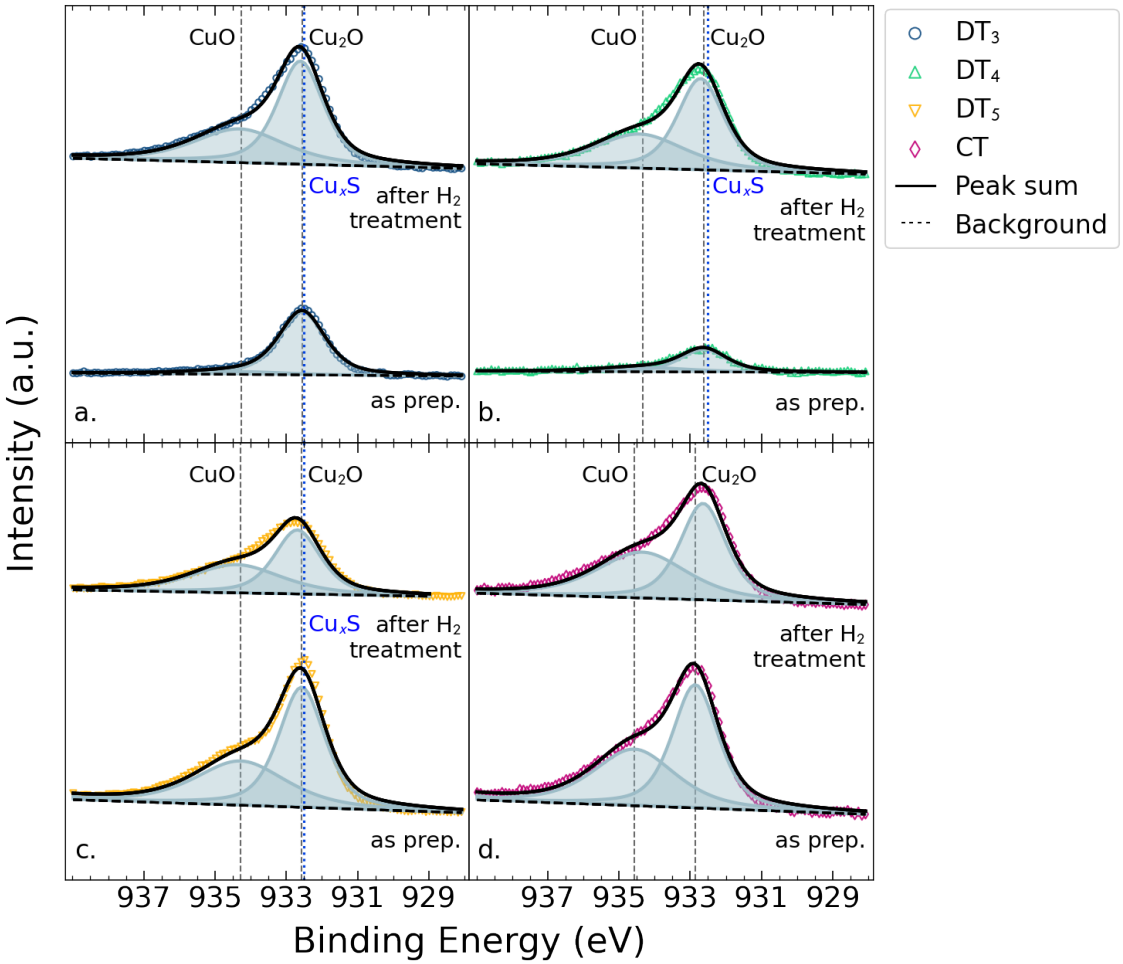

Figure 4.13: Cu $2p_{3/2}$ XPS spectra of samples (**a**) DT_3 , (**b**) DT_4, (**c**) DT_5 and (**d**) CT samples before and after reducing treatment.

Mg surface typically contains multiple chemical states of sulfur, therefore the presence of signals coming from both slightly and partially reduced S in MgS_x is also possible. The component at 163.5 eV could be also associated to a thiol bond with a metal oxide (Volmer et al., 1990), or even to unbounded thiol complexes (Bensebaa et al., 1998). Since the dithiol molecule has two thiol terminations, it has the possibility of bonding with other species in both or one of the extremes or even do not bond. After the reducing treatment, a new component with appears at ∼169 eV, which is due to sulfonate (Bensebaa et al., 1998, Volmer et al., 1990) or a metal sulfate. The sulfonate complex is characterized by the functional group R-SO_3^-, where R is an organic group. A metal sulfate represents any metal bonded with the polyatomic anion SO_4^{-2}. The oxidation of thiol complexes to sulfonate when exposed to ambient atmosphere have been reported to produce a signal at around 169 eV (Laibinis et al., 1991), in the same way as $MgSO_4$ (Gao et al., 2015).

Therefore, the XPS spectra after treatment suggests that a fraction of the dithiol molecules cleaved at high temperatures forming thiol complexes. Then the thiol complexes oxidize to sulfonate after re-exposure to ambient atmosphere and/or react with a metal to form a metal sulfate. From Cu $2p_{3/2}$ analysis, the formation of Cu sulfate was discarded, remaining $MgSO_4$ and/or sulfonate as the assignments for the signal at ~169 eV. From XPS data the S/Cu ratio was calculated. After the H_2 treatment at 300 °C, the S/Cu ratio is 20-40% of the initial value, which may be associated to the loss of S atoms during thermal treatment.

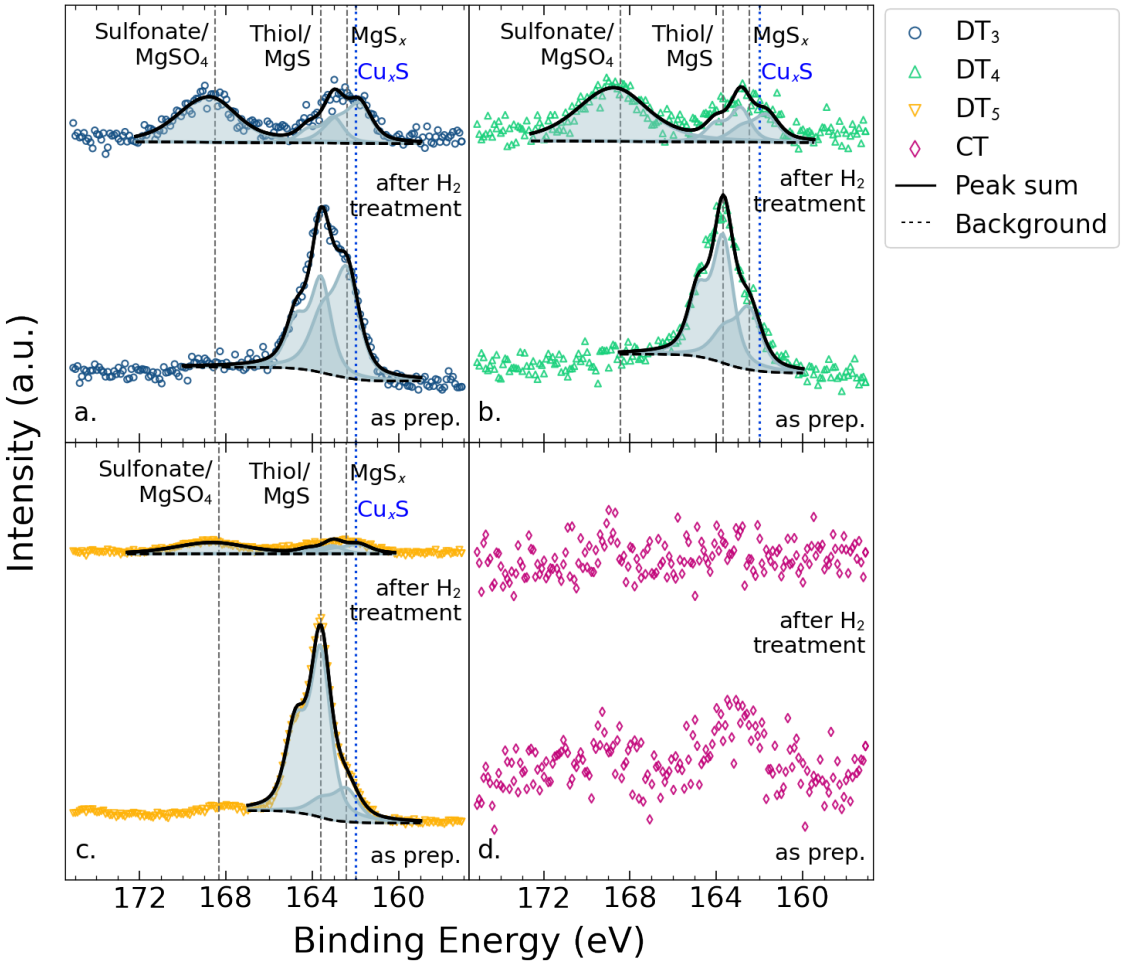

Figure 4.14: S $2p$ XPS spectra of (**a**) DT_3 , (**b**) DT_4, (**c**) DT_5 and (**d**) CT samples before and after reducing treatment.

Despite the presence of the new component after treatment, the two signals at 162.5 and 163.5 eV remain present. However, these components present a considerable shift to smaller energies and smaller relative intensity. The signals are still related to the same composites than before heating. Since the components present the same relative binding

energy in all samples, this shift is likely to represent the reducing of S atoms in MgS_x after the treatment in H_2 atmosphere. The change in the binding energies could also represent the formation of new composites containing Cu-S, Mg-S or S-S bonds. However, the possibility of disulfide formation is unlikely, since at high temperatures S-S cleaves in contact with transition metals (Bain et al., 1989). For Cu-S bonds, dithiol is expected to bind with metallic species by cleavage of the S-H bond and subsequently bonding with Cu(II) species (Volmer et al., 1990). From Cu $2p_{3/2}$ analysis, there is no new component after reducing treatment, then discarding the appearance of Cu-S bonds. Besides this, the *in situ* time-resolved XANES analysis show the absence of CuO during reduction treatment at 300 °C. The presence of CuO in the Cu $2p_{3/2}$ XPS spectra after reducing treatment comes from re-oxidation after atmosphere exposition, as expected. Moreover, after the thermal treatment the shift to lower binding energies takes it further away from the typical binding energies of Cu sulfates.

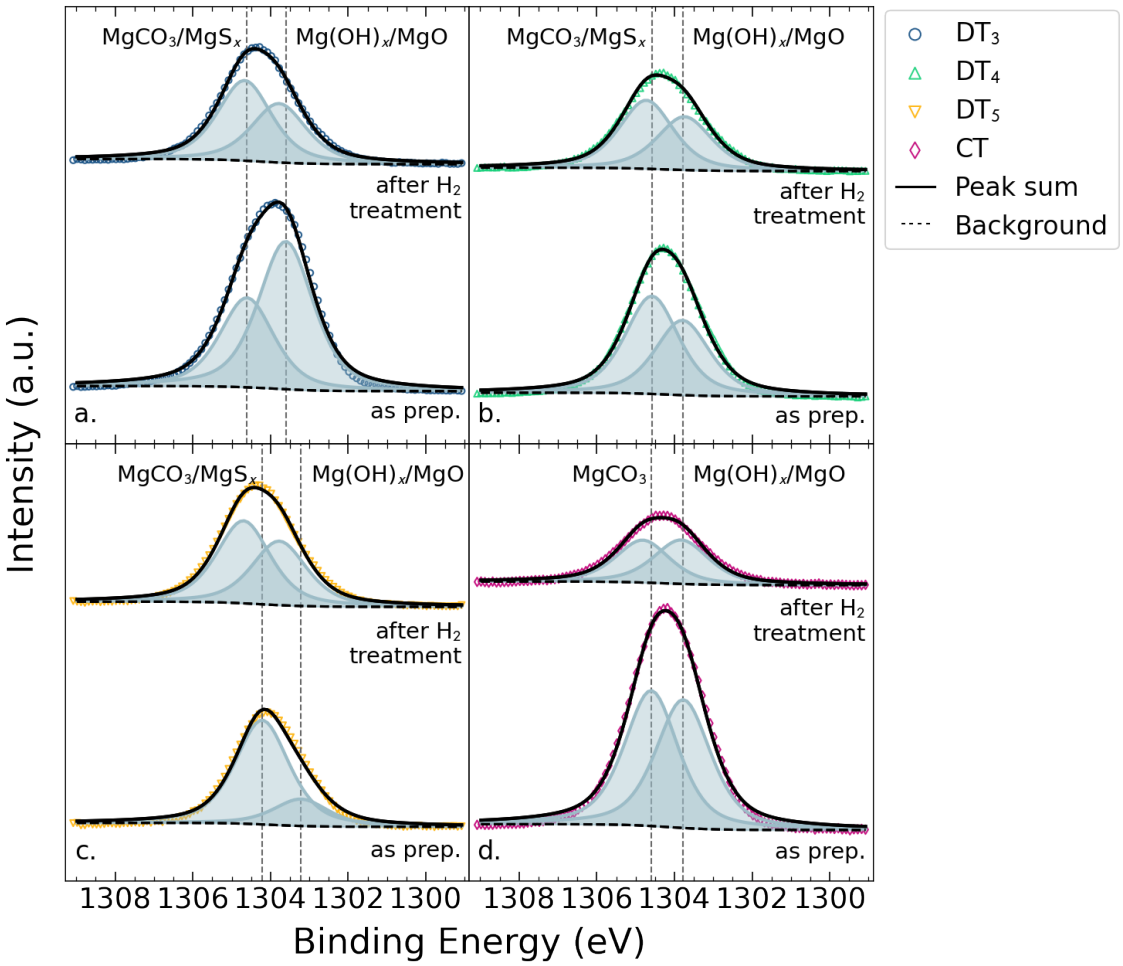

Figure 4.15: Mg $1s$ XPS spectra of (**a**) DT_3 , (**b**) DT_4, (**c**) DT_5 and (**d**) CT samples before and after reducing treatment.

In the *in situ* time-resolved XANES analysis, at the Cu K-edge, only Cu_2O, CuO and Cu contributed to the linear combination fit. This result is corroborated by the XPS spectra interpretation of Cu $2p_{3/2}$ and S $2p$ regions. Nevertheless, the thiol adsorption on the support must be corroborated by Mg $1s$ XPS analysis. Fig. 4.15 shows that all samples had the same composites identified, with exception of the CT sample, where there is no MgS_x component. The signal at ∼1303.5 eV is associated to $Mg(OH)_x$ and/or MgO (Khairallah et al., 2010). At 1304.5 eV the signal is related to $MgCO_3$ (Khairallah & Glisenti, 2006) and/or MgS_x (Gao et al., 2018). One or more Mg(II) components are expected to be present, especially from Mg-O bonds. It is usual that magnesium oxide (MgO), carbonate ($MgCO_3$) and hydroxide ($Mg(OH)_2$) be simultaneously detected in XPS analysis of MgO samples that were exposed to ambient atmosphere (Khairallah & Glisenti, 2006, Khairallah et al., 2010, Jensen et al., 2010, Gao et al., 2018). After the thermal treatment, a shift to higher energies by a similar value (∼0.4 eV) is observed for both components. For the MgS_x component, the energy shift direction agrees with the reducing of sulfur atoms in MgS_x. This corroborates the previous interpretation of the S $2p$ spectra, where dithiol molecules adsorb on the MgO support. The MgO/$Mg(OH)_x$ shift may have a similar explanation, where the Mg atoms in $Mg(OH)_x$ oxidize during reduction treatment, while the $(OH)_x$ species reduce.

4.6 Proposed Mechanism for Sintering Prevention

The introduction of obstacles in a surface containing random walkers is known to result in anomalous diffusion, where the diffusion coefficient becomes time dependent and decreases with an increase in obstacles concentration (Saxton, 1994). The inclusion of a coalescence mechanism gives rise to another possible event: a particle can grow to a size in which nearby obstacles can trap it. Depending on the concentration and size of obstacles, a particle can have a critical radius for which any attempt of movement results in a particle-obstacle collision. Fig. 4.16 depicts a trapped nanoparticle, where in any direction it moves, it encounters a dithiol molecule.

To illustrate how the occupation fraction of obstacles affects the probability of particle entrapment, consider N_{obs} obstacles of radius R_{obs} placed on a square grid of area of L^2, as Fig. 4.17 exemplifies. Then a particle with radius R can only move perpendicularly across the line connecting two obstacles if its diameter is smaller than the distance between the obstacles, otherwise there will be a collision. Hence, defining the minimum particle radius for which it becomes trapped as the critical radius R^*, we have:

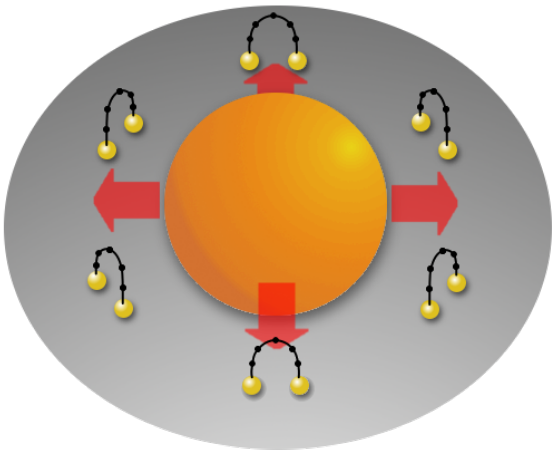

Figure 4.16: Representation of a Cu nanoparticle (central orange sphere) trapped by dithiol molecules (yellow and black spheres represent the S and C atoms in the dithiol molecules). The grey surface represents a very small area of the the MgO support. The sizes are merely representative. In this work, most of the nanoparticles are in the range of 2-10 nm, whereas the largest dithiol molecule (1,5-pentanedithiol from D_5) has a length of ∼0.8 nm.

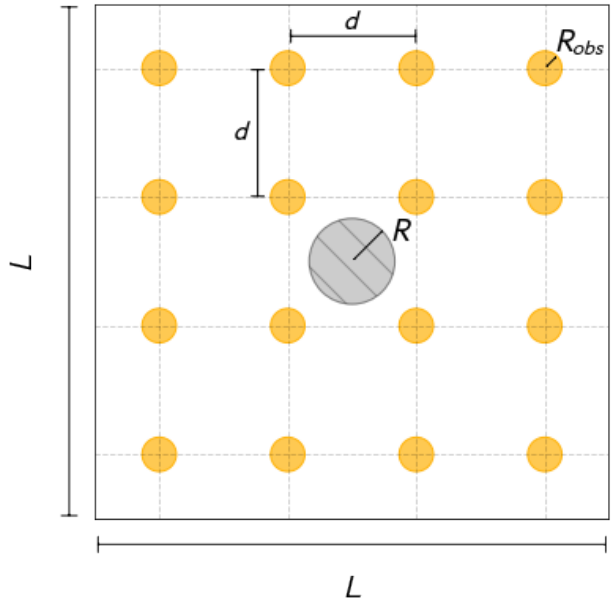

Figure 4.17: Scheme to illustrate obstacles (solid yellow circles) with radius R_{obs} positioned in a square grid of side L. A particle with radius R is represented by the circle with hashed gray filling. The maximum diameter a particle can have without being trapped is $R^* = d - 2R_{obs}$. For a square grid, $d = L/\sqrt{N_{obs}}$, where N_{obs} is the number of obstacles.

$$2R^* = d - 2R_{obs} \tag{4.9}$$

$$= L/\sqrt{N_{obs}} - 2R_{obs} \tag{4.10}$$

Now, let the obstacles occupation fraction be defined as:

$$\phi_{obs} = \frac{1}{L^2}\sum_i \pi {R_{obs}}_i^2 \tag{4.11}$$

since all obstacles have the same size, Eq. 4.11 gives $\phi_{obs} = N_{obs}\pi R_{obs}^2/L^2$. Then, for a given ϕ_{obs} and an N_{obs} with integer square root,

$$\frac{R_{obs}}{L} = \sqrt{\frac{\phi_{obs}}{\pi N_{obs}}} \tag{4.12}$$

which combined with 4.10 gives:

$$\frac{R^*}{L} = \frac{1}{2\sqrt{N_{obs}}} - \frac{R_{obs}}{L} \tag{4.13}$$

Fig. 4.18 shows how R^* depends on ϕ_{obs} and N_{obs}. It can be seen that, for a fixed obstacles size, increasing ϕ_{obs} and N_{obs} will result in the entrapment of smaller particles. Evidently, when modelling real systems such an ordered distribution of obstacles is unlikely, making the entrapment configurations much more complex. However, the probability of particle entrapment must grow with ϕ_{obs} and N_{obs}, even for randomly placed obstacles.

4.6.1 Numerical Simulation

In the simulation, both particles and obstacles have an occupation fraction. Therefore, the total occupation fraction ϕ is defined as the sum of the obstacles and particles occupation fraction:

$$\phi = \frac{\sum_i \pi {R_{obs}}_i^2}{L^2} + \frac{\sum_i \pi R_i^2}{L^2} \tag{4.14}$$

where R_{obsi} and R_i stands for the i^{th} obstacle and particle radius, respectively. The total occupation fraction at the beginning of the simulation is represented by ϕ_0. All obstacles have a fixed radius $R_{obs} = 0.1$. The particles have a time dependent radius $R(t)$, which varies due to the implemented coalescence mechanism. However, at the beginning of simulation all particles radius are set to the same value $R_0 = 1$. The length L of the

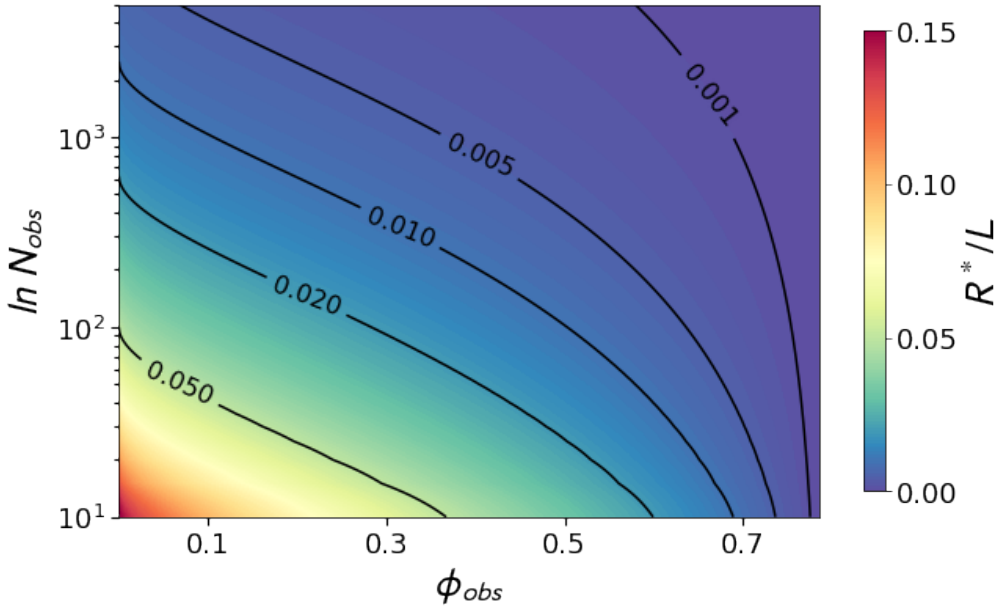

Figure 4.18: The color scale represents the R^*/L values, which is the minimum radius for a particle to be trapped, given as a fraction of L (the side of the square surface containing the particles/obstacles). Some level curves are shown in the diagram. Higher ϕ_{obs} and N_{obs} ensures entrapment of smaller particles.

simulation area is calculated from Eq. 4.14 as :

$$L = \sqrt{\frac{N_{obs}\pi {R_{obs}}^2 + N_{par}\pi {R_0}^2}{\phi_0}} \,, \tag{4.15}$$

where N_{par} is the number of particles in the simulation. The value of ϕ_0 was experimentally estimated so it could serve as a reference for the numerical parameters. Using the Brunauer–Emmett–Teller (BET) multipoint technique of analysis of N_2 adsorption-desorption isotherms measurements, the specific surface area of the MgO used as support was measured. Then, the total projected area of Cu nanoparticles was calculated. For an fcc crystal, such as Cu, the number of atoms can be approximated by (van der Klink & Brom, 2000)

$$N_{at} = \frac{16\pi}{3}\left(\frac{R}{a}\right)^3 \,, \tag{4.16}$$

where a is the unit cell size and R is the radius of the particle. Using the known mass of Cu and dithiol in the samples and assuming that all Cu nanoparticles are metallic and have the same size (5 nm, which is around the mean size from TEM before heating), the number of atoms per nanoparticle is calculated. From this the number of nanoparticles and its total projected area is calculated. The estimation gives $\phi_0 \sim 0.3$.

To evaluate a time scale for the simulation, the relation between the diffusion coefficient and the step size of random walks in the continuous time limit was used (Eq. 3.18). Setting $\Delta = \lambda_0$ and $D = D_0$, where λ_0 and D_0 are, respectively, the typical jump size and the diffusion coefficient of particles at the beginning of the simulation, gives:

$$\tau = \frac{\lambda^2}{4D_0} = \frac{K^2}{2{R_0}^4 D_0} \,, \tag{4.17}$$

where R_0 stands for the mean particle radius at the beginning of the simulation and K is a constant introduced in Eq. 4.5 which relates λ and R. For R_0, the experimental mean particle size obtained by TEM analysis for the DT_5 sample is used, which is 5 nm; for D_0, values of Cu nanoparticles self-diffusion coefficients at temperatures near 300 °C were searched on the literature. Due to the high variance on the diffusion coefficient values, the general magnitude order of 1 nm^2/ns is used (Kart et al., 2014, Yang & Sacher, 2001, Hoehne & Sizmann, 1971). The constant K was set to numerical value of 1 in the simulation and has units of nm. With these values, each MC step would represent a time variation of $\tau = 0.01$ ns. This means that the simulations, with a total number of 10^5 MC steps represents a time scale of 1 μs. Naturally this is a very small time regime to represent a realistic experiment, and this is a common issue in Monte Carlo simulations Limoge & Bocquet (1988), Voter et al. (2002). The time range of 1 μs is not enough to observe the sintering behaviour of a real system. Due to computational limits, one can not simulate realistic motion rates within this small time scale because it becomes impossible for the simulation to present any interesting phenomena. Thus, the simulation presents a faster version of what would be observed in reality. As for the length scale, the unity is set to 2.5 nm, so the nanoparticles start with an uniform diameter distribution of 5 nm, whereas the obstacles, which represent the dithiol molecules, have 0.5 nm of diameter.

For the simulations conduction, first the number of particles is fixed at $N_{par} = 1000$ and the effect of the obstacles presence in sintering prevention is explored. Then $N_{par} = 2000, 5000, 10000$ was varied to test the effect of finite size of the system. The particles and obstacles are well dispersed before the simulation begins.

For any quantity of obstacles, the method proved to be extremely efficient in restricting coalescence. In Fig. 4.19.a are shown the stacked size distributions for different obstacle fractions after 10^5 MC steps, with $N_{par} = 1000$ and $\phi = 0.5$. In the stacked histograms, multiple data are stacked on top of each other, which means that for a given x the count value of one data set starts where other ends (there is no superpositions). The sum of the histograms is normalized to one. Fig. 4.19.b presents the mean particle radius at the end of the simulation with is standard deviation. There is an evident reduction in final mean sizes after the introduction of obstacles, which increases with N_{obs}/N_{par}. The only

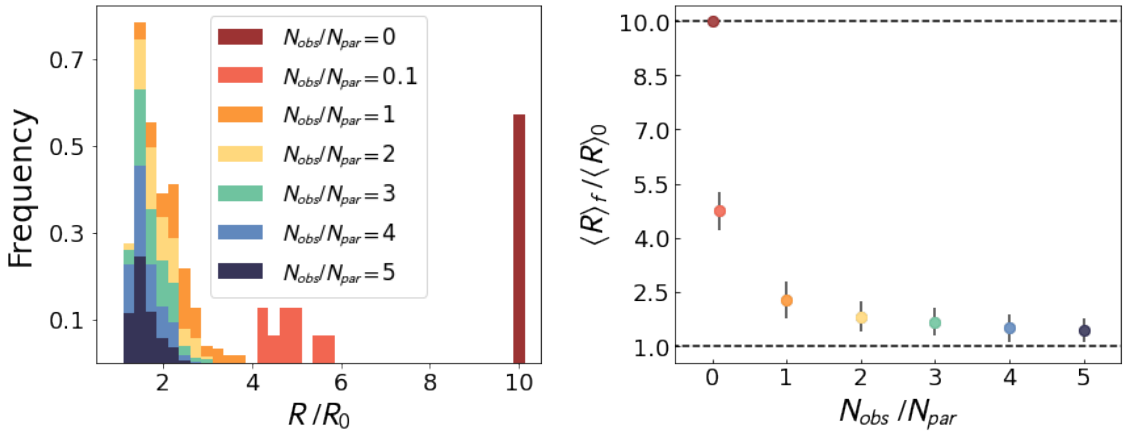

Figure 4.19: (**a**) Stacked particle size distribution and (**b**) increase factor of mean particle radius ($\langle R\rangle_f$ /$\langle R\rangle_0$) in function of obstacles fraction, for $\phi_0 = 0.5$ and $N_{par} = 1000$. In b, the lower and upper dashed lines represent the mean particle radius for the cases in which no particles and all particles have sintered, respectively. The mean values and standard deviation for each color is calculated from the size distribution corresponding to the same color. When all particles are sintered to a single one its radius will be $R_{sinter} = (N_{par}R_0)^{1/3}$. Only for a scenario without obstacles the particles fully sinter. With $N_{obs}/N_{par} > 0$ coalescence is drastically reduced.

scenarios in which particles fully sintered (only a single particle with all the initial mass remains in the end of simulation) were the ones without obstacles. Also, regardless of having used an uniform initial particle size distribution and from the small simulation size, the final distributions have similar behaviour to ones expected from nanoparticles, as the distributions obtained by TEM show (Fig. 4.7).

To explore how ϕ_0 influence in the particles final mean radius, simulations with 19 values in the range of 0.01-0.8 were carried out. Since the number of particles is fixed at $N_{par} = 1000$, variations in the value of ϕ_0 come strictly from changing ϕ_{obs} and/or the length L of the simulation area. For each ϕ_0 and N_{obs}/N_{par}, an $\langle R\rangle_f$ /$\langle R\rangle_0$ value was obtained at the end of the simulation, culminating in Fig. 4.20. The line shown in the figure represents the value at which the average particle sizes double in respect to their sizes at the beginning of the simulations, $\langle R\rangle_f$ /$\langle R\rangle_0 = 2$. Because the value 2 is arbitrary we have tested several others and the qualitative result is robust: the position of the line changes, not its shape. Below this line particles coalesce; above it, sintering is avoided. The result resembles the ones obtained for the critical particle radius in the grid of obstacles (Fig. 4.18). As in the simple grid model, higher occupation fractions and number of obstacles increase the entrapment probability of smaller particles, giving lower final mean particle radius. It is important to note that, when the system has very low density, the time necessary to observe a change in the simulations is too large.

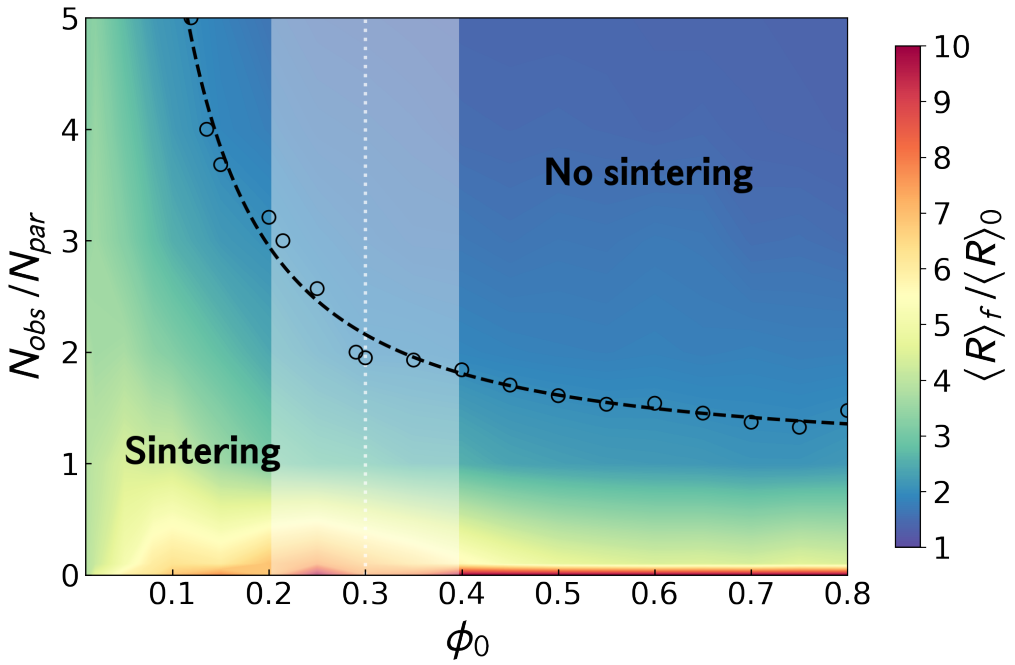

Figure 4.20: $\langle R\rangle_f\ /\langle R\rangle_0$ fraction in function of ϕ_0 and N_{obs}/N_{par}. The points represent coordinates for $\langle R\rangle_f\ /\langle R\rangle_0 = 2$. They were fitted by the function $y(x) = a + bx^n$, resulting in an the asymptotic limit of $N_{obs}/N_{par} \simeq 1.06$. This level curve is defined to delimit the boundary for sintering prevention.

In the simulations, for $\phi_0 < 0.1$ particles avoid coalescence mostly due to the large average distance between them instead of from being restrained by the obstacles. The ϕ_0 experimental value estimated for our samples is of ~ 0.3, well above this value. Also, the experimental time range under high temperatures is much larger, hence the Cu nanoparticles and the dithiol molecules (obstacles) are extremely likely to have contact for very low ϕ_0.

When studying any macroscopic system with a very large number of degrees of freedom, it is necessary to make an approximation and simulate a smaller model system. This introduces systematic errors called finite size effects. To explore the finite size effects, simulations with $N_{par} = 2000, 5000, 10000$ and varying N_{obs}/N_{par}, for a fixed $\phi = 0.3$, were conducted. In Fig. 4.21.a are shown the stacked final size distributions for $N_{obs}/N_{oar} = 1, 2$, where it can be seen that changing the number of particles does not affect the final distributions. This result is even more evident from Fig. 4.21.b, which shows that the final mean sizes statistically follow the same curve, independently of the system size. The simulated system represents a very small area in comparison to a real system, thus containing a small sample of the whole. However, this sample is shown to be representative of the general behaviour that a simulation with higher number of particles

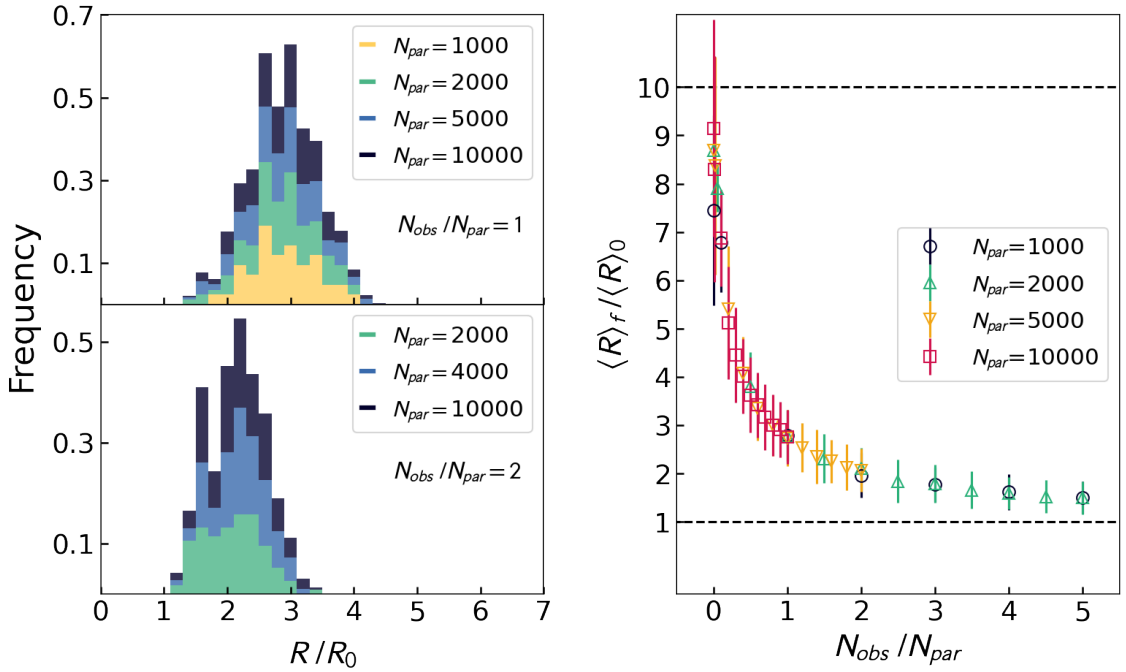

Figure 4.21: (**a**) Stacked size distributions for N_{obs}/N_{par} fractions of 1 (upper) and 2 (lower). The shape and mean of the distribution is governed by N_{obs}/N_{par}, independently of N_{par}. Although only $N_{obs}/N_{par} = 1, 2$ are exhibited, this analysis was also done for $N_{obs}/N_{par} = 0, 0.1, 3, 4, 5$. (**b**) $\langle R\rangle_f$ /$\langle R\rangle_0$ fractions in function of N_{obs}/N_{par} for different system sizes. The dashed lower dashed line represents the initial mean size while the upper represents the value corresponding to full sintering. It can be seen that the points in b statistically follow the same curve, evidencing that the system size does not significantly change the outcomes. For all figures, $\phi_0 = 0.3$.

would present.

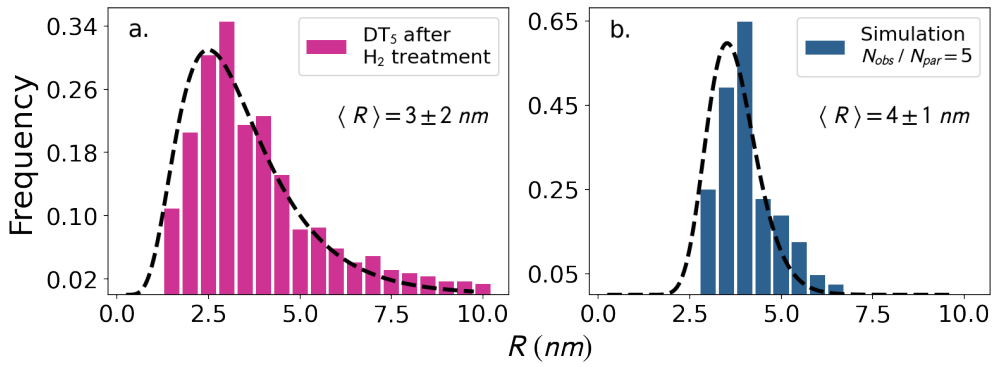

Figure 4.22: (a) Experimental size distribution of DT_5 sample after heating, obtained by TEM. (b) Final size distribution from simulation for $N_{obs}/N_{par} = 5$ and $\phi_0 = 0.3$. In the simulation the initial size distribution is homogeneous; all particles start with $R_0 = 2.5$ nm.

In conclusion, the proposed mechanism assumes that the dithiol molecules act as obstacles to prevent nanoparticles contact and subsequent coalescence, thus avoiding sintering. The numerical results demonstrate that this is a plausible mechanism, since particles coalescence is efficiently reduced for reasonable obstacles to particles ratios, as seen in Fig. 4.20. The dithiol molecules have sizes of $\sim 0.5nm$ and thus are not expected to represent a strong physical barrier for nanoparticles of more than 10x their size. However, with enough volume of dithiol molecules, they can decrease nanoparticle diffusion by locally raising the activation energy for migration. Comparison with experiments must be taken cautiously, since there are several simplifications to our model. For the experimental estimated value of $\phi \sim 0.3$, the model predicts that it would be necessary at least two times more obstacles than particles. From the dithiol to Cu mass ratio used to prepare the samples, it is known that the experimental N_{obs}/N_{par} is well above 2 before heating (could be as high as $\sim 10^3$). However, XPS analysis showed that a considerable fraction of dithiol breaks at high temperatures, altering this fraction. As Fig. 4.22 shows, the particle radius distributions of a simulation for $N_{obs}/N_{par} = 5$ and the TEM distribution for DT_5 after the treatment have similar behaviour, indicating that the particle growth is well described by the coalescence mechanism. As for the specific values of R, it have to be noted that the Cu nanoparticles already had a well defined size distribution before heating (Fig. 4.7.a), while the simulated particles started with an homogeneous distribution where $R_i = R_0 = 2.5\ nm$ for every i. In addition, the relation between λ and R (Eq. 4.5) is strictly phenomenological and should be thoroughly investigated to make a more realistic model. With this considerations, the results convincingly show that the model works as a mechanism to prevent sintering and can be regarded as a possible description of how impregnating an MgO surface with dithiol molecules prevents sintering of Cu nanoparticles.

Chapter 5

Conclusions and Perspectives

In this work a new method for preventing sintering of nanoparticles was presented and examined. It consists on the impregnation of the support surface with dithiol molecules, which successfully prevents sintering of Cu/MgO nanoparticles by acting as obstacles for nanoparticles diffusion. XRD results show that, after H_2 treatment under 300 °C, the Cu nanoparticles in the sample without dithiol have a 332% increase in mean diameter, while the samples with dithiol impregnation retain around the same mean size as the Cu nanoparticles as prepared. The *in situ* EXAFS results corroborates this trend, where the mean Cu nanoparticle size for the sample without dithiol is 175% bigger than for the other samples. The TEM images also show compelling evidence of sintering in the sample without dithiol after H_2 treatment at 300 ° C, and for the other samples, the TEM images indicate that sintering was prevented or at least substantially reduced. Therefore, three distinct experimental techniques have given a consistent trend that unequivocally indicates the method is effective in preventing sintering for the studied system. Furthermore, the use of XPS and *in situ* time-resolved XANES techniques have demonstrated that the method does not cause sulfur poisoning of the Cu nanoparticles. In special, the XPS measurements indicate the possibility of dithiol being strongly adsorbed at the support, as expected. A simple model in which the nanoparticles migrate through Brownian motion and have its diffusion hindered by randomly placed obstacles has been explored and shown to portrait a plausible mechanism whereby the method prevents sintering by coalescence. Monte Carlo simulations show that under reasonable fractions of obstacles to particles sintering is highly suppressed and that the diagram of nanoparticle growth as a function of the fraction of obstacles to particles and initial occupation fraction show discernible regimes, making it possible to estimate the parameter ranges that determine a sintering preventive system.

The sintering prevention method here presented can be applied to other systems, given

a thoughtful choice of the components. The study of different systems would give rich information on the limitations of the method. Further inquiry on the minimal required quantities of dithiol for an effective prevention are needed, as well as the amounts from which the nanoparticles become poisoned. For this purpose, a quantitative estimation of dithiol loss due to sulfonate formation under high temperatures is also needed. The dithiol amount thresholds can be more deeply investigated by refining the theoretical model through the use of experimentally obtained parameters and implementing more detailed relations to simulate nanoparticle diffusion. Also, analysis of the system under higher temperatures is valuable to explore the limiting temperatures where the method fails. Reactivity measurements must be made to investigate whether the method compromise catalytic activity.

References

[1] ABRÀMOFF, MICHAEL D, MAGALHÃES, PAULO J, RAM, SUNANDA J. Image processing with ImageJ. **Biophotonics international**, v. 11, n. 7, p. 36–42, 2004.

[2] AKHTAR, M KAMAL, LIPSCOMB, G GLENN, PRATSINIS, SOTIRIS E. Monte carlo simulation of particle coagulation and sintering. **Aerosol Science and Technology**, v. 21, n. 1, p. 83–93, 1994.

[3] ALIMOHAMMADI, MOZHGAN, FICHTHORN, KRISTEN A. Molecular dynamics simulation of the aggregation of titanium dioxide nanocrystals: preferential alignment. **Nano letters**, v. 9, n. 12, p. 4198–4203, 2009.

[4] ARGYLE, MORRIS D, BARTHOLOMEW, CALVIN H. Heterogeneous catalyst deactivation and regeneration: a review. **Catalysts**, v. 5, n. 1, p. 145–269, 2015.

[5] ASTRUC, DIDIER, LU, FENG, ARANZAES, JAIME RUIZ. Nanoparticles as recyclable catalysts: the frontier between homogeneous and heterogeneous catalysis. **Angewandte Chemie International Edition**, v. 44, n. 48, p. 7852–7872, 2005.

[6] BAGUS, PAUL S, ILTON, EUGENE S, NELIN, CONNIE J. The interpretation of XPS spectra: Insights into materials properties. **Surface Science Reports**, v. 68, n. 2, p. 273–304, 2013.

[7] BAIN, COLIN D, BIEBUYCK, HANS A, WHITESIDES, GEORGE M. Comparison of self-assembled monolayers on gold: coadsorption of thiols and disulfides. **Langmuir**, v. 5, n. 3, p. 723–727, 1989.

[8] BARTHOLOMEW, CALVIN H. Carbon deposition in steam reforming and methanation. **Catalysis Reviews Science and Engineering**, v. 24, n. 1, p. 67–112, 1982.

[9] BARTHOLOMEW, CALVIN H. Mechanisms of catalyst deactivation. **Applied Catalysis A: General**, v. 212, n. 1-2, p. 17–60, 2001.

[10] BARTHOLOMEW, CALVIN H, FARRAUTO, ROBERT J. **Fundamentals of industrial catalytic processes**: John Wiley & Sons, 2011.

[11] BARTHOLOMEW, CALVIN H, SORENSEN, WAYNE L. Sintering kinetics of silica- and alumina-supported nickel in hydrogen atmosphere. **Journal of Catalysis**, v. 81, n. 1, p. 131–141, 1983.

[12] BARTHOLOMEW, CH, AGRAWAL, PK, KATZER, JR. Sulfur poisoning of metals. In: ADVANCES IN CATALYSIS, v. 31, p. 135–242. Elsevier, 1982.

[13] BECK, DONALD D, CARR, CONSTANCE J. A study of thermal aging of ptal2o3 using temperature-programmed desorption spectroscopy. **Journal of Catalysis**, v. 110, n. 2, p. 285–297, 1988.

[14] BELL, ALEXIS T. The impact of nanoscience on heterogeneous catalysis. **Science**, v. 299, n. 5613, p. 1688–1691, 2003.

[15] BENSEBAA, FARID, ZHOU, YU, DESLANDES, YVES, KRUUS, ERIK, ELLIS, TOMAS H. XPS study of metal-sulfur bonds in metal-alkanethiolate materials. **Surface science**, v. 405, n. 1, p. L472–L476, 1998.

[16] BERNARDI, FABIANO, ALVES, MARIA CM, TRAVERSE, AGNES, SILVA, DAGOBERTO O, SCHEEREN, CARLA W, DUPONT, JAIRTON, MORAIS, JONDER. Monitoring atomic rearrangement in Pt_xPd_{1-x} (x= 1, 0.7, or 0.5) nanoparticles driven by reduction and sulfidation processes. **The Journal of Physical Chemistry C**, v. 113, n. 10, p. 3909–3916, 2009.

[17] BORCHERT, HOLGER, SHEVCHENKO, ELENA V, ROBERT, AYMERIC, MEKIS, IVO, KORNOWSKI, ANDREAS, GRÜBEL, GERHARD, WELLER, HORST. Determination of nanocrystal sizes: a comparison of TEM, SAXS, and XRD studies of highly monodisperse $CoPt_3$ particles. **Langmuir**, v. 21, n. 5, p. 1931–1936, 2005.

[18] BRAGG, WILLIAM HENRY, BRAGG, WILLIAM LAWRENCE, OTHERS, . The reflection of X-rays by crystals. **Proc. R. Soc. Lond. A**, v. 88, n. 605, p. 428–438, 1913.

[19] BUFFAT, PH, BOREL, JEAN PIERRE. Size effect on the melting temperature of gold particles. **Physical review A**, v. 13, n. 6, p. 2287, 1976.

[20] BUNKER, GRANT. **Introduction to XAFS: a practical guide to X-ray absorption fine structure spectroscopy**: Cambridge University Press, 2010.

[21] CALVIN, S, MILLER, MM, GOSWAMI, R, CHENG, S-F, MULVANEY, SP, WHITMAN, LJ, HARRIS, VG. Determination of crystallite size in a magnetic nanocomposite using extended X-ray absorption fine structure. **Journal of applied physics**, v. 94, n. 1, p. 778–783, 2003.

[22] CAMPBELL, CHARLES T, KOEL, BRUCE E. H_2S/Cu (111): A model study of sulfur poisoning of water-gas shift catalysts. **Surface science**, v. 183, n. 1-2, p. 100–112, 1987.

[23] CAMPBELL, CHARLES T, PARKER, STEPHEN C, STARR, DAVID E. The effect of size-dependent nanoparticle energetics on catalyst sintering. **Science**, v. 298, n. 5594, p. 811–814, 2002.

[24] CAMPELO, JUAN M, LUNA, DIEGO, LUQUE, RAFAEL, MARINAS, JOSE M, ROMERO, ANTONIO A. Sustainable preparation of supported metal nanoparticles and their applications in catalysis. **ChemSusChem: Chemistry & Sustainability Energy & Materials**, v. 2, n. 1, p. 18–45, 2009.

[25] CAO, ANMIN, LU, RONGWEN, VESER, GÖTZ. Stabilizing metal nanoparticles for heterogeneous catalysis. **Physical Chemistry Chemical Physics**, v. 12, n. 41, p. 13499–13510, 2010.

[26] CAO, ANMIN, VESER, GOETZ. Exceptional high-temperature stability through distillation-like self-stabilization in bimetallic nanoparticles. **Nature Materials**, v. 9, n. 1, p. 75–81, 2010.

[27] CARGNELLO, MATTEO, DOAN-NGUYEN, VICKY VT, GORDON, THOMAS R, DIAZ, ROSA E, STACH, ERIC A, GORTE, RAYMOND J, FORNASIERO, PAOLO, MURRAY, CHRISTOPHER B. Control of metal nanocrystal size reveals metal-support interface role for ceria catalysts. **Science**, v. 341, n. 6147, p. 771–773, 2013.

[28] CENTI, GABRIELE, PERATHONER, SIGLINDA, RAK, ZBIGNIEW S. Reduction of greenhouse gas emissions by catalytic processes. **Applied Catalysis B: Environmental**, v. 41, n. 1-2, p. 143–155, 2003.

[29] CEZAR, JULIO C, SOUZA-NETO, NARCIZO M, PIAMONTEZE, CíNTHIA, TAMURA, EDILSON, GARCIA, FLAVIO, CARVALHO, EDSON J,

NEUESCHWANDER, RÉGIS T, RAMOS, ALINE Y, TOLENTINO, HÉLIO CN, CANEIRO, ALBERTO, OTHERS, . Energy-dispersive x-ray absorption spectroscopy at lnls: investigation on strongly correlated metal oxides. **Journal of synchrotron radiation**, v. 17, n. 1, p. 93–102, 2010.

[30] CHALLA, SIVAKUMAR R, DELARIVA, ANDREW T, HANSEN, THOMAS W, HELVEG, STIG, SEHESTED, JENS, HANSEN, POUL L, GARZON, FERNANDO, DATYE, ABHAYA K. Relating rates of catalyst sintering to the disappearance of individual nanoparticles during Ostwald ripening. **Journal of the american chemical society**, v. 133, n. 51, p. 20672–20675, 2011.

[31] CHAPPERT, CLAUDE, FERT, ALBERT, VAN DAU, FRÉDÉRIC NGUYEN. The emergence of spin electronics in data storage. In: NANOSCIENCE AND TECHNOLOGY: A COLLECTION OF REVIEWS FROM NATURE JOURNALS, p. 147–157. World Scientific, 2010.

[32] CHEN, KY, COST, JR. Coalescence of helium bubbles in aluminum. **Journal of Nuclear Materials**, v. 52, n. 1, p. 59–74, 1974.

[33] CHERNYSHEV, VICTOR M, ASTAKHOV, ALEXANDER V, CHIKUNOV, ILYA E, TYURIN, ROMAN V, EREMIN, DMITRY B, RANNY, GLEB S, KHRUSTALEV, VICTOR N, ANANIKOV, VALENTINE P. Pd and Pt catalyst poisoning in the study of reaction mechanisms: what does the mercury test mean for catalysis? **ACS Catalysis**, v. 9, n. 4, p. 2984–2995, 2019.

[34] CHONG, KEN P. Nanoscience and engineering in mechanics and materials. **Journal of Physics and Chemistry of Solids**, v. 65, n. 8-9, p. 1501–1506, 2004.

[35] CULLITY, BERNARD DENNIS, STOCK, STUART R. **Elements of X-ray Diffraction**. 2.ed.: Reading, Addison-Wesley Publishing Company, Inc., 1978.

[36] DE BROGLIE, L. Research on the theory of quanta. In: ANNALES DE PHYSIQUE, v. 10, p. 22–128, 1925.

[37] DE VOS, DIRK E, DAMS, MIEKE, SELS, BERT F, JACOBS, PIERRE A. Ordered mesoporous and microporous molecular sieves functionalized with transition metal complexes as catalysts for selective organic transformations. **Chemical Reviews**, v. 102, n. 10, p. 3615–3640, 2002.

[38] VRIES, JOHANNES GDE , JACKSON, S DAVID. Homogeneous and heterogeneous catalysis in industry. **Catalysis Science & Technology**, v. 2, n. 10, p. 2009–2009, 2012.

[39] DEL ANGEL, G, BONILLA, A, PENA, Y, NAVARRETE, J, FIERRO, JLG, ACOSTA, DR. Effect of lanthanum on the catalytic properties of PtSn/γ-Al_2o_3 bimetallic catalysts prepared by successive impregnation and controlled surface reaction. **Journal of Catalysis**, v. 219, n. 1, p. 63–73, 2003.

[40] DELLA MEA, GUILHERME B, MATTE, LíVIA P, THILL, ALISSON S, LOBATO, FRANCIELLI O, BENVENUTTI, EDILSON V, ARENAS, LELIZ T, JÜRGENSEN, ASTRID, HERGENRÖDER, ROLAND, POLETTO, FERNANDA, BERNARDI, FABIANO. Tuning the oxygen vacancy population of cerium oxide (ceo2- x, 0¡ x¡ 0.5) nanoparticles. **Applied Surface Science**, v. 422, p. 1102–1112, 2017.

[41] DELMON, B, ERTL, G, KNÖZINGER, H, WEITKAMP, J. **Handbook of heterogeneous catalysis**, v. 1: Wiley-VCH, 1997.

[42] DELMON, BERNARD. **Catalyst Deactivation 1980: International Symposium Proceedings: International Symposium Proceedings**: Elsevier, 2000.

[43] DEROSA, MARIA C, MONREAL, CARLOS, SCHNITZER, MORRIS, WALSH, RYAN, SULTAN, YASIR. Nanotechnology in fertilizers. **Nature nanotechnology**, v. 5, n. 2, p. 91–91, 2010.

[44] DEVROYE, LUC. Nonuniform random variate generation. **Handbooks in operations research and management science**, v. 13, p. 83–121, 2006.

[45] DING, LIFENG, DAVIDCHACK, RUSLAN L, PAN, JINGZHE. A molecular dynamics study of sintering between nanoparticles. **Computational Materials Science**, v. 45, n. 2, p. 247–256, 2009.

[46] DING, Y, MAJETICH, SA, KIM, J, BARMAK, K, ROLLINS, H, SIDES, P. Sintering prevention and phase transformation of FePt nanoparticles. **Journal of magnetism and magnetic materials**, v. 284, p. 336–341, 2004.

[47] DUNLEAVY, JK. Sulfur as a catalyst poison. **Platinum Metals Review**, v. 50, n. 2, p. 110, 2006.

[48] DUPAS, CLAIRE, LAHMANI, MARCEL. **Nanoscience: Nanotechnologies and nanophysics**: Berlin, Springer Science & Business Media, 2007.

[49] ECKERT, MICHAEL. Max von laue and the discovery of X-ray diffraction in 1912. **Annalen der Physik**, v. 524, n. 5, p. A83–A85, 2012.

[50] EINSTEIN, ALBERT. The photoelectric effect. **Ann. Phys**, v. 17, n. 132, p. 4, 1905.

[51] EREKSON, EREK J, BARTHOLOMRW, CALVIN H. Sulfur poisoning of nickel methanation catalysts: Ii. effects of h2s concentration, co and h2o partial pressures and temperature on reactivation rates. **Applied Catalysis**, v. 5, n. 3, p. 323–336, 1983.

[52] ERHARDT, DAVID. Not-so-new technology. **Nature materials**, v. 2, n. 8, p. 509–510, 2003.

[53] ERTL, GERHARD, KNÖZINGER, HELMUT, WEITKAMP, JENS. **Preparation of solid catalysts**: John Wiley & Sons, 2008.

[54] ESA, . Catalysts or making it happen, september 20th of 2018.

[55] EUZEN, PATRICK, LE GAL, JEAN-HERVÉ, REBOURS, BERNADETTE, MARTIN, GÉRARD. Deactivation of palladium catalyst in catalytic combustion of methane. **Catalysis today**, v. 47, n. 1-4, p. 19–27, 1999.

[56] FANTAUZZI, MARZIA, ELSENER, BERNHARD, ATZEI, DAVIDE, RIGOLDI, AMERICO, ROSSI, ANTONELLA. Exploiting XPS for the identification of sulfides and polysulfides. **RSC advances**, v. 5, n. 93, p. 75953–75963, 2015.

[57] FERNÁNDEZ-GARCíA, MARCOS. XANES analysis of catalytic systems under reaction conditions. **Catalysis Reviews**, v. 44, n. 1, p. 59–121, 2002.

[58] FERRARI, MAURO. Cancer nanotechnology: opportunities and challenges. **Nature reviews cancer**, v. 5, n. 3, p. 161–171, 2005.

[59] FEYNMAN, RICHARD P, OTHERS, . There's plenty of room at the bottom. **California Institute of Technology, Engineering and Science magazine**, 1960.

[60] FIGUEIREDO, WALLACE T, DELLA MEA, GUILHERME B, SEGALA, MAXIMILIANO, BAPTISTA, DANIEL L, ESCUDERO, CARLOS, PÉREZ-DIESTE, VIRGINIA, BERNARDI, FABIANO. Understanding the strong metal-support interaction (SMSI) effect in Cu_x Ni_{1-x}/CeO_2 ($0<x<1$) nanoparticles for enhanced catalysis. **ACS Applied Nano Materials**, v. 2, n. 4, p. 2559–2573, 2019.

[61] FIGUEROA, SJA, MAURICIO, JC, MURARI, J, BENIZ, DB, PITON, JR, SLEPICKA, HH, SOUSA, M FALCÃODE , ESPíNDOLA, AM, LEVINSKY, APS. Upgrades to the xafs2 beamline control system and to the endstation at the lnls. In: JOURNAL OF PHYSICS: CONFERENCE SERIES, v. 712. IOP Publishing, p. 012022, 2016.

[62] FOMIN, VLADIMIR M. **Physics of Quantum Rings**: Londres, Springer Science & Business Media, 2013.

[63] FORZATTI, PIO, LIETTI, LUCA. Catalyst deactivation. **Catalysis today**, v. 52, n. 2-3, p. 165–181, 1999.

[64] FRANK, FC, READ JR, WT. Multiplication processes for slow moving dislocations. **Physical Review**, v. 79, n. 4, p. 722, 1950.

[65] FROMENT, GF, DELMON, B. **Catalyst Deactivation 1994**: Elsevier, 1994.

[66] FULTZ, BRENT, HOWE, JAMES M. **Transmission electron microscopy and diffractometry of materials**: Springer Science & Business Media, 2012.

[67] GABALDON, JOHN P, BORE, MANGESH, DATYE, ABHYA K. Mesoporous silica supports for improved thermal stability in supported Au catalysts. **Topics in Catalysis**, v. 44, n. 1-2, p. 253–262, 2007.

[68] GAO, TAO, HOU, SINGYUK, HUYNH, KHUE, WANG, FEI, EIDSON, NICO, FAN, XIULIN, HAN, FUDONG, LUO, CHAO, MAO, MINGLEI, LI, XIAOGANG, OTHERS, . Existence of solid electrolyte interphase in Mg batteries: Mg/S chemistry as an example. **ACS applied materials & interfaces**, v. 10, n. 17, p. 14767–14776, 2018.

[69] GAO, TAO, HOU, SINGYUK, WANG, FEI, MA, ZHAOHUI, LI, XIAOGANG, XU, KANG, WANG, CHUNSHENG. Reversible S^0/MgS_x redox chemistry in a $MgTFSI_2/MgCl_2$/DME electrolyte for rechargeable Mg/S batteries. **Angewandte Chemie**, v. 129, n. 43, p. 13711–13715, 2017.

[70] GAO, TAO, NOKED, MALACHI, PEARSE, ALEX J, GILLETTE, ELEANOR, FAN, XIULIN, ZHU, YUJIE, LUO, CHAO, SUO, LIUMIN, SCHROEDER, MARSHALL A, XU, KANG, OTHERS, . Enhancing the reversibility of Mg/S battery chemistry through Li^+ mediation. **Journal of the American Chemical Society**, v. 137, n. 38, p. 12388–12393, 2015.

[71] GAWANDE, MANOJ B, GOSWAMI, ANANDARUP, FELPIN, FRANÇOIS-XAVIER, ASEFA, TEWODROS, HUANG, XIAOXI, SILVA, RAFAEL, ZOU, XIAOXIN, ZBORIL, RADEK, VARMA, RAJENDER S. Cu and Cu-based nanoparticles: synthesis and applications in catalysis. **Chemical reviews**, v. 116, n. 6, p. 3722–3811, 2016.

[72] GRUBER, EE. Calculated size distributions for gas bubble migration and coalescence in solids. **Journal of Applied Physics**, v. 38, n. 1, p. 243–250, 1967.

[73] GRÜNERT, WOLFGANG, KLEMENTIEV, KONSTANTIN. X-ray absorption spectroscopy principles and practical use in materials analysis. **Physical Sciences Reviews**, v. 1, n. ahead-of-print, 2020.

[74] HANSEN, THOMAS WILLUM. Sintering and particle dynamics in supported metal catalysts. 2006.

[75] HARRIS, PJF. Growth and structure of supported metal catalyst particles. **International materials reviews**, v. 40, n. 3, p. 97–115, 1995.

[76] HARUTA, MASATAKE. Size-and support-dependency in the catalysis of gold. **Catalysis today**, v. 36, n. 1, p. 153–166, 1997.

[77] HAVLIN, SHLOMO, BEN-AVRAHAM, DANIEL. Diffusion in disordered media. **Advances in physics**, v. 36, n. 6, p. 695–798, 1987.

[78] HAYEZ, V, FRANQUET, A, HUBIN, A, TERRYN, H. XPS study of the atmospheric corrosion of copper alloys of archaeological interest. **Surface and Interface Analysis: An International Journal devoted to the development and application of techniques for the analysis of surfaces, interfaces and thin films**, v. 36, n. 8, p. 876–879, 2004.

[79] HOCHELLA JR, MICHAEL F. Nanoscience and technology: the next revolution in the earth sciences. **Earth and Planetary Science Letters**, v. 203, n. 2, p. 593–605, 2002.

[80] HOEHNE, KLAUS, SIZMANN, R. Volume and surface self-diffusion measurements on copper by thermal surface smoothing. **physica status solidi (a)**, v. 5, n. 3, p. 577–589, 1971.

[81] HUANG, WJ, SUN, R, TAO, J, MENARD, LD, NUZZO, RG, ZUO, JM. Coordination-dependent surface atomic contraction in nanocrystals revealed by coherent diffraction. **Nature materials**, v. 7, n. 4, p. 308–313, 2008.

[82] JACOBS, GARY, GHADIALI, FIROZ, PISANU, ADRIANA, PADRO, CRISTINA L, BORGNA, ARMANDO, ALVAREZ, WALTER E, RESASCO, DANIEL E. Increased sulfur tolerance of Pt/KL catalysts prepared by vapor-phase impregnation and containing a tm promoter. **Journal of Catalysis**, v. 191, n. 1, p. 116–127, 2000.

[83] JENSEN, IJT, DIPLAS, S, LøVVIK, OM, WATTS, J, HINDER, S, SCHREUDERS, H, DAM, B. X-ray photoelectron spectroscopy study of MgH_2 thin films grown by reactive sputtering. **Surface and Interface Analysis**, v. 42, n. 6-7, p. 1140–1143, 2010.

[84] JENTYS, ANDREAS. Estimation of mean size and shape of small metal particles by EXAFS. **Physical Chemistry Chemical Physics**, v. 1, n. 17, p. 4059–4063, 1999.

[85] JEON, TAE-YEOL, YOO, SUNG JONG, CHO, YONG-HUN, KANG, SOON HYUNG, SUNG, YUNG-EUN. Effect of de-alloying of Pt-Ni bimetallic nanoparticles on the oxygen reduction reaction. **Electrochemistry communications**, v. 12, n. 12, p. 1796–1799, 2010.

[86] JIA, QIANG, ZOU, GUISHENG, WANG, WENGAN, REN, HUI, ZHANG, HONGQIANG, DENG, ZHONGYANG, FENG, BIN, LIU, LEI. Sintering mechanism of a supersaturated Ag-Cu nanoalloy film for power electronic packaging. **ACS Applied Materials & Interfaces**, v. 12, n. 14, p. 16743–16752, 2020.

[87] JOO, SANG HOON, PARK, JEONG YOUNG, TSUNG, CHIA-KUANG, YAMADA, YUSUKE, YANG, PEIDONG, SOMORJAI, GABOR A. Thermally stable Pt/mesoporous silica core-shell nanocatalysts for high-temperature reactions. **Nature materials**, v. 8, n. 2, p. 126, 2009.

[88] JOSE-YACAMAN, M, GUTIERREZ-WING, C, MIKI, M, YANG, D-Q, PIYAKIS, KN, SACHER, E. Surface diffusion and coalescence of mobile metal nanoparticles. **The Journal of Physical Chemistry B**, v. 109, n. 19, p. 9703–9711, 2005.

[89] JOYNER, RICHARD W, PENDRY, JOHN B, SALDIN, DELANO K, TENNISON, STEPHEN R. Metal-support interactions in heterogeneous catalysis. **Surface science**, v. 138, n. 1, p. 84–94, 1984.

[90] JU, YIWEN, LU, SHUANGFANG, SUN, YAN, TAN, FENGQI, WANG, GUOCHANG, HAN, KU, BAO, YUAN, LI, QINGGUANG. Nano-geology and unconventional oil and gas. **Acta Geologica Sinica-English Edition**, v. 89, n. s1, p. 192–193, 2015.

[91] JU, YW, SUN, YAN, WAN, QUAN, LU, SHUANG-FANG, HE, HONG-PING, WU, JIAN-GUANG, ZHANG, WEN-JING, WANG, GUO-CHANG, HUANG, CHENG. Nanogeology: A revolutionary challenge in geosciences. **Bulletin of Mineralogy, Petrology and Geochemistry**, v. 35, n. 1, p. 1–20, 2016.

[92] JULKAPLI, NURHIDAYATULLAILI MUHD, BAGHERI, SAMIRA. Magnesium oxide as a heterogeneous catalyst support. **Reviews in Inorganic Chemistry**, v. 36, n. 1, p. 1–41, 2016.

[93] KALAKKAD, DINESH S, SHROFF, MEHUL D, KÖHLER, STEVE, JACKSON, NANCY, DATYE, AK. Attrition of precipitated iron Fischer-Tropsch catalysts. **Applied Catalysis A: General**, v. 133, n. 2, p. 335–350, 1995.

[94] KALANUR, SHANKARA S, SEO, HYUNGTAK. Synthesis of Cu_xS thin films with tunable localized surface plasmon resonances. **ChemistrySelect**, v. 3, n. 21, p. 5920–5926, 2018.

[95] KART, HH, YILDIRIM, H, KART, S OZDEMIR, ÇAĞIN, T. Physical properties of Cu nanoparticles: A molecular dynamics study. **Materials Chemistry and Physics**, v. 147, n. 1-2, p. 204–212, 2014.

[96] KAUSHAL, JYOTI, MEHANDIA, SEEMA, SINGH, GURSHARAN, RAINA, ARUN, ARYA, SHAILENDRA KUMAR. Catalase enzyme: Application in bioremediation and food industry. **Biocatalysis and agricultural biotechnology**, v. 16, p. 192–199, 2018.

[97] KEIPER, ADAM. The nanotechnology revolution. **The New Atlantis**, , n. 2, p. 17–34, 2003.

[98] KHAIRALLAH, FARES, GLISENTI, ANTONELLA. XPS study of MgO nanopowders obtained by different preparation procedures. **Surface Science Spectra**, v. 13, n. 1, p. 58–71, 2006.

[99] KHAIRALLAH, FARES, GLISENTI, ANTONELLA, NATILE, MARTA MARIA, GALENDA, ALESSANDRO. ZnO/MgO nanocomposites by wet impregnation: An XPS study. **Surface Science Spectra**, v. 17, n. 1, p. 76–86, 2010.

[100] KHAWAJA, AYAZ MAHMOOD. The legacy of nanotechnology: revolution and prospects in neurosurgery. **International Journal of Surgery**, v. 9, n. 8, p. 608–614, 2011.

[101] KIM, JAE Y, RODRIGUEZ, JOSÉ A, HANSON, JONATHAN C, FRENKEL, ANATOLY I, LEE, PETER L. Reduction of CuO and Cu_2O with H_2: H embedding and kinetic effects in the formation of suboxides. **Journal of the American Chemical Society**, v. 125, n. 35, p. 10684–10692, 2003.

[102] KONINGSBERGER, DC, PRINS, ROELOF. **X-ray absorption: principles, applications, techniques of EXAFS, SEXAFS, and XANES**, v. 60: John Wiley and Sons, 1988.

[103] KRIL, CE, BIRRINGER, RAINER. Estimating grain-size distributions in nanocrystalline materials from X-ray diffraction profile analysis. **Philosophical Magazine A**, v. 77, n. 3, p. 621–640, 1998.

[104] KRYLOVA, VALENTINA, ANDRULEVIČIUS, MINDAUGAS. Optical, XPS and XRD studies of semiconducting copper sulfide layers on a polyamide film. **International Journal of Photoenergy**, v. 2009, 2009.

[105] KWOK, RWM. XPS peak software. version 4.1., 2000.

[106] LAIBINIS, PAUL E, WHITESIDES, GEORGE M, ALLARA, DAVID L, TAO, YU TAI, PARIKH, ATUL N, NUZZO, RALPH G. Comparison of the structures and wetting properties of self-assembled monolayers of n-alkanethiols on the coinage metal surfaces, copper, silver, and gold. **Journal of the American Chemical Society**, v. 113, n. 19, p. 7152–7167, 1991.

[107] LAKATOS-LINDENBERG, KATJA, SHULER, KURT E. Random walks with nonnearest neighbor transitions. i. analytic 1-d theory for next-nearest neighbor and exponentially distributed steps. **Journal of Mathematical Physics**, v. 12, n. 4, p. 633–652, 1971.

[108] LANGE, JEAN-PAUL. Renewable feedstocks: the problem of catalyst deactivation and its mitigation. **Angewandte Chemie International Edition**, v. 54, n. 45, p. 13186–13197, 2015.

[109] LASHOF, DANIEL A, AHUJA, DILIP R. Relative contributions of greenhouse gas emissions to global warming. **Nature**, v. 344, n. 6266, p. 529, 1990.

[110] LEARNING, LUMEN. **Factors that affect chemical equilibrium**. 2021, Site: `https://courses.lumenlearning.com/boundless-chemistry/chapter/factors-that-affect-chemical-equilibrium/`. Acessed in: january 15th of 2021.

[111] LEE, PA, PENDRY, JB. Theory of the extended X-ray absorption fine structure. **Physical Review B**, v. 11, n. 8, p. 2795, 1975.

[112] LEE, SIWON, SEO, JONGSU, JUNG, WOOCHUL. Sintering-resistant Pt@CeO_2 nanoparticles for high-temperature oxidation catalysis. **Nanoscale**, v. 8, n. 19, p. 10219–10228, 2016.

[113] LI, DONGSHENG, NIELSEN, MICHAEL H, LEE, JONATHAN RI, FRANDSEN, CATHRINE, BANFIELD, JILLIAN F, DE YOREO, JAMES J. Direction-specific interactions control crystal growth by oriented attachment. **Science**, v. 336, n. 6084, p. 1014–1018, 2012.

[114] LIEBER, CHARLES M. Semiconductor nanowires: A platform for nanoscience and nanotechnology. **Mrs Bulletin**, v. 36, n. 12, p. 1052–1063, 2011.

[115] LIFSHITZ, ILYA M, SLYOZOV, VITALY V. The kinetics of precipitation from supersaturated solid solutions. **Journal of physics and chemistry of solids**, v. 19, n. 1-2, p. 35–50, 1961.

[116] LIMOGE, Y, BOCQUET, JL. Monte Carlo simulation in diffusion studies: time scale problems. **Acta metallurgica**, v. 36, n. 7, p. 1717–1722, 1988.

[117] LINDSAY, STUART. **Introduction to nanoscience**: New York, Oxford University Press, 2010.

[118] LIU, JIA, JI, QINGMIN, IMAI, TSUBASA, ARIGA, KATSUHIKO, ABE, HIDEKI. Sintering-resistant nanoparticles in wide-mouthed compartments for sustained catalytic performance. **Scientific Reports**, v. 7, p. 41773, 2017.

[119] LIU, RUIZENG, LIU, DIANWEN, LI, JIALEI, LI, JIANMIN, LIU, ZHICHENG, JIA, XIAODONG, YANG, SHENGWANG, LI, JIANGLI, NING, SHUAI. Sulfidization mechanism in malachite flotation: A heterogeneous solid-liquid reaction that yields cuxsy phases grown on malachite. **Minerals Engineering**, v. 154, p. 106420, 2020.

[120] LYTLE, FW, SAYERS, DE, STERN, EA. Extended X-ray-absorption fine-structure technique. ii. experimental practice and selected results. **Physical Review B**, v. 11, n. 12, p. 4825, 1975.

[121] MARELLA, RAVI KUMAR, NEELI, CHINNA KRISHNA PRASAD, KAMARAJU, SEETHA RAMA RAO, BURRI, DAVID RAJU. Highly active cu/mgo catalysts

for selective dehydrogenation of benzyl alcohol into benzaldehyde using neither O_2 nor H_2 acceptor. **Catalysis Science & Technology**, v. 2, n. 9, p. 1833–1838, 2012.

[122] MATTE, LíVIA P, KILIAN, ALEX S, LUZA, LEANDRO, ALVES, MARIA CM, MORAIS, JONDER, BAPTISTA, DANIEL L, DUPONT, JAIRTON, BERNARDI, FABIANO. Influence of the CeO_2 support on the reduction properties of Cu/Ceo_2 and Ni/CeO_2 nanoparticles. **The Journal of Physical Chemistry C**, v. 119, n. 47, p. 26459–26470, 2015.

[123] MAXWELL, IE, NABER, JE. New and improved catalytic processes for clean fuels. **Catalysis letters**, v. 12, n. 1-3, p. 105–115, 1992.

[124] MCNAUGHT, ALAN D, WILKINSON, ANDREW, OTHERS, . **Compendium of chemical terminology**, v. 1669: Blackwell Science Oxford, 1997.

[125] MCWILLIAMS, ANDREW. The maturing nanotechnology market: products and applications. **BCC Research, NAN031G**, 2016.

[126] MIRKIN, CHAD A. The beginning of a small revolution. **Small**, v. 1, n. 1, p. 14–16, 2005.

[127] MOM, RIK VALENTIJN. **Imaging complex model catalysts in action: From surface science towards industrial practice using high-pressure scanning tunneling microscopy**. 2017. Tese de Doutoramento – Leiden University.

[128] MORGAN, NEAL, WELLS, CLIVE, KRAFT, MARKUS, WAGNER, WOLFGANG. Modelling nanoparticle dynamics: coagulation, sintering, particle inception and surface growth. **Combustion Theory and Modelling**, v. 9, n. 3, p. 449–461, 2005.

[129] MOULIJN, JACOB A, VAN DIEPEN, AE, KAPTEIJN, FREEK. Catalyst deactivation: is it predictable?: What to do? **Applied Catalysis A: General**, v. 212, n. 1-2, p. 3–16, 2001.

[130] NAGARAJA, BM, PADMASRI, AH, RAJU, B DAVID, RAO, KS RAMA. Vapor phase selective hydrogenation of furfural to furfuryl alcohol over Cu–MgO coprecipitated catalysts. **Journal of Molecular Catalysis A: Chemical**, v. 265, n. 1-2, p. 90–97, 2007.

[131] NAVALÓN, SERGIO, GARCíA, H. Nanoparticles for catalysis. **Nanomaterials**, v. 6, n. 123, 2016.

[132] NEWMAN, M, BARKEMA, G. **Monte Carlo methods in statistical physics**, v. 24: Oxford University Press: New York, USA, 1999.

[133] PAN, XIULIAN, FAN, ZHONGLI, CHEN, WEI, DING, YUNJIE, LUO, HONGYUAN, BAO, XINHE. Enhanced ethanol production inside carbon-nanotube reactors containing catalytic particles. **Nature materials**, v. 6, n. 7, p. 507, 2007.

[134] PARK, JUNG-NAM, FORMAN, ARNOLD J, TANG, WEI, CHENG, JIHONG, HU, YONG-SHENG, LIN, HONGFEI, MCFARLAND, ERIC W. Highly active and sinter-resistant pd-nanoparticle catalysts encapsulated in silica. **Small**, v. 4, n. 10, p. 1694–1697, 2008.

[135] PARK, KINAM. Nanotechnology: What it can do for drug delivery. **Journal of controlled release: official journal of the Controlled Release Society**, v. 120, n. 1-2, p. 1, 2007.

[136] PARKS, GD, SCHAFFER, AM, DREILING, MJ, SHIBLOM, CM. Surface studies of the interaction of nickel and antimony on cracking catalysts. **Am. Chem. Soc., Div. Pet. Chem., Prepr.;(United States)**, v. 25, n. CONF-800303-, 1980.

[137] PARREIRA, P, LAVAREDA, G, AMARAL, A, DO REGO, AM BOTELHO, CONDE, O, VALENTE, J, NUNES, F, DE CARVALHO, C NUNES. Transparent p-type Cu_xS thin films. **Journal of Alloys and Compounds**, v. 509, n. 16, p. 5099–5104, 2011.

[138] PECHARSKY, VITALIJ, ZAVALIJ, PETER. **Fundamentals of powder diffraction and structural characterization of materials**: Springer Science & Business Media, 2008.

[139] PENG, YUE, LI, JUNHUA, CHEN, LIANG, CHEN, JINGHUAN, HAN, JIAN, ZHANG, HE, HAN1, WEI. Alkali metal poisoning of a CeO_2-WO_3 catalyst used in the selective catalytic reduction of NO_x with NH_3: An experimental and theoretical study. **Environmental science & technology**, v. 46, n. 5, p. 2864–2869, 2012.

[140] PENN, R LEE, BANFIELD, JILLIAN F. Imperfect oriented attachment: dislocation generation in defect-free nanocrystals. **Science**, v. 281, n. 5379, p. 969–971, 1998.

[141] PETERSON, CHRISTINE. **Molecular nanotechnology: the next industrial revolution**: Palo Alto, Foresight Institute. January, 2000.

[142] PIDGEON, N, PORRITT, J, RYAN, J, SEATON, A, TENDLER, S, WELLAND, M, WHATMORE, R. Nanoscience and nanotechnologies: opportunities and uncertainties. **The Royal Society, The Royal Academy of Engineering**, v. 29, n. 07, p. 2004, 2004.

[143] PIKE, JENNA, CHAN, SIU-WAI, ZHANG, FENG, WANG, XIANQIN, HANSON, JONATHAN. Formation of stable cu2o from reduction of cuo nanoparticles. **Applied Catalysis A: General**, v. 303, n. 2, p. 273–277, 2006.

[144] PLESSOW, PHILIPP N, ABILD-PEDERSEN, FRANK. Sintering of pt nanoparticles via volatile pto2: simulation and comparison with experiments. **ACS Catalysis**, v. 6, n. 10, p. 7098–7108, 2016.

[145] PONCELET, GEORGES, MARTENS, J, DELMON, B, GRANGE, P, JACOBS, PA. **Preparation of catalysts VI: scientific bases for the preparation of heterogeneous catalysts**: Elsevier, 1995.

[146] QIU, PENGFEI, ZHU, YAQIN, QIN, YUTING, SHI, XUN, CHEN, LIDONG. Electrical and thermal transports of binary copper sulfides Cu_xS with x from 1.8 to 1.96. **APL Materials**, v. 4, n. 10, p. 104805, 2016.

[147] QIU, SONGBAI, ZHANG, XUE, LIU, QIYING, WANG, TIEJUN, ZHANG, QI, MA, LONGLONG. A simple method to prepare highly active and dispersed Ni/MCM-41 catalysts by co-impregnation. **Catalysis Communications**, v. 42, p. 73–78, 2013.

[148] RATKE, LORENZ, VOORHEES, PETER W. **Growth and coarsening: Ostwald ripening in material processing**: Springer Science & Business Media, 2013.

[149] RAVEL, BRUCE, NEWVILLE, MATHENA. ATHENA, ARTEMIS, HEPHAESTUS: data analysis for X-ray absorption spectroscopy using IFEFFIT. **Journal of synchrotron radiation**, v. 12, n. 4, p. 537–541, 2005.

[150] RAZA, MOHSIN. **Oxygen vacancy stabilized zirconia (OVSZ); synthesis and properties**. 3 2017. Tese de Doutoramento – Université de Mons, Chimie des Interactions Plasma-Surface (ChIPS).

[151] REHR, JJ, ALBERS, RC. Scattering-matrix formulation of curved-wave multiple-scattering theory: Application to x-ray-absorption fine structure. **Physical Review B**, v. 41, n. 12, p. 8139, 1990.

[152] REICHL, LINDA E. **A modern course in statistical physics**: American Association of Physics Teachers, 1999.

[153] REITZ, TL, LEE, PL, CZAPLEWSKI, KF, LANG, JC, POPP, KE, KUNG, HH. Time-resolved XANES investigation of CuO/ZnO in the oxidative methanol reforming reaction. **Journal of catalysis**, v. 199, n. 2, p. 193–201, 2001.

[154] RIETVELD, HAM. A profile refinement method for nuclear and magnetic structures. **Journal of applied Crystallography**, v. 2, n. 2, p. 65–71, 1969.

[155] RODRIGUEZ, JA, LIU, P, WANG, X, WEN, W, HANSON, J, HRBEK, J, PÉREZ, M, EVANS, J. Water-gas shift activity of Cu surfaces and Cu nanoparticles supported on metal oxides. **Catalysis today**, v. 143, n. 1-2, p. 45–50, 2009.

[156] RODRIGUEZ, JOSÉ A, KIM, JAE Y, HANSON, JONATHAN C, PÉREZ, MANUEL, FRENKEL, ANATOLY I. Reduction of CuO in H_2: in situ time-resolved XRD studies. **Catalysis Letters**, v. 85, n. 3-4, p. 247–254, 2003.

[157] RODRIGUEZ-CARVAJAL, J. Fullprof: a program for Rietveld refinement and pattern matching analysis. In: SATELLITE MEETING ON POWDER DIFFRACTION OF THE XV CONGRESS OF THE IUCR, v. 127. 1990.

[158] RUCKENSTEIN, E, PULVERMACHER, B. Growth kinetics and the size distributions of supported metal crystallites. **Journal of Catalysis**, v. 29, n. 2, p. 224–245, 1973.

[159] RUSKA, ERNST. The development of the electron microscope and of electron microscopy. **Bioscience reports**, v. 7, n. 8, p. 607–629, 1987.

[160] SADEQZADEH, M, CHAMBREY, S, PICHÉ, S, FONGARLAND, P, LUCK, F, CURULLA-FERRÉ, D, SCHWEICH, D, BOUSQUET, J, KHODAKOV, AY. Deactivation of a Co/Al_2O_3 Fischer–Tropsch catalyst by water-induced sintering in slurry reactor: Modeling and experimental investigations. **Catalysis today**, v. 215, p. 52–59, 2013.

[161] SANDER, MARKUS, WEST, RICHARD H, CELNIK, MATTHEW S, KRAFT, MARKUS. A detailed model for the sintering of polydispersed nanoparticle agglomerates. **Aerosol Science and Technology**, v. 43, n. 10, p. 978–989, 2009.

[162] SATTERTHWAITE, DAVID. Cities' contribution to global warming: notes on the allocation of greenhouse gas emissions. **Environment and urbanization**, v. 20, n. 2, p. 539–549, 2008.

[163] SAXTON, MICHAEL J. Anomalous diffusion due to obstacles: a Monte Carlo study. **Biophysical journal**, v. 66, n. 2, p. 394–401, 1994.

[164] SAXTON, MICHAEL J. Anomalous subdiffusion in fluorescence photobleaching recovery: a Monte Carlo study. **Biophysical journal**, v. 81, n. 4, p. 2226–2240, 2001.

[165] SAYERS, DALE E, STERN, EDWARD A, LYTLE, FARREL W. New technique for investigating noncrystalline structures: Fourier analysis of the extended X-ray absorption fine structure. **Physical review letters**, v. 27, n. 18, p. 1204, 1971.

[166] SCHNOHR, CLAUDIA S, RIDGWAY, MARK C. Introduction to X-ray absorption spectroscopy. In: X-RAY ABSORPTION SPECTROSCOPY OF SEMICONDUCTORS, p. 1–26. Springer, 2015.

[167] SCHWIND, M, ÅGREN, JOHN. A random walk approach to Ostwald ripening. **Acta materialia**, v. 49, n. 18, p. 3821–3828, 2001.

[168] SHEN, MEIQING, ZHANG, YUN, WANG, JIANQIANG, WANG, CHEN, WANG, JUN. Nature of SO_3 poisoning on Cu/SAPO-34 SCR catalysts. **Journal of catalysis**, v. 358, p. 277–286, 2018.

[169] SHIRLEY, DAVE A. High-resolution X-ray photoemission spectrum of the valence bands of gold. **Physical Review B**, v. 5, n. 12, p. 4709, 1972.

[170] SHTYKA, OLEKSANDR, CIESIELSKI, RADOSLAW, KITSYUK, EVGENY, SAVITSKY, ANDREY, MANIECKI, TOMASZ. The influence of the size of metal particles on the catalytic activity of Ni and Cu-supported catalysts in methanol reforming reaction. **Reaction Kinetics, Mechanisms and Catalysis**, v. 129, n. 1, p. 219–233, 2020.

[171] SIMONSEN, SøREN BREDMOSE, CHORKENDORFF, IB, DAHL, SøREN, SKOGLUNDH, MAGNUS, SEHESTED, JENS, HELVEG, STIG. Ostwald ripening in a Pt/SiO_2 model catalyst studied by in situ TEM. **Journal of catalysis**, v. 281, n. 1, p. 147–155, 2011.

[172] SMOLUCHOWSKI, M VON. Drei vortrage uber diffusion, brownsche bewegung und koagulation von kolloidteilchen. **ZPhy**, v. 17, p. 557–585, 1916.

[173] SOARES, JASON W, STEEVES, DIANE M, SINGH, JAGDEEP, IM, JISUN, WHITTEN, JAMES E. Thiol adsorption on metal oxides: an approach for selective

deposition on zinc oxide nanoparticles. In: OXIDE-BASED MATERIALS AND DEVICES II, v. 7940. International Society for Optics and Photonics, p. 79400K, 2011.

[174] SOMORJAI, GA, MCCREA, KR, ZHU, J. Active sites in heterogeneous catalysis: development of molecular concepts and future challenges. **Topics in Catalysis**, v. 18, n. 3-4, p. 157–166, 2002.

[175] SOMORJAI, GABOR A. Modern concepts in surface science and heterogeneous catalysis. **Journal of physical chemistry**, v. 94, n. 3, p. 1013–1023, 1990.

[176] SOMORJAI, GABOR A, KLERER, JULIUS. Principles of surface chemistry. **Journal of The Electrochemical Society**, v. 119, n. 9, p. 279C, 1972.

[177] SOMORJAI, GABOR A, MCCREA, KEITH. Roadmap for catalysis science in the 21st century: a personal view of building the future on past and present accomplishments. **Applied Catalysis A: General**, v. 222, n. 1-2, p. 3–18, 2001.

[178] SONG, PENGXIANG, WEN, DONGSHENG. Molecular dynamics simulation of the sintering of metallic nanoparticles. **Journal of Nanoparticle Research**, v. 12, n. 3, p. 823–829, 2010.

[179] SONSTRÖM, P, BÄUMER, M. Supported colloidal nanoparticles in heterogeneous gas phase catalysis: on the way to tailored catalysts. **Physical Chemistry Chemical Physics**, v. 13, n. 43, p. 19270–19284, 2011.

[180] STERN, EA, SAYERS, DE, LYTLE, FW. Extended X-ray-absorption fine-structure technique. iii. determination of physical parameters. **Physical Review B**, v. 11, n. 12, p. 4836, 1975.

[181] STERN, EDWARD A. Theory of the extended X-ray-absorption fine structure. **Physical Review B**, v. 10, n. 8, p. 3027, 1974.

[182] SUN, CHANG Q, WANG, Y, TAY, BK, LI, S, HUANG, H, ZHANG, YB. Correlation between the melting point of a nanosolid and the cohesive energy of a surface atom. **The Journal of Physical Chemistry B**, v. 106, n. 41, p. 10701–10705, 2002.

[183] SURYANARAYANAN, V, NAIR, A SREEKUMARAN, TOM, RENJIS T, PRADEEP, T. Porosity of core–shell nanoparticles. **Journal of Materials Chemistry**, v. 14, n. 17, p. 2661–2666, 2004.

[184] TAIT, STEVEN L, NGO, LIEN T, YU, QIUMING, FAIN JR, SAMUEL C, CAMPBELL, CHARLES T. Growth and sintering of Pd clusters on α-al$_2$o$_3$ (0001). **The Journal of chemical physics**, v. 122, n. 6, p. 064712, 2005.

[185] TANG, ZHIYONG, KOTOV, NICHOLAS A, GIERSIG, MICHAEL. Spontaneous organization of single cdte nanoparticles into luminescent nanowires. **Science**, v. 297, n. 5579, p. 237–240, 2002.

[186] TAYLOR, H. S. **Proceedings of the Royal Society of London**, v. 108, 1925.

[187] TEIXEIRA, ANTONIO CARLOS SC, GIUDICI, REINALDO. Deactivation of steam reforming catalysts by sintering: experiments and simulation. **Chemical engineering science**, v. 54, n. 15-16, p. 3609–3618, 1999.

[188] TROVARELLI, ALESSANDRO. Catalytic properties of ceria and ceo2-containing materials. **Catalysis Reviews**, v. 38, n. 4, p. 439–520, 1996.

[189] TSONG, TIEN T. Experimental studies of the behaviour of single adsorbed atoms on solid surfaces. **Reports on Progress in Physics**, v. 51, n. 6, p. 759, 1988.

[190] HOEVEN, MVAN DER , KOBAYASHI, Y, DIERCKS, R. Technology roadmap: Energy and GHG reductions in the chemical industry via catalytic processes. **International Energy Agency: Paris**, v. 56, 2013.

[191] KLINK, JACQUES JOHANNESVAN DER , BROM, HANS BERNARD. NMR in metals, metal particles and metal cluster compounds. **Progress in Nuclear Magnetic Resonance Spectroscopy**, v. 36, n. 2, p. 89–201, 2000.

[192] VASEEM, M, UMAR, AHMAD, HAHN, YB, KIM, DH, LEE, KS, JANG, JS, LEE, JAE SUNG. Flower-shaped CuO nanostructures: structural, photocatalytic and XANES studies. **Catalysis Communications**, v. 10, n. 1, p. 11–16, 2008.

[193] VASQUEZ, RP. Cu_2O by XPS. **Surface Science Spectra**, v. 5, n. 4, p. 257–261, 1998a.

[194] VASQUEZ, RP. CuO by XPS. **Surface Science Spectra**, v. 5, n. 4, p. 262–266, 1998b.

[195] VASQUEZ, RP. $CuSO_4$ by XPS. **Surface Science Spectra**, v. 5, n. 4, p. 279–284, 1998c.

[196] VOGELAAR, BAS M, EIJSBOUTS, SONJA, BERGWERFF, JAAP A, HEISZWOLF, JOHAN J. Hydroprocessing catalyst deactivation in commercial practice. **Catalysis Today**, v. 154, n. 3-4, p. 256–263, 2010.

[197] VOLMER, M, STRATMANN, M, VIEFHAUS, H. Electrochemical and electron spectroscopic investigations of iron surfaces modified with thiols. **Surface and Interface Analysis**, v. 16, n. 1-12, p. 278–282, 1990.

[198] VOORHEES, PETER W. The theory of Ostwald ripening. **Journal of Statistical Physics**, v. 38, n. 1-2, p. 231–252, 1985.

[199] VOTER, ARTHUR F, MONTALENTI, FRANCESCO, GERMANN, TIMOTHY C. Extending the time scale in atomistic simulation of materials. **Annual review of materials research**, v. 32, n. 1, p. 321–346, 2002.

[200] VYSTAVEL, T, KOCH, SA, PALASANTZAS, G, DE HOSSON, J TH M. In situ transmission electron microscopy studies on structural dynamics of transition metal nanoclusters. **Journal of materials research**, v. 20, n. 7, p. 1785–1791, 2005.

[201] WAGNER, CARL. Theorie der alterung von niederschlägen durch umlösen (Ostwald-reifung). **Zeitschrift für Elektrochemie, Berichte der Bunsengesellschaft für physikalische Chemie**, v. 65, n. 7-8, p. 581–591, 1961.

[202] WALLACE, THOMAS J. Reactions of thiols with metals. i. low-temperature oxidation by metal oxides. **The Journal of Organic Chemistry**, v. 31, n. 4, p. 1217–1221, 1966.

[203] WANG, XIANQIN, HANSON, JONATHAN C, FRENKEL, ANATOLY I, KIM, JAW-YONG, RODRIGUEZ, JOSE A. Time-resolved studies for the mechanism of reduction of copper oxides with carbon monoxide: complex behavior of lattice oxygen and the formation of suboxides. **The Journal of Physical Chemistry B**, v. 108, n. 36, p. 13667–13673, 2004.

[204] WARREN, BERTRAM EUGENE. **X-ray Diffraction**: Reading, Addison-Wesley Publishing Company., 1990.

[205] WHITESIDES, GEORGE M. Nanoscience, nanotechnology, and chemistry. **Small**, v. 1, n. 2, p. 172–179, 2005.

[206] WHITTINGTON, BI, JIANG, CJ, TRIMM, DL. Vehicle exhaust catalysis: I. the relative importance of catalytic oxidation, steam reforming and water-gas shift reactions. **Catalysis Today**, v. 26, n. 1, p. 41–45, 1995.

[207] WILLERTZ, LE, SHEWMON, PG. Diffusion of helium gas bubbles in gold and copper foils. **Metallurgical Transactions**, v. 1, n. 8, p. 2217–2223, 1970.

[208] WYNBLATT, P, GJOSTEIN, NA. Supported metal crystallites. **Progress in solid state chemistry**, v. 9, p. 21–58, 1975.

[209] YANG, D-Q, SACHER, E. Coalescence kinetics of copper clusters on highly oriented pyrolytic graphite and Dow Cyclotene, as determined by X-ray photoelectron spectroscopy. **Journal of Applied Physics**, v. 90, n. 9, p. 4768–4771, 2001.

[210] YANG, GUANGPENG, DU, XUESEN, RAN, JINGYU, WANG, XIANGMIN, CHEN, YANRONG, ZHANG, LI. Understanding SO_2 poisoning over different copper species of Cu-SAPO-34 catalyst: a periodic DFT study. **The Journal of Physical Chemistry C**, v. 122, n. 37, p. 21468–21477, 2018.

[211] YANG, RUIQIN, ZHANG, YI, IWAMA, YUKI, TSUBAKI, NORITATSU. Mechanistic study of a new low-temperature methanol synthesis on Cu/MgO catalysts. **Applied Catalysis A: General**, v. 288, n. 1-2, p. 126–133, 2005.

[212] ZABINSKY, SI, REHR, JJ, ANKUDINOV, A, ALBERS, RC, ELLER, MJ. Multiple-scattering calculations of x-ray-absorption spectra. **Physical Review B**, v. 52, n. 4, p. 2995, 1995.

[213] ZHANG, JING, HUANG, FENG, LIN, ZHANG. Progress of nanocrystalline growth kinetics based on oriented attachment. **Nanoscale**, v. 2, n. 1, p. 18–34, 2010.

[214] ZHU, HUILONG. Sintering processes of two nanoparticles: a study by molecular dynamics simulations. **Philosophical Magazine Letters**, v. 73, n. 1, p. 27–33, 1996.

[215] ZHUANG, ZANYONG, ZHANG, JING, HUANG, FENG, WANG, YONGHAO, LIN, ZHANG. Pure multistep oriented attachment growth kinetics of surfactant-free SnO_2 nanocrystals. **Physical Chemistry Chemical Physics**, v. 11, n. 38, p. 8516–8521, 2009.